INFORMATION TO USERS

This manuscript has been reproduced from the microfilm master. UMI films the text directly from the original or copy submitted. Thus, some thesis and dissertation copies are in typewriter face, while others may be from any type of computer printer.

The quality of this reproduction is dependent upon the quality of the copy submitted. Broken or indistinct print, colored or poor quality illustrations and photographs, print bleedthrough, substandard margins, and improper alignment can adversely affect reproduction.

In the unlikely event that the author did not send UMI a complete manuscript and there are missing pages, these will be noted. Also, if unauthorized copyright material had to be removed, a note will indicate the deletion.

Oversize materials (e.g., maps, drawings, charts) are reproduced by sectioning the original, beginning at the upper left-hand corner and continuing from left to right in equal sections with small overlaps.

Photographs included in the original manuscript have been reproduced xerographically in this copy. Higher quality 6" x 9" black and white photographic prints are available for any photographs or illustrations appearing in this copy for an additional charge. Contact UMI directly to order.

Bell & Howell Information and Learning
300 North Zeeb Road, Ann Arbor, MI 48106-1346 USA
800-521-0600

UMI®

A TWO-DIMENSIONAL AMPLITUDE-STEERED ARRAY FOR REAL-TIME VOLUMETRIC ACOUSTIC IMAGING

BY

CATHERINE ANN HILLSLEY FRAZIER

B.S.E.E., University of Maryland at College Park, 1994
M.S., University of Illinois at Urbana-Champaign, 1996

THESIS

Submitted in partial fulfillment of the requirements
for the degree of Doctor of Philosophy in Electrical Engineering
in the Graduate College of the
University of Illinois at Urbana-Champaign, 2000

Urbana, Illinois

UNIVERSITY OF ILLINOIS AT URBANA-CHAMPAIGN

THE GRADUATE COLLEGE

APRIL 2000
(date)

WE HEREBY RECOMMEND THAT THE THESIS BY

CATHERINE ANN HILLSLEY FRAZIER

ENTITLED A TWO-DIMENSIONAL AMPLITUDE-STEERED ARRAY FOR REAL-TIME VOLUMETRIC ACOUSTIC IMAGING

BE ACCEPTED IN PARTIAL FULFILLMENT OF THE REQUIREMENTS FOR THE DEGREE OF DOCTOR OF PHILOSOPHY

W D Brien
Director of Thesis Research

William R. Perkins Joy S.M. Kang
Head of Department

Committee on Final Examination†

W D Brien
Chairperson

David C. Munson, Jr.

George W. Swenson, Jr.

Robert Hamilton

J C Gaboriaud

† Required for doctor's degree but not for master's.

O-517

ABSTRACT

Real-time volumetric ultrasound imaging is difficult due to problems with array construction and due to the slow speed of data collection. In 1976, a linear amplitude-steered array was introduced that uses reduced electronics to steer a monofrequency beam. The current study examines how the linear amplitude-steered array can be extended to a two-dimensional array operating over a broad range of frequencies to be used for a real-time volumetric imaging system. First, the properties of the linear amplitude-steered array are studied, showing that there is a tradeoff between axial and lateral resolution, unique to this array, that depends on the length of the array. Second, various time-frequency distributions are surveyed for use in creating an image from a single received signal. Next, the concepts of imaging with a linear array are extended to imaging a volume with a two-dimensional amplitude-steered array. The array design is presented, and it is shown that targets can be localized by using the frequency separation of the amplitude-steered array in the vertical direction and conventional phased array beamsteering in the horizontal direction. Several methods for displaying the data are presented, with projection images offering computational savings. Nonlinear propagation is also discussed, demonstrating that although frequency of the received signal is equated with position, nonlinear generation of harmonics does not cause the appearance of false targets in the images. Experimental data are compared with simulations to validate the simulations of the array operation.

ACKNOWLEDGMENTS

There are many people whose support I would like to acknowledge. First, I would like to thank my research advisor, Professor William D. O'Brien, Jr., for his guidance, for the many opportunities he has given me, and for providing steady support. I would also like to thank my committee members, Professor David C. Munson, Jr., Professor Robert Darmody, Professor John G. Harris, and Professor George Swenson for their insightful questions and comments, which have greatly enhanced this work. I am grateful to Dr. Jack Hughes for introducing me to the amplitude-steered array.

I would like to thank the team of the people at the Applied Research Laboratory at the Pennsylvania State University for sharing results and ideas, in particular, Mark Geleskie, Scott Brown, and Dave van Tol. The experimental data for this thesis were collected at ARL. I very much appreciate the help of Mark Geleskie, Pete Tussey, and Greg Granville for their help on that trip, making sure the array was operational and positioning targets during the experiments. I am also grateful to Ken and Mechteld Hillsley and to Jean and Cale Brownstead for letting me stay with them during my trips to State College.

The people of the Bioacoustics Research Laboratory have supported me throughout my years here. They are my mentors, teachers, and friends. It has been a pleasure to work with them. In particular, I would like to thank Wanda Elliot and Sue Clay for all of their administrative assistance, which greatly reduced the number of things I had to worry about.

To my friends, informally known as the Maryland mafia, many thanks for insights, which they may not know they provided, for being there to share holidays and special

occasions, and not least of all for babysitting. In many ways, they have made this thesis possible.

Finally, I am grateful to my family for their encouragement. My parents, Richard and Audrey Hillsley, and my brothers and sisters have always believed in me. My son, Philip, always gave me an excuse to play outside on a nice day. My husband, Victor, is my partner and my friend; we are a great team. At various times, they have each given me the support I needed to complete this work.

This research has been funded by DARPA under BAA 97-33. This work was also supported by the American Association of University Women through a Selected Professions Fellowship from July 1999 to June 2000. This thesis is based upon work sponsored by the Department of the Navy, Indian Head Division, Naval Surface Warfare Center under Grant N00174-98-1-0032. Any opinions, findings, and conclusions or recommendations expressed herin are those of the author and do not necessarily reflect the views of the Department of the Navy.

TABLE OF CONTENTS

LIST OF TABLES

LIST OF FIGURES

CHAPTER 1

INTRODUCTION

Acoustic arrays are used for many imaging applications, including medical imaging, sonar, atmospheric imaging, seismic imaging, and nondestructive evaluation. Typically, one-dimensional arrays are used to collect data and two-dimensional images are formed, where the first dimension is azimuth and the second dimension is range. For medical imaging, extensions have been made to 1.5-dimensional arrays, which have many elements in the azimuthal direction and few elements in the elevation direction so that some focusing in elevation can be included. These 1.5-dimensional arrays are also used to form two-dimensional images.

Two-dimensional arrays, which allow focusing and beamsteering in both azimuth and elevation, are desirable in imaging applications because they offer the possibility of improved image quality for two-dimensional images or they can be used for three-dimensional imaging. Three-dimensional imaging allows better visualization of anatomy or structures. In medical imaging, three-dimensional images can provide information on the shape of a solid mass, one of the parameters used to distinguish benign and malignant tumors. Real-time three-dimensional imaging would allow a physician to view the structures of the heart throughout the cardiac cycle. In sonar, volumetric imaging is most often considered for short range applications (less than 10 m) such as fish counting, assisting divers, monitoring remotely operated vehicles, or mine hunting. Real-time three-dimensional imaging could provide the visibility required to locate objects such as damaged pipes in turbid water.

In seismic imaging or nondestructive evaluation, real-time implementation of three-dimensional imaging is not critical because the targets are stationary. However, for medical imaging, sonar, and atmospheric imaging, real-time data collection is important. Transient events might be missed if the time to scan the volume is long. Also,

images created off-line would be distorted by motion of objects in the scene during data collection. The remainder of this thesis will focus on sonar and medical imaging.

1.1 Real-Time Three-Dimensional Ultrasound

Three-dimensional medical ultrasound exists; however, it is not real-time. Current systems typically scan two-dimensional planes using linear arrays and then translate or rotate the array to scan the next plane. Three-dimensional images are then formed off-line [1]. Often for cardiac imaging, where real-time data collection is most critical, data are collected over several heart beats, and then the data from differenct cycles are combined so that a single cycle of the heart can be recreated as a cineloop. Successive heart beats must be similar enough for the reconstruction. In many cases, irregular heart beats are thrown out [2], [3], making it impossible to use these systems to diagnose a heart abnormality.

Real-time three-dimensional imaging, meaning updating the volume of data at a rate of 30 Hz, is difficult due to two problems. The first is a problem only because of the current state of array fabrication technology. The second is a more fundamental constraint, dependent on the properties of the medium. Our study addresses the latter; however, it is worth mentioning the issues of array construction. Three-dimensional imaging requires a two-dimensional array. The difficulty in fabricating two-dimensional arrays arises from the large number of very small, very closely packed elements. A large number of elements is required to achieve a reasonable aperture size for resolution. Elements must be small and closely packed because a fully sampled array must have an interelement spacing of $\frac{\lambda}{2}$ or less in order to avoid grating lobes, where λ is the wavelength in the medium. For a system operating in water at 3 MHz, the wavelength is 500 μm. As frequency increases, the wavelength decreases, making the problem worse. Small elements can have poor sensitivity due to their high electrical impedance, and small elements make electrical connections difficult. Close spacing increases the potential for electrical or acoustic cross-talk. A large number of elements implies a high channel count, which is difficult to implement due to space limitations. The number of elements can be reduced and the interelement

spacing increased by using sparse array layouts [4], although reducing the number of elements will increase the average sidelobe level of the beam pattern. The sensitivity, cross-talk, and connection problems can be addressed using new technology such as thick films, although much improvement is still needed [5], [6], [7].

The second challenge in implementing real-time volumetric imaging systems is the slow speed of data collection. Data collection for a three-dimensional image using techniques of two-dimensional imaging requires too much time for volumes to be scanned in real-time. The physical limit is the speed of sound in the medium. For example, collecting data for a medical image up to 15 cm deep in the body requires 25 ms, where the speed of sound is assumed to be 1540 m/s and where 128 pulses are used to create 128 lines in the image. A three-dimensional image formed with 128^2 pulses under the same conditions requires 3.19 s. Real-time three-dimensional imaging using conventional data collection techniques would be impossible. The solution to this problem is to form several beams from one transmitted pulse and to separate reflections from different directions through processing.

1.1.1 Medical imaging

Several groups have developed methods for real-time three-dimensional medical imaging. Using a sparse synthetic aperture beamformer, Lockwood, Talman, and Brunke [8] have developed a linear array that is mechanically rocked to collect data for three-dimensional images. The system is a modification of currently available systems that rock the transducer to collect a volume of data in that the rocking is accomplished at a high enough rate for the data collection to be real-time. Few transmit pulses, each using a small number of elements, are used to reduce the data acquisition time for a single transducer position. With synthetic aperture beamforming, all the receive beams corresponding to one transmit pulse can be formed simultaneously. Using a linear array reduces the required channel count. This technique has been demonstrated for medical imaging only in simulation.

Shen and Ebbini [9] have worked on coded-excitation in combination with a pseudo-inverse operator so that multiple beams can be received at one time. This

system has been tested for two-dimensional image creation using a one-dimensional array. Independent codes are transmitted on each element, resulting in different impulse responses in each steering direction. Returns from different directions are then separated using filters. Their proposed method does not require a Nyquist sampled array, so that fewer elements of the two-dimensional array may be used without degrading the image quality. Images formed using previous coded-excitation methods with matched filter operators have suffered because correlations between beams in different directions produce artifacts in the images. Shen and Ebbini's technique is reported not to have this drawback; however, the pseudo-inverse operator suffers from consequences of the assumption that targets occur on a grid pattern. If target positions differ from the grid pattern, the image quality is degraded.

Lu [10] has proposed a technique for three-dimensional imaging using limited diffraction beams. In this case, a plane wave pulse is transmitted from the two-dimensional array to illuminate the scene. Then in reception the same transducer array is used to form an array of diffraction limited beams by varying the weighting on the elements. Using a three-dimensional inverse Fourier transform, a three-dimensional image is created. This technique requires a fairly large, broadband array, and it is limited to imaging the region directly in front of the array. The largest cross-sectional area that can be imaged is equal to the area of the array. The imaged area can be increased only by using a large number of transmit pulses. The method has been tested using a phantom with embedded point scatterers [11]. The results look promising, although the images reveal the dependence of the technique on the broad bandwidth of the transducer.

Finally, researchers from Duke University have a real-time volumetric imaging system, which is in operation [12]. Their system uses a sparse, two-dimensional array. As reported in 1991, the volume is scanned in a pyramidal scheme, with 12 transmit pulses in the elevation direction and 52 transmit pulses in the azimuthal direction, for a total of 624 transmit pulses per volume. Parallel beamforming is used in the elevation direction so that eight receive beams are formed for each transmit pulse. The volume can be scanned eight times per second. Initial image quality was

poor. To improve the image quality, they have been working on improving the two-dimensional array, increasing channel count and frequency. They would also like to implement parallel beamforming in the azimuthal direction as well as in elevation.

Although many groups have been working on the problem in medical imaging, the ideal solution has not yet been found. Shen and Ebbini's technique has not yet been extended to volumetric imaging. Lu's technique is promising; however, to achieve the high frame rate, it requires that signals received by every element be stored, which means having a large number of channels. As explained earlier, having a large number of channels is difficult due to space considerations. The synthetic aperture methods of Lockwood and Smith are fairly brute force methods to reduce the number of transmit pulses used. The frame rate on the Duke system was 8 frames/s. In order to increase the frame rate, the number of transmits will have to be reduced even further.

1.1.2 Sonar imaging

Three-dimensional sonar imaging has been developed for applications such as fish counting, mine hunting, and inspecting structures. In general, systems are designed to complement or replace optical systems, which are ineffective in turbid water. Sonar imaging differs from medical imaging in the ranges of interest. Maximum ranges of interest range from 170 m to 2.4 m, and operating frequencies range from 200 kHz to 3.5 MHz. In order to accomplish real-time sonar imaging, even fewer transmit pulses are available than for medical imaging. Several of the systems discussed in the literature are based on transmitting a single pulse with a broad region of coverage and then focusing or processing the received signals to produce an image. Jones [13] uses the simplest system, transmitting a chirp over a broad region and then using a sparse two-dimensional array to steer and focus the receive beam. Such a system will suffer from poor signal-to-noise ratio due to the broad spread of energy in the transmit and the high average sidelobe level of the receive beam pattern. Also, the broad transmit beam will lower the achievable resolution.

In [14], a single transmit is used to insonify a region and a two-dimensional transducer array is used to receive reflected signals; however, the processing is not the

same as conventional beamforming of the received signals. Instead, the processing uses a noncoherent correlation of the received signals, or correlation of the envelopes of the received signals. First, the magnitude-squared of the received signal from each element is calculated. Each of these detected signals is multiplied by the envelope of the transmitted signal appropriately delayed to correspond to the location of a reflector at the assumed angle and range. The multiplied signal is then integrated, and the sum over all the array elements is taken. A large sum indicates a target at the assumed direction and range. The proposed method is reported to have the advantages of no grating lobes regardless of interelement spacing and reduction in speckle. However, it is acknowledged that the method will have poor angular resolution. In fact, both angular resolution and depth of field depend directly on ct_e/f_0, where c is the speed of sound, t_e is the time duration of the transmitted signal envelope, and f_0 is the carrier frequency. Angular resolution is also inversely proportional to the size of the array. Since small angular resolution and large depth of field are desirable, the best way to improve angular resolution is by increasing the size of the array; however, total array sizes are generally limited. For example, in a diver held sonar, the array must fit into a system that a diver can hold. In addition, although -3 dB beamwidth of the correlation system can be made comparable to that of a focused beamforming system, the -10 dB and -20 dB beamwidths of the correlation system are much larger than those of the focused beamforming system, meaning poor image contrast. This system has been demonstrated in simulation for three-dimensional imaging of few point targets.

Ishihara et al. have developed a system that uses a coded wavefront [15]. As discussed earlier, coded wavefront systems suffer from image artifacts due to the non-orthogonality of beams in different directions. Here, multiple transmits and receptions are used to compensate for this problem. As presented, the maximum range tested is 170 m. Collecting data for and reconstructing one image requires approximately one second. For much shorter ranges, reconstructing an image would require less time; however, the requirement for multiple transmit pulses limits the maximum achievable frame rate.

Other researchers are developing lens-based systems. Belcher et al. [16] and Kamgar-Parsi et al. [17] have developed three small, high-frequency sonars that use lenses. In both cases, the transmitter is a single element or row of the two-dimensional array. The receiver is the two-dimensional array located in the focal plane of the lens. An acoustic camera is being developed by Erikson at Lockheed Martin. It is also a lens-based system using a transducer hybrid array (THA) and a C-scan format for data collection [18]. A separate transmitter, with a wide beam, is used to insonify the region of interest. Then, an acoustic lens is used to image multiple planes onto the acoustic array. In all of these systems, the lens accomplishes the focusing, so that the electronics requirement is reduced. A small number of range planes can be collected with a single transmit pulse; more range planes are collected with successive pulses. The total range depth that can be imaged is determined by the depth of focus of the acoustic lens, which is limited. The design range for Erikson's system is approximately 120 mm, much shorter than our intended range. The maximum range is limited by the fact that multiple transmit pulses are required to collect the entire volume of data.

The systems mentioned in this section all use a transmit pulse with broad coverage. Resolution would be improved if the transmitted beam could be focused or made narrow in multiple directions.

1.2 Spatial Frequency Separation

Another approach to achieving multiple beams with one transmit pulse is to steer the beam by changing the frequency. F. L. Lizzi and K. W. Weil hold a patent on a transducer device which uses change in frequency to steer a beam [19]. Using a curved transducer with tapered thickness and then exciting the transducer with different frequencies, beams with different origins and steering directions can be radiated. By changing the frequency continuously, the beam is scanned through a sector. The system is limited by the fact that the ratio of highest to lowest excitation frequency cannot be more than three. Otherwise, at the highest frequencies, multiple beams will be radiated with different orientations and steering directions, as the transducer

will radiate from all places where the excitation frequency is an odd multiple of a half wavelength of thickness.

This thesis presents the use of spatial frequency separation achieved using amplitude-weighting to solve the problem of slow data collection. The concept of steering the maximum response of an array using amplitude weighting was introduced by Hughes and Thompson in 1976 [20]. At that time, the intent of amplitude steering was to tilt the maximum response of the beam pattern without using multiple delay lines or phase-shift networks, which are bulky. In their formulation, the beam was steered to a particular direction at a single frequency, and the fact that the steering direction changed with frequency was considered a drawback of the design.

By operating a linear amplitude-steered array in broadband mode, with an impulsive or chirp excitation, the maximum array response is swept over a range of angles. A sector can be scanned using a single transmit pulse, leading to fast two-dimensional imaging of the sector, compared to conventional imaging which uses one transmit pulse for each steering direction. The two-dimensional amplitude-steered array (patent pending), which can be used for volumetric imaging, uses frequency separation to determine vertical position and conventional beamforming to determine horizontal location. Although the array may be a fully sampled two-dimensional array, a separate channel is not required for each element. Only four channels are required per column of elements. Potential advantages of using this array for volumetric imaging are fewer electronics than required for proposed medical systems that must address each element individually and better resolution than current sonar systems that use a broad transmit beam.

1.3 Organization of This Thesis

This research was undertaken as part of a larger project developed by the Applied Research Laboratory (ARL) at the Pennsylvania State University. The team at ARL was led by W. Jack Hughes and Charles Allen. Other subcontractors include Northrup Grumman, Blatek, Inc., and TRS Ceramics, Inc., whose responsibilities were issues of array construction. This thesis is a study of the operation of the amplitude-steered

array for imaging. Although we focus on an underwater imaging application, the array may be modified for use in other systems, such as medical imaging systems.

Chapter 2 introduces the amplitude-steered array by examining fundamental issues of how the linear amplitude-steered array would be used to form two-dimensional images. In particular, we study the tradeoff between axial and lateral resolution, and we survey various forms of time-frequency processing to form images. Chapter 3 discusses the extension of the linear array to a two-dimensional array for volumetric imaging. As presented, the array is a linear amplitude-steered array in one direction, and a conventional phased array in the perpendicular direction. A specific application is chosen around which a specific array is designed. The array layout is discussed along with the achievable resolution. Finally, strategies for presenting images from the data are given, including surface rendering, slice images, and projection images. The analyses in Chapters 2 and 3 are performed with simulated data. In Chapter 4, we compare simulated results to experimental data collected with a low frequency version of the linear amplitude-steered array. Having validated the simulations with experimental data, we show the effect of nonlinear propagation on the operation of the array in Chapter 5. Nonlinear propagation results in the generation of higher harmonics, and our processing equates frequency with position. Therefore, we must consider the possibility that false targets will appear in the images. Finally, Chapter 6 gives a summary of research results and suggestions for future work.

CHAPTER 2

ONE-DIMENSIONAL AMPLITUDE-STEERED ARRAY

The amplitude-steered array, introduced by Hughes and Thompson in 1976 [20], was originally designed to steer a monochromatic signal to a particular direction. Using the array for an imaging application requires an evaluation of the field pattern, the achievable resolution, and the derivation of signal processing methods to form an image. This chapter is concerned with issues of using the linear amplitude-steered array for two-dimensional imaging. The basic operation of the array, an analysis of axial and lateral resolution, and the development of time-frequency processing for forming images are discussed in this chapter. The results presented in this chapter provide the basis for the extension to three-dimensional imaging with the two-dimensional array presented in the next chapter.

2.1 Array Field Pattern

In this discussion, we first consider the one-way far-field pressure of a linear array of equally spaced, equiamplitude point sources. Figure 2.1 gives a diagram defining variables. (All figures and tables appear at the end of the chapter.) To steer the main lobe to θ_0, the signal from each element can be phase-shifted by multiplying by the factor $e^{-j(nk_0d\sin\theta_0)}$, where n is an index used to enumerate the elements, k_0 is the wavenumber at a particular frequency, and d is the distance between the elements. This phase shift will only steer the main lobe to θ_0 at the frequency used to calculate k_0; therefore, a fixed phase shift is generally used for narrowband operation. The

pressure field can be expressed as

$$P(r,\theta) = \frac{e^{-jkr}}{r}\sum_{n} e^{jnd(k\sin\theta - k_0\sin\theta_0)} = \frac{Ne^{-jkr}}{r}H(\theta). \tag{2.1}$$

Now, we consider only the array pattern, $H(\theta)$. We assume that we have an array with an even number of elements N, and we measure the phase for each element relative to the center of the array. To simplify the expression, we replace $\frac{kd}{2}\sin\theta$ with u and $\frac{k_0 d}{2}\sin\theta_0$ with ϕ.

$$H(\theta) = \frac{1}{N}\sum_{n=-\frac{N}{2}+1}^{\frac{N}{2}} e^{j(2n-1)(u-\phi)} \tag{2.2}$$

Combining terms of the sum in pairs, we have

$$H(\theta) = \frac{2}{N}[\cos(u-\phi) + \cos(3(u-\phi)) + \cdots + \cos((N-1)(u-\phi))] \tag{2.3}$$

Using the trigonometric identity for the cosine of a sum, Equation (2.3) can be rewritten as

$$\begin{aligned} H(\theta) = \tfrac{2}{N}[&\cos\phi\cos u + \cos 3\phi\cos 3u + \cdots + \cos((N-1)\phi)\cos((N-1)u) \\ &+ \sin\phi\sin u + \sin 3\phi\sin 3u + \cdots + \sin((N-1)\phi)\sin((N-1)u)] \end{aligned} \tag{2.4}$$

A corresponding equation for an array with an odd number of elements N_{odd} is

$$\begin{aligned} H(\theta) = \tfrac{2}{N_{odd}}\ [&0.5 + \cos 2\phi\cos 2u + \cos 4\phi\cos 4u \\ &+ \cdots + \cos((N_{odd}-1)\phi)\cos((N_{odd}-1)u) \\ &+ \sin 2\phi\sin 2u + \sin 4\phi\sin 4u \\ &+ \cdots + \sin((N_{odd}-1)\phi)\sin((N_{odd}-1)u)] \end{aligned} \tag{2.5}$$

Using Equation (2.4), we shift our interpretation of how the beamsteering is achieved. At the beginning of this discussion, we steered the beam by phase-shifting a linear array of equiamplitude elements. Now we steer the beam by weighting the elements. In Equation (2.4), $\cos((2n-1)\phi)$ and $\sin((2n-1)\phi)$ terms are constants which we interpret as amplitude weights on the elements. The $\cos((2n-1)u)$ and $\sin((2n-1)u)$ terms represent combinations of pairs of elements on opposite sides of the center of the array in phase or 180° out of phase, respectively. Therefore, Equation (2.4) can be interpreted as the sum of the outputs of two arrays. The first array

(sum of $\cos(2n-1)u$ terms) combines elements on opposite sides of the center with equal amplitudes and in phase. We call this the phase-symmetric array. The second array (sum of $\sin(2n-1)u$ terms) combines elements on opposite sides of the array with equal amplitudes and 180° out of phase. We call this the phase-antisymmetric array. According to Equation (2.4), the outputs of the two arrays should be added in phase; however, the output of a phase-antisymmetric array is inherently 90° out of phase with the output of a phase-symmetric array. The outputs of the two arrays, therefore, must be added with an additional ±90° shift [21]. The sign of the shift determines whether the beam is tilted towards positive θ_0 or towards negative θ_0. We note that if we used only one set of weights, cosine or sine, the beam pattern would have main lobes at both positive θ_0 and negative θ_0.

Conceptually, we have used one array with two sets of weights, or two arrays, to achieve beamsteering. In practice, the array layout is designed such that the phase-symmetric and phase-antisymmetric arrays share the same space. The $\cos(2n-1)\phi$ and $\sin(2n-1)\phi$ factors in Equation (2.4) are the amplitude weights which determine the steering direction of the main beam, but they do not have any effect on sidelobe levels. Further apodization can be applied to achieve reduced sidelobe levels, as demonstrated in Appendix A.

If the array described above is excited by a frequency different from the design frequency used to calculate ϕ, the maximum response will occur at an angle different from the designed steering direction θ_0.

$$\phi = \frac{k_0 d}{2}\sin\theta_0 = \frac{k_f d}{2}\sin\theta_f \tag{2.6}$$

The subscript f was added to k and θ to emphasize that the new steering direction is calculated for a specific frequency f. Rearranging to solve for the new steering direction θ_f gives

$$\theta_f = \sin^{-1}\left(\frac{k_0}{k_f}\sin\theta_0\right) \tag{2.7}$$

which can be restated as

$$\theta_f = \sin^{-1}\left(\frac{f_0}{f}\sin\theta_0\right) \tag{2.8}$$

As the frequency increases, the angle that the beam is steered away from broadside decreases. Table 2.1 lists the steering direction for several frequencies for a 9.76-cm-length array, which is designed to steer to 5° at 5.6 MHz. An example of several beams from the array is shown in Figure 2.2. Beams are shown for 5.6 MHz (5°), 4.5 MHz (6.23°), 3.4 MHz (8.25°), 2.3 MHz (12.25°), and 1.2 MHz (24°). From the table and the figure, we see that as the frequency decreases, the beamwidths increase and the spacing between the beams also increases.

2.2 Resolution Tradeoff for Imaging

We take advantage of the separation of frequencies caused by the amplitude weighting to collect data for a two-dimensional image using a single transmit pulse. A linear-FM chirp is transmitted from the array. As the frequency changes, the main beam is swept over a sector. The reflected wave is received by the array and filtered using a matched-filter to accomplish pulse-compression. Then the short time Fourier transform (STFT) is calculated to determine the range and lateral position of the targets. The one-dimensional amplitude steered array localizes targets using time-of-flight and frequency information. The temporal position of the FFT window gives the range of the target, and the frequencies contained within the window give the lateral position of the target. In this section, we derive the achievable resolution using this scheme.

2.2.1 Definition of resolution

In traditional imaging, where the transducer is shock-excited, axial resolution is determined by the spatial length of the transmitted pulse, which can be related to the relative bandwidth of the transducer and the wavelength at the center frequency and which is independent of the size of the transducer [22].

In analyzing the resolution achieved by the amplitude-steered array, we will use one-point definitions for lateral and axial resolution, which correspond to measuring the axial and lateral extent of the point spread function. This definition is used in contrast to a two-point definition, which would specify the minimum separation

between two points that allows the points to be distinguished. For the amplitude-steered array of point elements operated at a particular frequency f, the array pattern can be written as

$$H(\theta) = \frac{1}{N} \frac{\sin(\frac{N}{2} kd(\sin\theta - \sin\theta_f))}{\sin(\frac{1}{2} kd(\sin\theta - \sin\theta_f))} \tag{2.9}$$

where $k \sin\theta_f = k_0 \sin\theta_0$. We define lateral resolution as the -3-dB width of the one-way array pattern. The -3-dB points on either side of the maximum are the points where the argument of the periodic sinc is ± 1.3894. We use the expression

$$\frac{N}{2} kd(\sin\theta_{-3dB} - \sin\theta_f) = \pm 1.3894 \tag{2.10}$$

Solving for θ_{-3dB} on each side of the maximum array response,

$$\begin{aligned} \theta^{+}_{-3dB} &= \sin^{-1}(\sin\theta_f + \frac{0.4423\lambda}{Nd}) \\ \theta^{-}_{-3dB} &= \sin^{-1}(\sin\theta_f - \frac{0.4423\lambda}{Nd}) \\ \alpha &= \theta^{+}_{-3dB} - \theta^{-}_{-3dB} \end{aligned} \tag{2.11}$$

where α is the lateral resolution in degrees.

Axial resolution is defined as the spatial length of the pulse:

$$AR = \frac{ct}{2} \tag{2.12}$$

where c is the speed of sound in the medium and t is the temporal length of the pulse. For conventional imaging, where the transducer is shock-excited, this description of axial resolution can be related to an expression for axial resolution which depends on the wavelength at the resonance frequency and on the Q of the transducer, where Q is defined as 2π times the energy stored at resonance divided by the energy lost per cycle [22]. That expression is given by

$$AR = \frac{Q\lambda}{4} \tag{2.13}$$

An alternate definition of Q, $Q = \frac{f_r}{\Delta f}$, where f_r is the resonance frequency and Δf is measured at half power points, is consistent with the previous definition of Q [23]. Therefore, Equation (2.13) is a definition of axial resolution in terms of the inverse of the relative bandwidth of the transducer.

We seek a definition of axial resolution that is similar in form to Equation (2.13). However, our definition of resolution will not depend on the Q of the transducer, but rather on the inverse of the relative bandwidth of the received signal $\frac{f}{\Delta f}$, which we call Q_{sig}. We transmit a chirp and then apply matched filtering for pulse compression. The output of the pulse compression operation is approximately a sinc if the time-bandwidth product of the received signal is large enough [24]

$$\rho = \frac{\sin(\frac{2\pi\Delta f x}{c})}{\frac{2\pi\Delta f x}{c}}, \tag{2.14}$$

where ρ is the correlation between the received signal and the impulse response of the filter, Δf is the bandwidth of the received chirp, c is the speed of sound, and x is the range which is calculated as $\frac{ct}{2}$ when the array is operated in pulse-echo mode. Pulse compression of a linear FM chirp compensates for the quadratic phase and therefore gives an approximately rectangular band of frequencies with linear phase. In the time domain, this description corresponds to a sinc function. The discussion of whether or not the criterion on the time-bandwidth product has been met is reserved until Section 2.2.2. We use the -3-dB points of ρ to find the axial resolution. The function falls to -3 dB, relative to the maximum, when the argument of the sinc function is equal to ± 1.3894:

$$\frac{2\pi\Delta f x_{-3dB}}{c} = 1.3894 \tag{2.15}$$

We write

$$\frac{2\pi f}{c}\frac{\Delta f}{f} x_{-3dB} = 1.3894 \tag{2.16}$$

and solve for $2x_{-3dB}$, where the factor of 2 accounts for the -3-dB points on each side of the maximum. The expression for axial resolution is

$$AR = 2x_{-3dB} = 0.4423\, Q_{sig}\lambda \tag{2.17}$$

where Q_{sig} is the inverse of the relative bandwidth of the received signal, and λ is the wavelength at the center frequency of the received signal f. Although this expression does not explicitly depend on the length of the array, we will see in the next section, where we discuss the tradeoff between axial and lateral resolution, that Q_{sig} depends on the length through the beamwidth. We could have reduced Equation (2.16) to an

expression for x_{-3dB} that was a function of Δf, rather than a function of both Q_{sig} and λ; however, we prefer to have an expression in terms of the wavelength so we can see how resolution will change with center frequency, rather than with bandwidth.

Note that for good resolution, we would like both θ_{-3dB} and x_{-3dB} to be small. Also, note that while absolute range position of the target is given by the time-of-flight (temporal position of the FFT window), the range resolution depends only on frequency bandwidth. Similarly, lateral position may be given by the center frequency of the returned signal, but lateral resolution is determined by the length of the array in terms of number of wavelengths.

2.2.2 Axial and lateral resolution tradeoff

The amplitude-steered array spatially separates frequencies by virtue of the fixed phase shift used to calculate amplitude weights. If the frequencies could be completely separated, i.e., if the beams were infinitely narrow, a point target within the insonified region would produce a single frequency return, implying that two point targets separated only in range could not be distinguished. In reality, it is possible to distinguish multiple targets in the same direction at different ranges because beams are not infinitely thin, but overlap due to the finite length of the array.

Figure 2.3 conceptually shows the tradeoff between axial and lateral resolution. In parts (a) and (b), the curves plotted show the steering direction versus frequency. The curves are the same for both plots. The error bars indicate the -3-dB beamwidth at each frequency. We can see from the error bars that lateral resolution improves with increasing frequency, as expected. Axial resolution can also be determined from each plot. At a particular steering direction, by observing the range of frequencies that overlap, we can determine the bandwidth at that particular direction. In both parts (a) and (b) of Figure 2.3, the frequencies that overlap at a steering direction of 15° are located between the dashed lines. The extent of the dashed lines along the frequency axis tells us Δf. We know the "resonance frequency," the frequency with the greatest amplitude at 15°, from the curve. Therefore, we can determine the wavelength and Q_{sig}. Axial resolution can be calculated using Equation (2.17).

Figure 2.3(a) shows field characteristics for a 1-cm-length array. If the length of the aperture is increased from 1 cm to 4 cm, the lateral resolution improves, illustrated by the decrease in size of the error bars between Figure 2.3(a) and 2.3(b). However, that decrease in beamwidth implies a decrease in the range of frequencies that overlap in a particular direction, illustrated by the more narrow range between the dashed lines in Figures 2.3(a) than in 2.3(b). Therefore, Q_{sig} increases with increased array length, and the axial resolution is worsened. Therefore, there is a tradeoff between axial and lateral resolution that depends on the length of the array, or equivalently, on the width of the beam at each frequency.

Finite element size may change the beamwidth, which affects Q_{sig} and therefore axial resolution. With finite elements, the overall array pattern of Equation (2.9) is multiplied by the beam pattern of the individual element, which can narrow the main beam, thus improving the lateral resolution and degrading the axial resolution. For an array of rectangular elements, the unsteered beam pattern is given by

$$H(\theta) = \frac{1}{N} \frac{\sin(\frac{Nkd}{2} \sin\theta)}{\sin(\frac{kd}{2} \sin\theta)} \frac{\sin(\frac{ka}{2} \sin\theta)}{\frac{ka}{2} \sin\theta} \tag{2.18}$$

where a is the width of the element. The largest possible width of the element is the center-to-center spacing of the elements ($a = d$), which would give a continuous aperture. If N is large, the expression for the width of the main beam will be dominated by the periodic sinc term, the array pattern. Likewise, if $a \ll d$, the expression for the width of the main beam will be dominated by the array pattern. In the other extreme, if $a = d$ and $N = 2$, the effect of the element size is to double the length of the array compared to the array of two point elements. In that case and in similar cases where N is small and $a \approx d$, the finite element size will have a larger effect improving lateral resolution and degrading axial resolution. In general, the effect will be small for practical imaging arrays.

Finally, when deriving the expression for axial resolution, we made use of an approximation that the output of the pulse-compression operation is a sinc function if the time-bandwidth product is large enough. One numerical value for "large enough" is 100. Whether or not this condition is met depends on the received signal, which

means that it depends on the length of the array and the chirp rate. The bandwidth of the received signal will depend on the range of frequencies that overlap, which has been shown to depend on the length of the array. The chirp rate can be set independently so that the criterion is met. One limit to how slow the chirp rate can be is the most shallow range of interest. The entire transmit pulse must be emitted before any signal is to be received.

2.2.3 Simulation and results

We analyze the tradeoff between axial and lateral resolution for a linear array by simulating the received signal from point targets when the array is used in pulse-echo mode. Three arrays with different lengths are used. The first array has 452 elements with center-to-center spacing of 0.216 mm (9.76-cm-length aperture). For comparison, we also simulate arrays with 694 elements (15-cm-length aperture) and 347 elements (7.5-cm-length aperture), but otherwise similar designs. The amplitude weighting is determined so that the main beam is steered to 5° at 5.6 MHz. The transmitted signal is a linear FM chirp with frequency swept from 1.2 MHz to 5.6 MHz. The targets are placed at 20 m, well beyond the intended maximum range, so that they are in the far field for all steering directions and all array lengths. The angular positions of the targets range from 6° to 24°. The speed of sound is assumed to be 1500 m/s for all simulations. Attenuation is not included. The transducer we simulate has a broadband, low-Q impulse response. The main effect of the transducer's transfer function is to reduce the amplitude of targets away from the resonance frequency of the transducer. Therefore, in the simulations we replace the transducer's impulse response with an impulse.

The operation of the linear amplitude-steered array has been simulated using the Field II program, developed by J. A. Jensen [25], [26]. Figure 2.4 shows three images of six point targets, using the three different arrays. Comparing the images in Figure 2.4, particularly for the targets at the higher steering angles, we can observe the tradeoff in axial and lateral resolution that depends on the length of the array. In order to quantify the tradeoff between axial and lateral resolution, resolutions were measured

from images of point targets. From the image in part (c) of Figure 2.4, we can see that both axial and lateral resolution improve with decreasing steering direction, corresponding to increasing frequency. The images in parts (a) and (b) show the improvement in lateral resolution with decreasing steering direction; however, the improvement in axial resolution with decreasing steering direction may be difficult to appreciate.

In addition to the resolution tradeoff that arises due to the size of the array, there is a tradeoff between axial and lateral resolution due to the processing. The length of the sliding FFT window limits the resolution of targets. A very short FFT window implies poor frequency resolution and therefore poor lateral resolution, but it also implies good time localization and therefore good axial resolution. The FFT window can be increased to improve lateral resolution until the fundamental limit on lateral resolution due to the size of the array is reached, but a long window means poor axial resolution. In parts (a) and (b) of Figure 2.4, the difficulty in seeing the degradation of axial resolution due to the length of the array is a result of the relatively long Hanning window used to form the images. For the two shorter arrays, the window length is longer than the achievable axial resolution for the higher frequency (smaller steering direction) targets.

Lateral and axial resolutions were measured from images formed using different length FFT windows in order to reduce the effect of processing on the measurements, so that we could measure the tradeoff in resolution only due to the size of the array. Axial resolution was measured by setting the window length to be short, 8.333 μs. Lateral resolution was measured by setting the window length to be long, 0.147 ms. The long window length was chosen by increasing the length of the FFT window until the improvement in lateral resolution at 6° was less than 0.5%. The images in Figure 2.4 are formed using a window length of 50.8 μs, which is a compromise between the two extremes.

Measurements were made of the -3-dB beamwidths in the lateral direction and the -3-dB signal length in the axial direction (Table 2.2). For all steering directions, lateral resolution improves with increasing array length, and axial resolution degrades

with increasing array length. Calculated and measured lateral beamwidths and axial resolutions are shown in Figures 2.5 and 2.6, respectively. Calculated beamwidths were found using Equation (2.11). Figure 2.5 shows that beamwidths measured from simulated data agreed with calculated beamwidths to a steering direction of 14°. At higher steering angles, corresponding to lower frequencies, the measured beamwidths were larger than calculated beamwidths. This agreement may be improved by using a longer FFT window. Axial resolution was calculated using Equation (2.17), where Q_{sig} was calculated using the predicted beamwidths for each frequency and assuming that the array had a flat frequency response. If a given steering direction was within the steered -3-dB beamwidth of a frequency f, then f was included within Δf used to calculate Q_{sig}. Figure 2.6 shows that the calculated and measured axial resolutions agreed well. The average Q_{sig} predicted for the 7.5-cm, 9.76-cm, and 15-cm apertures are 27.60 ± 0.094, 35.90 ± 0.021, and 55.18 ± 0.054, respectively. The average Q_{sig} measured for the 7.5-cm, 9.76-cm and 15-cm apertures are 28.5 ± 1.85, 36.1 ± 2.01, and 54.1 ± 5.45, respectively. For a given array length, Q_{sig} remains approximately constant over the band of frequencies used, which by Equation (2.17) means that for a given array length axial resolution depends only on wavelength.

Resolution was also measured in the vertical (out-of-plane) direction for the 452-element, 9.76-cm length array. In the vertical direction, resolution is only dependent on the height of the elements. For the simulation, we assumed the elements were twice as tall as they were wide, or 372 μm tall. Resolution can be predicted using Equation (2.19):

$$\alpha_{v,-3dB} = 2 * \tan^{-1}(0.4423\lambda/D) \tag{2.19}$$

where $\alpha_{v,-3dB}$ is the angle of spreading in the vertical direction, λ is the wavelength, and D is the height of the elements. This equation is derived from the beam pattern of a rectangular element. In the vertical direction and in the far field, the beam is defined by $\mathrm{sinc}(\frac{kD}{2}\frac{x}{z})$, where k is the wavenumber, D is the height of the element, x is the coordinate along the height but at the far-field plane, and z is the axial coordinate perpendicular to the array element. The -3-dB points are found when the argument

of the sinc function is equal to ± 1.3894. $\frac{x}{z}$ is equal to $\tan(\frac{\alpha}{2})$. Values for vertical resolution predicted and measured through simulation are presented in Table 2.3.

2.2.4 Summary of resolution study

The far-field array pattern was derived to show how amplitude-weighting causes frequency separation. Expressions were derived to predict axial and lateral resolution in the far field of the array. The theoretical values were used to show that both axial and lateral resolution were dependent on the length of the array. When operated in broadband mode as in the case for imaging, the axial resolution is directly dependent on the size of the array in terms of wavelength, which is different from the operation of conventional transducers. In fact, resolution in the lateral direction can be traded for resolution in the axial direction by changing the array size.

2.3 Time-Frequency Processing for the Formation of Images

Many time-frequency distributions have been studied for various purposes, each having its own benefits and drawbacks. In sonar imaging, time-frequency distributions have been used to identify targets based on characteristics of the distribution for the reflected signals [27], [28]; however, time-frequency processing has not been used to form an image of the target.

In preceeding discussions of the amplitude-steered array, we used the spectrogram to form images. Although the spectrogram is conceptually simple and easy to program, as the extension of the FFT, there are several drawbacks that make it possibly undesirable as the means for forming the image. In particular, there is an inherent tradeoff between time and frequency resolution, so that an improvement in one direction implies a degradation in the other.

Now we investigate the results for other time-frequency distributions. It is generally accepted that there is no known distribution that is ideal for all cases, but that the best distribution for an application must be chosen based on the properties of the signal and the criteria for the result. We compare five distributions, including the

spectrogram, for a test signal which is a simulated reflection from seven point targets. The distributions we have chosen are the spectrogram, the constant-Q spectrogram [29], the Wigner distribution [30], the smoothed pseudo-Wigner distribution [31], and the Choi-Williams distribution [32]. These distributions are among the most common distributions discussed in the literature.

First, we discuss properties of each of the distributions. In Section 2.3.2, we describe our test signal, and the basis for comparison of each of the distributions. Finally, we give results and conclusions. In the following discussion, the terms *time-resolution* and *frequency-resolution* are used; however, the terms *range-resolution* and *lateral-resolution*, respectively, could easily be substituted.

2.3.1 Time-frequency distributions

Two good reviews of time-frequency distributions and their properties are [31] and [33]. In the field of time-frequency analysis, we generally seek a distribution that describes the intensity of a signal simultaneously in time and frequency. In general, it is considered desirable to be able to integrate over all frequencies to get the instantaneous intensity at time t, and to be able to integrate over all time to get the instantaneous intensity at frequency ω.

Many different distributions exist. In fact, an infinite number of them can be generated by changing the kernel function in the following equation, which describes distributions that are the Fourier transforms of a local autocorrelation function:

$$D(t,\omega) = \frac{1}{4\pi^2}\int\int\int e^{-j\theta t - j\tau\omega + j\theta u}\phi(\theta,\tau)s^*(u-\frac{1}{2}\tau)s(u+\frac{1}{2}\tau)dud\tau d\theta \qquad (2.20)$$

where D is the representation of the signal in the time-frequency plane, ϕ is the kernel, s is the signal in the time domain, and s^* is its complex conjugate. The kernel may depend on time and frequency and may also be a functional of the signal. The distributions generated by different kernels satisfy different desirable properties and they produce different energy concentrations. The properties of a distribution can be

investigated by looking at the kernel.

$$\begin{aligned} \phi(\theta,0) = 1 \quad &\Rightarrow \quad \int D(t,\omega)d\omega = |s(t)|^2 \\ \phi(0,\tau) = 1 \quad &\Rightarrow \quad \int D(t,\omega)dt = |S(\omega)|^2 \\ \phi(0,0) = 1 \quad &\Rightarrow \quad \int D(t,\omega)d\omega dt = 1 \\ \phi(\theta,\tau) = \phi^*(-\theta,-\tau) \quad &\Rightarrow \quad D(t,\omega) \text{ is real.} \end{aligned} \tag{2.21}$$

$S(\omega)$ is the Fourier transform of the signal, $s(t)$. $|s(t)|^2$ and $|S(\omega)|^2$ are referred to as marginal densities. The first two equations give the conditions on the kernel so that the marginal densities are preserved, meaning that the instantaneous energy at a specific time or frequency can be calculated by integrations of the joint distribution through frequency or time, respectively. The third equation indicates that if the kernel is normalized to equal 1 at $(\theta,\tau) = (0,0)$ then the total energy is preserved.

If the kernel is independent of the signal, the distribution given by Equation (2.20) is bilinear in the signal, meaning that the signal enters the equation only twice. Bilinear distributions generally suffer from cross-terms which interfere with the interpretation of the distribution as an image. In our imaging application, we are interested in time and frequency resolution as well as low cross-term levels.

In the following discussion, both continuous and discrete expressions are given for the distributions. Generally, the distributions are formulated in the continuous domain, and discrete formulations are obtained from the continuous expressions. The transition to discrete expression is not unique. In many cases, the discrete distribution is periodic with period π rather than 2π, which is the usual period for a discrete signal. To avoid aliasing, the signal can be sampled at twice the Nyquist rate, or the analytic signal, which is zero for the negative frequency components, can be used to calculate the distribution.

Spectrogram

The STFT is the classic method for studying signals whose spectra vary with time. The spectrogram is computed as the magnitude-squared of the STFT. It is quadratic

in the signal and is given by the expression

$$D(t,\omega) = \left| \frac{1}{\sqrt{2\pi}} \int e^{-j\omega\tau} s(\tau) h(t-\tau) d\tau \right|^2 \tag{2.22}$$

where $h(t)$ is the window function used to calculate the STFT. The spectrogram can be expressed using the form of Equation (2.20), with the kernel defined as

$$\phi(\theta,\tau) = \int h^*(u - \frac{1}{2}\tau) e^{-j\theta u} h(u + \frac{1}{2}\tau) du \tag{2.23}$$

The spectrogram has the advantage that cross-terms are reduced to zero as long as the signal components do not overlap in time. And the spectrogram is a nonnegative definite distribution which leads to easy interpretation as an image. The spectrogram preserves the total energy of the signal if the window is normalized, but it does not preserve the marginal densities.

The time and frequency resolution of the spectrogram are determined by the window h used in the calculation. Different tradeoffs can be made by changing the window shape, although for a given window shape, the time and frequency resolutions are determined by the window length. The window cannot be narrow in both the time and frequency domain, so there is an inherent tradeoff in resolution for the spectrogram. Using a definition of resolution that includes both energy concentration and cross-term level, Jones and Parks showed that with an appropriate window, the resolution of the spectrogram could be better than that of some other distributions, including the Wigner distribution [34]. In our case, we define resolution as the energy concentration and consider cross-terms as an additional issue.

Constant-Q Spectrogram

The constant-Q distribution is a special case of the spectrogram, in which the window length is chosen based on the frequency sample being calculated. The number of cycles in the window is kept constant; therefore, a constant ratio between center frequency and bandwidth can be maintained. The constant-Q character is a better match to our received signals. As shown in Section 2.2.3, we expect our received signal to have a constant-Q quality, so that signals with a high center frequency also

have a wide bandwidth and therefore a short time duration. We expect signals with a low center frequency to have a more narrow bandwidth and therefore a longer time duration.

The expression for the constant-Q spectrogram is given by [29]:

$$D[k] = \left| \frac{1}{N[k]} \sum_{n=0}^{N[k]-1} W[k,n]s[n]exp(-j2\pi Qn/N[k]) \right|^2 \tag{2.24}$$

where s is the signal, $N[k]$ is the number of samples used to evaluate the expression for frequency sample k, $W[k,n]$ is a window function set to a Hamming window, for example, and Q is defined as $\frac{f}{\Delta f}$, where f is the frequency.

Expressed using the form of Equation (2.20), the constant-Q distribution is given by [35]

$$D(t,\omega) = \left| \frac{1}{2\pi} \int s(\tau)h((t-\tau)\frac{\omega}{\omega_0})e^{-j\omega\tau}d\tau \right|^2 \tag{2.25}$$

In the constant-Q spectrogram, cross-terms are reduced to zero unless the signal components overlap in time, as for the conventional spectrogram. However, the constant-Q spectrogram also retains some of the undesirable properties of the spectrogram. There is still a tradeoff between time and frequency resolution that is based on the window length. That tradeoff is quantified by a single value Q, the length of the window in terms of number of cycles.

This distribution has been used to analyze music signals, where chords have a constant distance between component frequencies, when the frequencies are plotted on a log scale [29]. The authors point out that they initially tried to use the FFT algorithm because of its computational simplicity; however, they found that plotting the information versus the logarithm of frequency to conform to the pattern expected from musical notes, they had too much information at high frequencies and too little information at low frequencies. In mapping the data from the linear to the logarithmic domain, at low frequencies they had few linear points corresponding to many logarithmic points. At the high frequencies, the opposite was true. In our imaging application, we plot the results of the FFT calculation versus θ where $\theta = \sin^{-1}(f_0 * \sin(\theta_0)/f)$. For constant frequency spacing which is given by the FFT, we have many points at small steering angles and few points at large steering angles.

If we want constant angular spacing at small steering angles, we have many frequency points to map to few angular points. Conversely, at large steering angles we have few frequency points to map to many angular points.

Wavelet transforms also have the "constant-Q" quality. The wavelet transform is given by

$$W(t,a) = \int s(\tau)\sqrt{a}\gamma^*(a(\tau - t))d\tau \tag{2.26}$$

where $\gamma(t)$ is the analyzing wavelet. This is the time-scale expression for the wavelet transform. In the time-frequency expression, the scale a would be replaced by the ratio of frequency to center frequency of the analyzing wavelet $\frac{f}{f_0}$.

Wigner Distribution

The Wigner distribution has received much attention because it is one of the oldest distributions and because it produces a time-frequency representation with the greatest resolution. But the Wigner distribution also has very high cross-terms. This distribution is given by

$$D(t,\omega) = \frac{1}{2\pi}\int e^{-j\tau\omega}s^*(t - \frac{1}{2}\tau)s(t + \frac{1}{2}\tau)d\tau \tag{2.27}$$

where, as before, s is the signal and s^* is its complex conjugate. The kernel is simply 1, which, from the properties given in Equation (2.21), implies that the distribution preserves the marginal densities and the total energy and that it is real. The Wigner distribution is not necessarily zero when the signal is zero, due to the cross-terms; however, it is zero before the signal starts and after the signal finishes. The distribution can have negative values.

The Wigner distribution is periodic with a period π. Therefore, to produce a representation that is free from aliasing, the signal must either be oversampled by a factor of two, or the analytic signal must be used. Using the analytic signal is beneficial for other reasons beyond avoiding aliasing. Cross-terms appear when two frequency components interfere with each other, which includes positive frequencies interfering with negative frequencies from the same signal. Using the analytic signal will reduce the number of cross-terms since there will no longer be negative frequency components.

The discrete version of the Wigner distribution is given by [31]

$$D(n,k) = \frac{1}{\pi} \sum_{\tau=-L+1}^{\tau=L-1} s^*(n-\tau) e^{-j4\pi k\tau/N} s(n+\tau) \tag{2.28}$$

where the limits are included for practical evaluation of the sum. The total length $2L-1$ should be equal to or longer than the duration of the signal.

Smoothed Pseudo-Wigner Distribution

The smoothed pseudo-Wigner distribution is an attempt to reduce the oscillating cross-terms in the Wigner distribution. The smoothed pseudo-Wigner distribution is given by

$$D(t,\omega) = \int\int g(t-t') H(\omega-\omega') D^{Wigner}(t',\omega') dt' d\omega' \tag{2.29}$$

where g filters in the time direction and H is a filter in the frequency direction. If the filter $g(t)$ is a delta function, the distribution is referred to as the pseudo-Wigner distribution.

Smoothing is applied independently in the time and frequency directions; therefore, we do not have the undesirable connection between the two resolutions as in the case of the spectrogram. Smoothing degrades the resolution in the direction in which it is applied, and the smoothing operation destroys the preservation of the marginal densities. For some smoothing filters, we can get a nonnegative definite distribution, but not with Gaussian filters. Therefore, we must choose between having a nonnegative distribution and preserving the marginal densities.

The discrete version of the smoothed pseudo-Wigner distribution is given by a discrete convolution of low-pass filters and the Wigner distribution in the time and frequency directions.

Choi-Williams Distribution

The Choi-Williams distribution was created to reduce cross-terms while preserving the marginal densities. The Choi-Williams distribution is given by

$$D(t,\omega) = \int e^{-j\omega\tau} \left[\int \frac{1}{\sqrt{4\pi\tau^2/\sigma}} exp\left(-\frac{(\mu-t)^2}{4\tau^2/\sigma} \right) s(\mu+\frac{\tau}{2}) s^*(\mu-\frac{\tau}{2}) d\mu \right] d\tau \tag{2.30}$$

where σ is the parameter used to control the properties of the distribution. Small σ implies more smoothing and reduction of the cross-terms. However, this also leads to greater loss of resolution. The loss of resolution is not independently controlled for the time and frequency directions because only a signal parameter σ is used. The Choi-Williams distribution has the drawback that it is difficult to reduce cross-terms if two signal components occur at the same time or the same frequency [33].

The discrete version of the Choi-Williams distribution is given by Equation (20) of [32]:

$$\begin{aligned} D(n,k) &= 2\sum_{\tau=-\infty}^{\tau=\infty} W_N(\tau) e^{-j2\pi k\tau/N} \times \\ &\sum_{\mu=-\infty}^{\mu=\infty} W_M(\mu) \frac{1}{\sqrt{4\tau^2/\sigma}} exp\left(-\frac{\mu^2}{4\tau^2/\sigma} s(n+\mu+\tau)s^*(n+\mu-\tau)\right) \end{aligned} \tag{2.31}$$

where $W_N(t)$ is a symmetric window that is nonzero in the range $t \epsilon [-N/2, N/2]$, and $W_M(t)$ is a rectangular window that is nonzero in the range $t \epsilon [-M/2, M/2]$, effectively reducing the limits on the sums.

2.3.2 Test signal and basis for comparison

The test signal is a simulated reflection from a set of seven point targets received by the amplitude-steered array operated in pulse-echo mode. The point targets are located at (6°, 4.0 m), (9°, 4.01 m), (12°, 4.02 m), (15°, 4.03 m), (18°, 4.04 m), (21°, 4.05 m), and (24°, 4.06 m), where the first coordinate is the angular position and the second coordinate is the range. The transmitted signal is a linear-FM chirp with frequency sweeping from 1.2 MHz to 5.6 MHz. The amplitude-steered array steers the 5.6 MHz signal to 5°. The length of the array is 9.76 cm.

The resolution of different distributions is measured as the -6-dB axial and lateral widths of each point target because the array is operated in pulse-echo mode. The highest level of a cross-term is also compared to the maximum target amplitude in the image. Each distribution is optimized within the limits of the parameters available so that the highest level of a cross-term is 20 dB below the peak and so that the axial and lateral resolutions of the point target at 6° are approximately equal and close to 1 cm.

The criterion for highest level of a cross-term was chosen based on the appearance of the images. Cross-terms above this level may interfere with the interpretation of the image. However, lowering cross-terms causes a blurring of auto-terms. In most cases we do not have the degrees of freedom to control all of these criteria, so subjective evaluation is used to produce the best image.

The respresentation of the signal on the time-frequency plane using these distributions will be taken as an image of the targets. Some of the distributions are not positive definite, which makes their interpretation as images difficult. In the cases where the distribution has negative values, the absolute value is taken before logarithmic compression and display of the images.

2.3.3 Results

The spectrogram was calculated using a Hanning window of 590 points or 28.8 μs. In the constant-Q spectrogram, the number of cycles in the window was set to 141. The Wigner distribution does not offer any parameters to optimize. In the case of the smoothed pseudo-Wigner distribution, the filters in the time and frequency directions were Gaussian in shape. They can be defined by the expression $exp(-t^2/\alpha^2 - \omega^2/\beta^2)$, where α is 3.4 μs and β is 125.7×10^3 rad/s. For the Choi-Williams distribution, the rectangular window W_M was 256 samples long, W_N was also a rectangular window 513 samples long, and σ was 0.75.

Measured lateral and axial widths are presented in Table 2.4. Because of the high cross-terms for the Wigner distribution, measurements for targets at 12° to 21° are made using images with only a single target present at a time. The target at 24° was not measured because it appeared at the edge of the image. The target at 24° was not measured for the Choi-Williams distribution because it was not visible in the image.

The images produced with the spectrogram and constant-Q distributions are shown in Figures 2.7 and 2.8. As expected, the spectrogram and constant-Q distributions did not have any cross-terms. The constant-Q distribution achieved better lateral resolution than the spectrogram, although the spectrogram generally produced

better axial resolution. The constant-Q distribution maintained equal lateral and axial resolution for each individual target, while the spectrogram produced much better axial resolution than lateral resolution for the targets at lower frequencies.

The Wigner distribution has no parameters for smoothing, and therefore the level of the cross-terms could not be reduced. An image formed using the Wigner distribution is shown in Figure 2.9. In the image, only the targets at 6° and 9° could be distinguished from the cross-terms. The Wigner distribution is still of interest as a measure of the achievable resolution. The resolutions presented in the table for targets at larger angles were measured using signals that contained only one target at a time.

The smoothed pseudo-Wigner distribution produced the best image of the distributions compared here in terms of combined lateral and axial resolution. The lateral resolutions were comparable to those of the constant-Q distribution, but the axial resolutions were smaller, by a factor of 2 in most cases. And the cross-terms were reduced to an acceptable level. An image is shown in Figure 2.10.

The Choi-Williams distribution was not able to match the performance of the smoothed pseudo-Wigner distribution. An image is shown in Figure 2.11. The Choi-Williams distribution suffers from the drawback that if two components with the same frequency are present at different times, or if two components with different frequencies are present at the same time, the cross-terms are difficult to remove [33]. In our case, the two targets at the lower frequencies overlap enough in time and frequency that the cross-term between them could only be lowered below 20 dB at the cost of great loss in resolution. Therefore, some of the cross-terms were allowed to remain in the image at higher levels. With only one parameter to control time and frequency smoothing and to control the cross-terms, we were unable to effectively trade axial resolution for better lateral resolution.

2.3.4 Summary of the time-frequency study

The performances of several time-frequency distributions were compared using a test signal, which represented a pulse-echo signal from seven point targets. By

moving from the spectrogram to other time-frequency distributions, we have shifted from a tradeoff in axial and lateral resolution to a tradeoff in axial resolution, lateral resolution, and cross-term level. The smoothed pseudo-Wigner distribution gave the best results, most likely because it had the most available parameters. Cross-terms were present at low levels. All of the distributions discussed here have kernels that are independent of the signal. Signal-dependent kernels may give better overall resolution, and they can be designed to give positive definite distributions while still satisfying the marginals.

2.4 Conclusions

The operation of the linear amplitude steered array has been described. The beam pattern has been given, and the use of the array for imaging has been described. A study of axial and lateral resolution has shown that both are dependent on the length of the array, and one resolution can be traded for the other by changing the length of the array. The data processing has also been studied to show that different time-frequency distributions will produce very different images. The smoothed pseudo-Wigner distribution gives the best overall resolution with reasonable cross-terms.

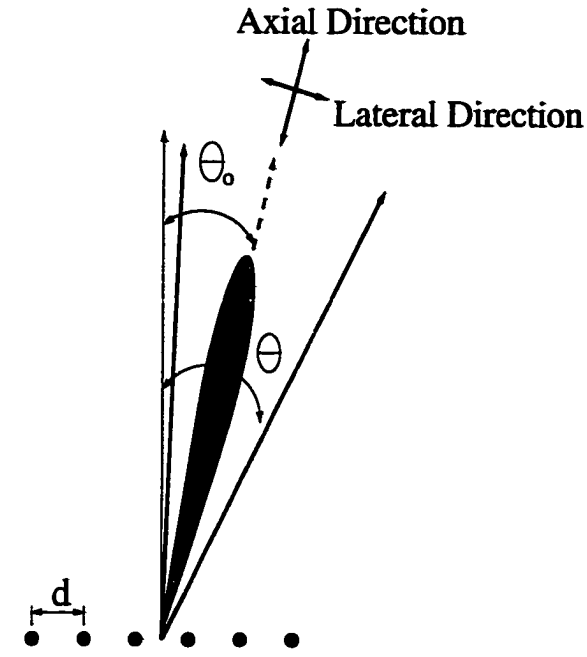

Figure 2.1: Diagram used to define variables for the derivation of the array field pattern.

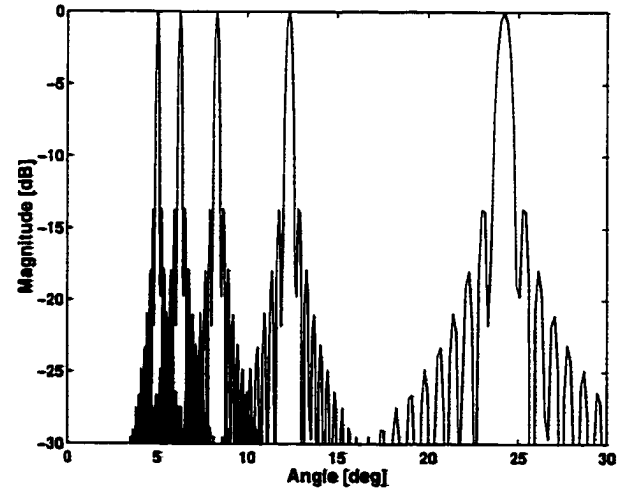

Figure 2.2: Beams from a 9.76-cm aperture steered to 5° at 5.6 MHz. Beams are shown for 5.6 MHz (5°), 4.5 MHz (6.23°), 3.4 MHz (8.25°), 2.3 MHz (12.25°), and 1.2 MHz (24°).

Table 2.1: Steering direction and beamwidth for a 9.76-cm, 452-element array designed to steer to 5° at 5.6 MHz.

frequency (MHz)	Steering Direction (deg)	Change in Steering Direction (deg)	Beamwidth (deg)
1.2	24.00	–	0.7104
1.5	18.99	5.01	0.5491
1.8	15.73	3.26	0.4496
2.1	13.44	2.29	0.3813
2.4	11.73	1.71	0.3315
2.7	10.41	1.32	0.2933
3.0	9.36	1.05	0.2631
3.3	8.51	0.86	0.2386
3.6	7.79	0.71	0.2184
3.9	7.19	0.60	0.2013
4.2	6.67	0.52	0.1867
4.5	6.23	0.45	0.1741
4.8	5.84	0.39	0.1631
5.1	5.49	0.34	0.1534
5.4	5.19	0.31	0.1448

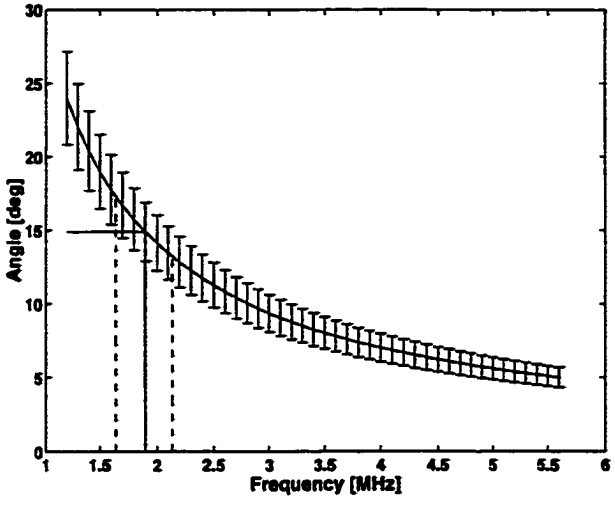

(a)

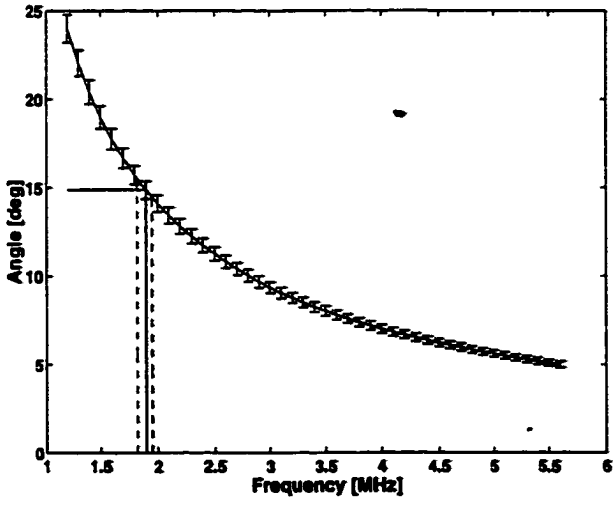

(b)

Figure 2.3: Lateral and axial resolution for (a) 1-cm-length and (b) 4-cm-length apertures. The curve shows the steering direction versus frequency. The error bars indicate the -3 dB beamwidth at each frequency. The vertical lines indicate how bandwidth decreases when array length is increased.

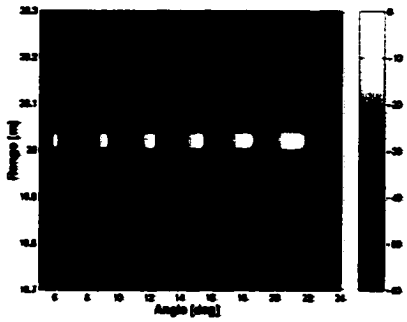

(a)

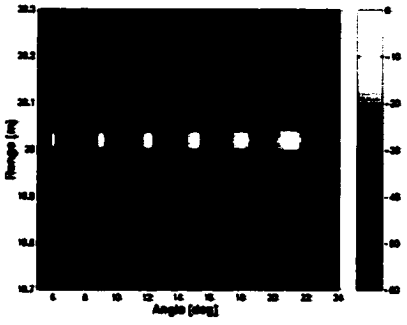

(b)

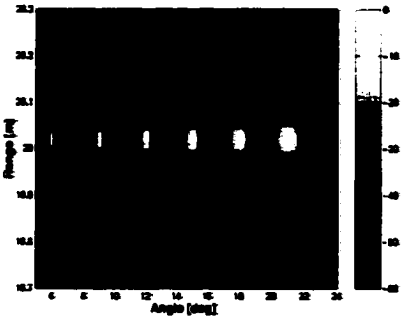

(c)

Figure 2.4: Images formed using simulated reflections from six simulated targets: (a) 7.5-cm, 374-element array, (b) 9.76-cm, 452-element array, (c) 15-cm, 694-element array. Time-Frequency processing is accomplished using the spectrogram with a 50.8-μs Hanning window.

Table 2.2: Axial and lateral resolution measurement results for three array lengths: 7.5 cm, 9.76 cm, and 15 cm. Axial resolution (AR) was measured from images formed using the spectrogram with an 8.333-μs Hanning window. Lateral resolution (LR) was measured from images formed using the spectrogram with a 0.147-ms Hanning window.

angle	6	9	12	15	18	21
f (MHz)	4.669	3.120	2.347	1.886	1.579	1.362
λ (mm)	0.321	0.481	0.639	0.795	0.950	1.10
LR (deg)						
7.5 cm	0.211	0.331	0.404	0.573	0.722	0.808
9.76 cm	0.174	0.254	0.316	0.440	0.539	0.613
15 cm	0.119	0.174	0.214	0.289	0.342	0.421
Δf (kHz)						
7.5 cm	165	110	75	70	60	50
9.76 cm	130	85	60	55	45	40
15 cm	95	55	40	35	30	20
AR (mm)						
7.5 cm	3.845	7.690	8.972	10.25	11.54	15.38
9.76 cm	6.409	8.972	11.54	12.82	15.38	17.94
15 cm	8.972	12.82	16.67	19.23	24.35	26.92

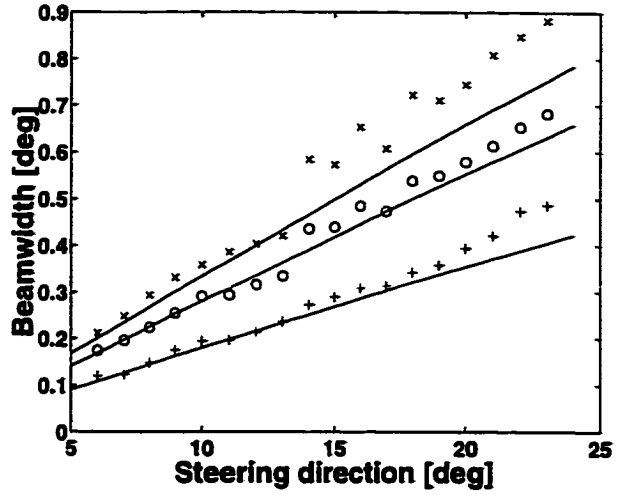

Figure 2.5: Comparison of calculated and measured beamwidths. Measured values are given for 7.5-cm-length array (x), 9.76-cm-length array (o), and 15-cm-length array (+). Calculated values are indicated by the solid lines.

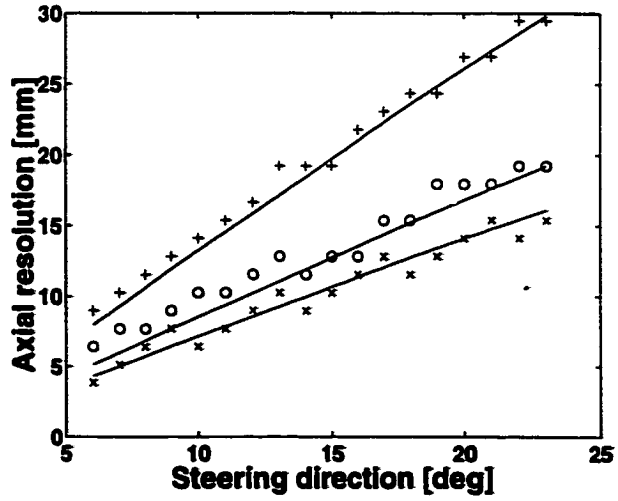

Figure 2.6: Comparison of calculated and measured axial resolutions. Measured values are given for 7.5-cm-length array (x), 9.76-cm-length array (o), and 15-cm-length array (+). Calculated values are indicated by the solid lines.

Table 2.3: Measured and predicted vertical (out-of-plane) resolution for the 452-element, 9.76-cm-length linear array.

Steering Direction (deg)	Predicted Resolution (deg)	Measured Resolution (deg)
6	41.8	44
9	59.5	60
12	74.4	76
15	86.8	92
18	96.9	100
21	105.3	110

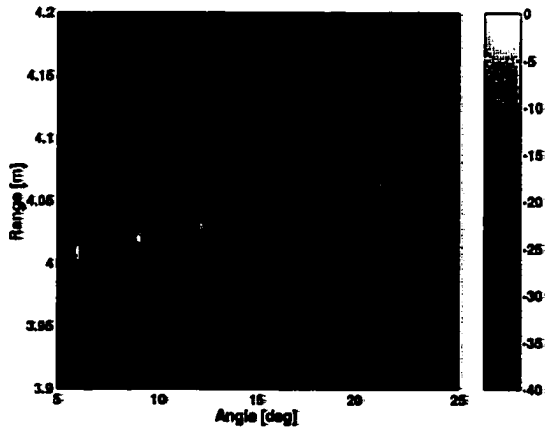

Figure 2.7: Image produced using the spectrogram. The spectrogram was calculated with a Hanning window of 590 points or 28.8 μs.

Table 2.4: Axial and lateral resolution measurement results for different distributions.

Lateral Resolution (mm)							
angle (deg)	6	9	12	15	18	21	24
spectrogram	11.8	19.5	30.6	45.7	66.1	81.8	102
constant-Q	11.1	17.2	23.2	31.0	37.6	42.6	48.7
Wigner*	11.1	16.6	21.5	28.4	34.7	38.5	–
SPWD	11.6	17.1	22.9	30.9	38.9	45.8	53.9
Choi-Williams	16.8	24.9	34.8	51.6	88.9	87.1	–
Axial Resolution (mm)							
angle (deg)	6	9	12	15	18	21	24
spectrogram	11.2	11.2	14.9	16.8	18.7	18.7	24.3
constant-Q	11.0	18.3	23.8	29.3	34.8	40.3	45.8
Wigner*	4.76	8.02	10.2	12.7	14.4	17.7	–
SPWD	7.07	9.41	12.2	14.1	16.0	19.0	21.4
Choi-Williams	7.10	9.89	13.0	14.8	15.6	20.6	–

*Values for Wigner distribution were measured using images with one target present at a time.

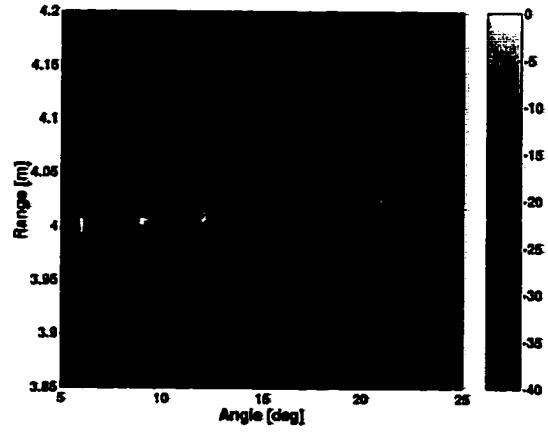

Figure 2.8: Image produced using the constant-Q spectrogram. The constant-Q spectrogram was calculated with a Hanning window containing 141 cycles.

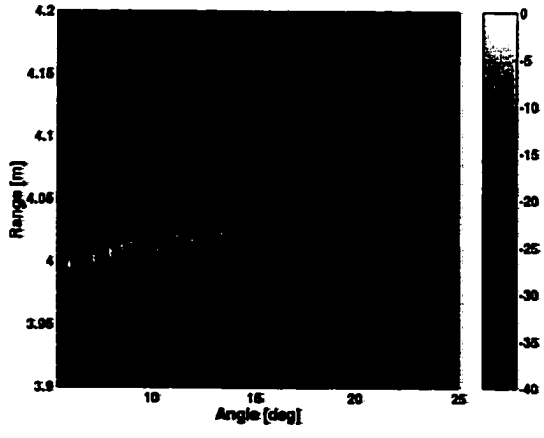

Figure 2.9: Image produced using the Wigner distribution. There were no parameters available for the optimization.

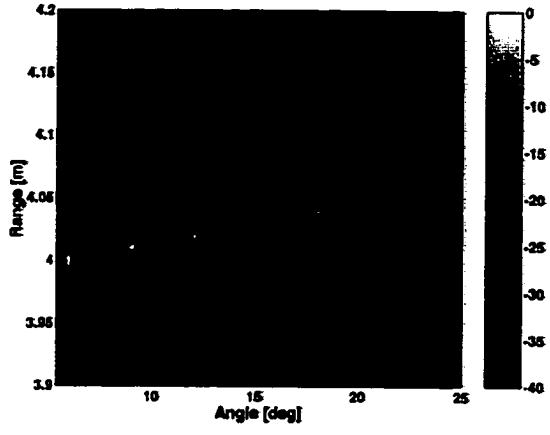

Figure 2.10: Image produced using the smoothed pseudo-Wigner distribution. Smoothing in both time and frequency directions was accomplished using filters with Gaussian shape, $\alpha = 3.4$ μs and $\beta = 125.7 \times 10^3$ rad/s.

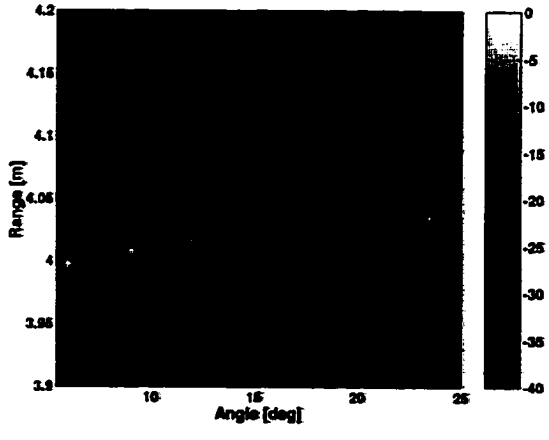

Figure 2.11: Image produced using the Choi-Williams distribution, $\sigma = 0.75$.

CHAPTER 3

TWO-DIMENSIONAL AMPLITUDE-STEERED ARRAY

The linear amplitude-steered array was discussed in detail in Chapter 2 to introduce issues of array operation, image formation, and resolution. We now extend the discussion to the implementation of the amplitude-steered array as a two-dimensional array for fast volumetric imaging.

This chapter first gives an introduction to the operation of the two-dimensional array, briefly describing the current application. Then the layout of the array is discussed along with the beam pattern produced. Next the data collection is described along with its simulation. At this point the achievable resolution of the array can be compared with the resolutions achieved using different time-frequency processing. Finally, the image formation algorithms are presented along with resulting images.

3.1 Introduction

We give a brief description of the application and array operation here to provide a context for the more detailed discussions that follow. The goal is to image a sector from 3 to 5 m in front of the array, with a resolution voxel of 1 cm. The sector will be 20°-wide in the vertical direction and 30°-wide in the horizontal direction. The resolution requirement leads to the choice of 1 to 5 MHz as the desired operating frequency range. The array is intended to be used within a diver-held sonar camera for real-time detection and identification of submerged mines. We expect the mines to be metallic targets suspended in the water or sitting on the soft bottom of the water body, with total size of apprximately 50 cm and features on the order of 1 cm.

The major constraint on acoustic volumetric imaging that is addressed by this array is the slow data acquisition due to the speed of sound in water. The speed of sound in seawater is approximately 1500 m/s. A pulse requires 6.7 ms to travel 5 m and return. Because we wish to image to a range of 5 m, we must be able to collect all the data with a small number of transmit pulses. Using one pulse per scan of the volume of interest will allow us to have a frame rate of approximately 150 volumes/s. The time required to process the data will reduce the frame rate.

To image a volume of interest with a single transmit pulse, information must be contained within the received signal to give vertical, horizontal, and range position of the target. The range of the target will be obtained from the time elapsed until the reflected signal is received. The vertical position information will be determined by the frequency of the returned signal. The horizontal position of the target will be found by using conventional, linear phased array processing of the signals from the columns of the array.

To insonify the entire volume of interest with one pulse, a subset of the two-dimensional array elements will be used as transmit elements. To insonify an entire region with a single transmit pulse, with a conventional array, the transmitter would have to be small in both the horizontal and vertical directions. For the two-dimensional amplitude steered array, using a set of elements that is narrow in the horizontal direction and wide in the vertical direction will give a beam that is wide in the horizontal direction and narrow in the vertical direction. But in the vertical direction, the narrow beam will be scanned as the frequency changes.

3.2 Array Design

The two-dimensional array is a matrix of elements. We refer to the vertical columns of elements as "staves," and we refer to the horizontal rows of elements as "rows." The amplitude steering occurs only in the vertical direction.

The following array designs were developed by colleagues at the Applied Research Laboratory at the Pennsylvania State University. In this section, we present each of the designs and discuss the optimality of the final array design.

3.2.1 Linear array design

The original layout for the two-dimensional amplitude-steered array was based on the implementation of amplitude weighting for the linear array. Amplitude weighting for the linear array was accomplished, not by scaling the signals from point sources/receivers, but by dividing up the available area of a single piezoelectric crystal according to the ratio of the weights, as shown by Figure 3.1. We show how this figure is derived by first imagining that we could phase a continuous rectangular transducer to steer its main beam. We use the following equation to determine the phase at each point on the transducer:

$$H_{continuous}(\theta) = \int e^{jk_0 x \sin(\theta_0)} e^{-jkx\sin(\theta)} dx \tag{3.1}$$

where θ is the angular argument of the beam pattern, k_0 is the wavenumber at the design frequency, θ_0 is the design steering angle, and x is the spatial position along the transducer. We separate the phase into its real and imaginary parts to obtain

$$H_{continuous}(\theta) = \int \cos(k_0 x \sin\theta_0) e^{-jkx\sin\theta} dx + j \int \sin(k_0 x \sin\theta_0) e^{-jkx\sin\theta} dx \tag{3.2}$$

where the first term of the sum corresponds to the cosine array and the second term corresponds to the sine array. The weightings, $\cos(k_0 x \sin\theta_0)$ and $\sin(k_0 x \sin\theta_0)$, are the continuous versions of the sampled weightings, $\cos((2n-1)\phi)$ and $\sin((2n-1)\phi)$, for the array of point sources/receivers of Chapter 2, where $\phi = k_0 d \sin\theta_0/2$.

Part (a) of Figure 3.1 shows the regions belonging to the cosine and sine arrays for the continuous transducer. The solid line represents the cosine array, and the dashed line represents the sine array. The weighting is acheived by changing the shape of the transducer. In part (b) of Figure 3.1, we show that the two different weightings must occupy the same space. In Figure 3.1(c) we show that the sharing of space is achieved by using a cosine weighting and a (sine + cosine) function for weighting.

3.2.2 Two-dimensional array design

The original two-dimensional array was essentially a painting of the one-dimensional array onto the two-dimensional array, as shown in Figure 3.2. The maximum array

dimensions are 55 by 52 elements. The center-to-center spacing is 2.11 mm, giving an array that is approximately a circle with a radius of 11 cm. In Figure 3.1, the frequency separation is in the horizontal direction, and in Figure 3.2, the frequency separation is in the vertical direction. Although the design is largely based on the linear implementation, there are some differences which take advantage of the flexibility of using an array. The sine regions, which had been implemented as a (sine+cosine) function in the one-dimensional array, include some elements in the center staves of the array. This modification is necessary because the center two staves will be used as the transmit array. In order to approximate the beamsteering of the whole array, the center two staves must include some sine elements.

This array design was unsatisfactory because of the presence of high sidelobes, as shown in Figure 3.3. The array was designed to steer to 30° at 100 kHz, and it was to be used for a frequency range of 50 kHz to 400 kHz. Therefore the beam pattern shown is for 400 kHz, where grating lobes are most likely to occur. The 400-kHz beam is steered to approximately 7°. Additional major lobes appear at 49.8° in the vertical direction and ±1.59° in the horizontal direction, and they are only 12.4 dB below the main lobe.

3.2.3 Alternating element design

New designs were conceived in an attempt to lower the grating lobes. The next iteration used increased mixing of the two different types of elements. The linear array implementation was no longer considered. Instead the design is a more direct implementation of the concepts from Chapter 2. Now the point sources/receivers of the linear array will correspond to rows of the two-dimensional amplitude-steered array. This correspondence is shown in Figure 3.4. On the left, the figure shows a linear amplitude-steered array, as discussed in Chapter 2, except that the frequency steering is now in the vertical direction. Recall from Chapter 2 that the usual electronic steering has been divided into two sets of weights, one phase-symmetric consisting of $\cos((2n-1)\phi)$ terms, and one phase-antisymmetric consisting of $\sin((2n-1)\phi)$ terms, where $n\epsilon[-\frac{N}{2},\frac{N}{2}]$ is an index used to enumerate the elements and there are

an even number of elements in the array. For the two-dimensional array, the weighting is accomplished by selecting the number of elements in each row that are connected together as sine or cosine elements. In this way the phase-symmetric and phase-antisymmetric arrays share physical space. On the right, we show that each point source/receiver of the linear array corresponds to a row of the two-dimensional amplitude-steered array. Each element of the row must be assigned to be a cosine or sine element so that the proper $\cos((2n-1)\phi)$ and $\sin((2n-1)\phi)$ weightings are maintained. As the $\cos((2n-1)\phi)$ and $\sin((2n-1)\phi)$ terms may represent positive or negative values, in each row, there are either positive cosine or negative cosine elements, not both. Also, there are either positive sine or negative sine elements, not both. The numbers of each type of element in a row were determined by the equations

$$N_C(n) = \frac{N_n^{max}}{1.414} |\cos((2n-1)k_0 d/2 \sin\theta_0)| \tag{3.3}$$

$$N_S(n) = \frac{N_n^{max}}{1.414} |\sin((2n-1)k_0 d/2 \sin\theta_0)| \tag{3.4}$$

where the weights of Equation (3.2) have been discretized assuming an even number of rows, where N_C is the number of cosine elements, N_S is the number of sine elements, N_n^{max} is the maximum number of elements in the n^{th} row, d is the spacing between the rows, k_0 is the design wavenumber, and θ_0 is the design steering angle. For our arrays, N_n^{max} depends on the row number to account for the circular aperture. Elements of each row were assigned alternating type, sine or cosine, along the row until the maximum of one type is reached, i.e., at element $2 * \min\{N_C, N_S\}$. The row was completed with the remaining elements of the other type.

This design resulted in very high sidelobes. Figures 3.5 and 3.6 show the second array layout and the resulting beam pattern at 5 MHz, for an array that was designed to operate between 1 and 5 MHz and steer to 5° at 5 MHz. The array diameter is 10 cm. The center-to-center spacing of rows is 215.9 μm, and the center-to-center spacing of staves is 254 μm. Grating lobes in the vertical direction resulted from gaps at the edge of the array where some rows had more elements than others. Grating lobes in the horizontal direction resulted from the alternating elements. There are multiple lobes above -15 dB relative to the main lobe. The maximum grating lobes occur

at $-36.2°$ in the horizontal direction and $-51.2°$ and $37.6°$ in the vertical direction. These lobes are only 10.7 dB below the main lobe.

3.2.4 Random array design

The final array design was based on using a random assignment of elements. As with the alternating element design, a certain number of sine elements and a certain number of cosine elements are required in each row. The proportion of these elements is the same as with alternating elements in order to accomplish the beamsteering. However, the positioning of the elements within the row has been made random. Each element of the array was given a certain probability of being a cosine element and a certain probability of being a sine element. The sum of these probabilities does not equal one for every row. It is also possible for the element to be nulled, or not used, in order to keep the proper relative weighting between rows. A random number generator was used to assign element type. In the alternating array design, null elements all occurred at the edge of the array. In the random array design, these elements occur anywhere in the row. This array design led to a greatly reduced peak sidelobe level but an increased average sidelobe level. Figure 3.7 shows the array layout used for the simulations, and Figure 3.8 shows the beam pattern produced. There are no large sidelobes; however, the pedestal level is approximately -44 dB.

The optimal beam pattern we are trying to achieve is that of an electronically steered array of the same size. In the optimal array layout, each element has both a cosine weight and a sine weight, implemented as an electronic phase. For the amplitude-steered array, each element contributes either to the cosine or the sine weighting, but not to both. Therefore, we are essentially designing two sparse arrays, one cosine and one sine array. These two arrays cannot be designed independently because each element of the combined array can only have one type.

Patterns of sparse arrays are characterized by grating lobes or sidelobe pedestal level. According to Steinberg's work [36], [37], the average sidelobe level of the intensity pattern is approximately N^{-1}, where N is the number of elements in the array. Steinberg analyzed and compared the peak sidelobe level of sparse arrays,

designed using random placement of elements and algorithmically aperiodic arrays. He found that both produced the same mean sidelobe level, but that the variance of the random arrays was much smaller than that of algorithmically designed arrays, when all of the algorithmically designed arrays were compared as a group regardless of design method. The large variance of the nonrandom design methods means that it is possible to achieve designs where the peak sidelobe level is significantly lower than that achieved by most designs. The method most likely to produce a better design than the random design is dynamic programming, where the location of the first element is chosen at random. Subsequent elements are positioned to produce the best result, given the previous element positions. For the random arrays, the small variance indicates that it is difficult to obtain an improvement in the peak sidelobe level by trial and error design. However, it is also less likely that one iteration will produce a beam pattern with an inordinately high sidelobe.

The random array design is not necessarily optimal because there may be some nonrandom design that produces a lower peak sidelobe level. However, the random array design produced a beam pattern whose main lobe has the same width as the main lobe of the full array. And the random array has no grating lobes or large sidelobes. The predicted average sidelobe level is -51.12 dB. The measured average sidelobe level is -44 dB. The peak sidelobe level is only 2.3 dB above the mean.

The random array may be made even more sparse, in order to reduce the number of elements that need to be connected. For example, reducing the probabilities that an element is a sine or cosine element by a factor of 50 (increasing the probability that an element is not used) reduces the total number of elements that need to be connected by a factor of 50. The main lobe width does not change, nor does the steering angle; however, the mean sidelobe level is increased to 34 dB below the main lobe. An example of an array layout and a cut through the beam pattern at the main lobe for this very sparse random design are shown in Figures 3.9 and 3.10. A more sparse design may be desirable when fabrication of large two-dimensional arrays is difficult.

3.3 Data Collection and Simulations

Data collection with the random two-dimensional amplitude-steered array will proceed as follows. In front of the array will be a cylindrical lens with a line focus at four meters, focusing in the vertical direction. A linear FM chirp pulse is transmitted from the center two staves. At a given frequency, the transmit beam is wide in the horizontal direction and narrow in the vertical direction. The beam is steered in the vertical direction, according to its frequency. The reflected signal is then received by the whole array. Signals from individual staves are digitized separately and stored for delay-and-sum beamforming in the horizontal direction.

Data collection with the random two-dimensional amplitude-steered array is simulated using the Field II program by J. A. Jensen [25], [26]. A block diagram of the simulations is shown in Figure 3.11. The code which accomplished this simulation is given in Appendix B. Data collection was simulated in four parts: cosine elements transmitting, cosine elements receiving; cosine elements transmitting, sine elements receiving; sine elements transmitting, cosine elements receiving; and sine elements transmitting, sine elements receiving. If targets were known to exist only at positive vertical angles, only one of the four parts was required. The array description, point target locations, and point target amplitudes were generated by different programs and stored as Matlab files. Within Field II, the transducer characteristics were defined and focusing delays were input. Then Field II generated the output voltage signal by first determining the spatial impulse response of the array at the locations of the targets, and then convolving that response with the transducer excitation and impulse response.

The Field II program assumes a linear frequency dependence of attenuation, which is an appropriate assumption for tissue but not for water. In order to include attenuation in the simulation, the target strengths were modified according to their range and vertical position in the field. The targets were generally placed at 4 m, centered at 0° horizontally.

The target used for these simulations was designed to include some features of a mine, including representations of bolts and a slanted face. A diagram of the target

with dimensions is shown in Figure 3.12. The bolts are of a size to test the resolution limits. We would like to be able to resolve features that are 1 cm in size. The slanted face is intended to provide information about depth resolution. The original model of this target was done at the Applied Research Laboratory using AutoCAD. We use the model by assuming the node positions of AutoCAD are point targets in the Field II program. The definition of the bolts required many nodes. Therefore, they are highly dense targets, more dense than the rest of the target. A diagram of the target in terms of its point-target representation is shown in Figure 3.13.

Simulating the actual data collection, a linear FM chirp is transmitted by the center two staves of the array. The reflected signals are received by each of the elements in a stave, and the sum of the signals from elements in the same stave is calulated using the appropriate phase shift to simulate a lens focused at four meters in the vertical direction. The stave signals are stored in a matrix. One direction of the matrix is time and the other dimension is stave number. Before storing the time signal from a stave as one column of the matrix, appropriate time delays are added for focusing in the horizontal direction.

3.4 Three-Dimensional Data Set

Forming the complete three-dimensional data set, following the data simulation, consists of two steps. First, the signals from individual staves must be processed to give horizontal position information. Second, time-frequency processing is performed on signals corresponding to each horizontal steering direction to give vertical position and range information.

3.4.1 Horizontal position information

Once the signals from each stave are received, the raw data are processed to give horizontal position information. This processing is shown in the block diagram in Figure 3.14. The focusing delays do not change with steering direction, so they are applied within the Field II program. Further processing is accomplished separately in Matlab. Beamsteering is accomplished using the Radon transform. The discrete

Radon transform sums through a matrix at different angles, resulting in beams steered several directions [38].

The output from the array, with focusing delays applied, is a two-dimensional matrix, with stave along one direction, and time along the other. Once the Radon transform is complete, we have a matrix of one time signal for each horizontal steering direction. For a complete set of volumetric data, we then apply time-frequency processing to the time-signal from each horizontal steering direction.

3.4.2 Time-frequency processing

Range and vertical position information are determined using time-frequency processing. We implement the spectrogram and the smoothed pseudo-Wigner distribution (SPWD). The spectrogram is the most likely to be implemented for early arrays. However, in Chapter 2, the analysis of the linear array using different time-frequency distributions showed that the SPWD gave the best overall results.

Parameters such as the filter lengths and shapes were determined by forming images of the model mine target and optimizing those images for visual appearance. Then a resolution analysis was performed to determine the resolution provided by the distribution used.

In the case of the spectrogram, the length of the window used for the linear array in Chapter 2 was not ideal. It was based on forcing the target at 6° to have equal resolution in the axial and lateral directions. A better image is produced by increasing the length of the window, so that some of the range resolution is sacrificed for better vertical resolution for the targets at larger angles. The final window length chosen was 1024 samples or 50 μs.

The parameters previously selected for the smoothed pseudo-Wigner distribution allowed us to lower cross-terms to almost −30 dB while having better range resolution than specified. The filters used for smoothing in the time and frequency directions were Gaussian windows, described by the expression $exp(-t^2/\alpha^2 - \omega^2/\beta^2)$, where α is 3.4 μs and β is 125.7×10^3 rad/s.

3.5 Resolution Analysis

As with the linear array, the image resolution is dependent not only on the size of the array, but also on the processing used to form the images. First, we describe the resolution that is achievable by the array, without considering the processing. Then we will consider the resolution obtained when using the spectrogram or SPWD.

In the range direction, we will call the resolution *range resolution*, which we previously called *axial resolution*. Range resolution will be given in millimeters. It is dependent on the bandwidth of the received signal, as in the case of the linear array. What we had previously called *lateral resolution* is now called *vertical resolution*. We will also measure horizontal resolution. Vertical and horizontal resolutions are measured in degrees. In the vertical direction, the lateral resolution is very much like that of the linear amplitude-steered array. The resolution will get worse as the vertical position increases because we have chosen to have the high frequencies steered downward. In the horizontal direction, the resolution is similar to that of an electronically phased array.

The theoretical description of resolution is complicated by the multiple frequencies and multiple foci in the horizontal direction. For the lowest frequencies used, the volume of interest is in the far field; therefore, focusing will not be effective. Horizontal resolution could be estimated by determining the far-field beam spread of the array. For the highest frequencies, the region of interest is in the near field. Six different focal regions are used. A theoretical value for horizontal resolution can be determined at the location of the foci. At other locations, the diffraction-limited spreading must be taken into account. In the far field, range resolution is not dependent on range. In the near field, there is some dependence. Vertical resolution depends on the frequency separation. Resolution is investigated through simulations because of the many different cases within our volume of interest.

Range resolution is found using the time signal after the Randon transform is preformed. Envelope detection is performed using the Hilbert transform. Then the envelope is log compressed and the points 6 dB below the maximum are found. The time difference between these points is then converted to distance using the speed of

sound. Vertical resolution is found by first calculating the magnitude-squared of the FFT of the entire received time signal. Those data are then log compressed and the frequency values 6 dB below the maximum are found. That frequency information is then converted to angular information. The −6-dB level is used because the array is used in pulse-echo mode. Finally, horizontal resolution is found by calculating the Radon transform for a range of angles around the target's actual angular position. This calculation forms part of an image in the horizontal angle/range plane. The horizontal resolution is then the horizontal size of the point target in the image measured by −6-dB points.

Resolutions measured from simulated data are given in Appendix C. In general, horizontal resolution stays fairly constant due to the multiple foci. At very high frequencies (small steering angles), vertical resolution is better than horizontal resolution at closer ranges, but comparable to horizontal resolution at far ranges, because there is only one focus in the vertical direction. At low frequencies, vertical resolution is fairly stable because in the far field focusing does not have any effect. Also for low frequencies vertical resolution is better than horizontal resolution because of the transmit-receive combination. The transmit beam pattern is wide in the horizontal direction, but narrow in the vertical direction. The comparison between vertical and horizontal resolution shows one of the advantages of the amplitude-steered array over a system that uses a broad transmit and a conventional phased array to receive. Better resolution in the vertical direction than in the horizontal direction is a result of having a narrow transmit beam in the vertical direction for each frequency.

Resolutions are also measured for data following time-frequency processing. In this case, only range and vertical resolutions are measured. The Radon transform is calculated for the appropriate steering angle, then two-dimensional images are formed using either the spectrogram or the SPWD. Resolutions are measured from the image as the −6-dB range and vertical extent of the pulse spread function. These results are presented in Appendix D.

Plots showing the comparisons of range and vertical resolutions for the case of no processing or processing with the spectrogram and SPWD are given in Figure 3.15.

Part (a) shows the range resolutions for the three cases. The solid line respresents the results for no processing, and should be the lowest line for all angles. However, the dotted line, representing the results for the SPWD, dips below the solid line. This is a result of measurement error. The SPWD can produce resolution very close to the limit of no processing, but it cannot do better. Part (b) shows the results for the vertical resolution. Again, the SPWD resolution approaches that of no processing. For both range and vertical resolution, the spectrogram results are not as good as the others. For comparsion, in (b), the dash-dotted line shows the horizontal resolution measured with no processing. It is worse than the resolution in the vertical direction because the transmit in the horizontal direction is broad.

3.6 Image Display

Using the Radon transform to get horizontal position information and the SPWD to get range and vertical position information, we form a three-dimensional data set. The three-dimensional data set is reduced to two dimensions for display. The methods for this reduction are surface rendering, projection images, or slice images.

3.6.1 Surface rendering

One method to reduce the three-dimensional data set to a two-dimensional image is surface rendering. An image may show the maximum value for a particular direction if the maximum is above a threshold value. Similarly, the depth location of the maximum value could be displayed. We feel that this is valuable because the targets of interest are metallic and so most of the energy reflected will be from the front surface of the target, not from within the target.

The image produced using either of the above models shows vertical position of the target versus horizontal position. Range information is lost or displayed as image brightness. Two-dimensional data for each horizontal steering direction is reduced to a single row, which can be accomplished in two ways. In the first case, the maximum return from each vertical direction is shown. In this instance, there is no range resolution. In the second case, the range of the maximum return is shown for each

direction, as long as the maximum is above a certain threshold value. The range resolution is displayed as color in the image, but different reflectivities of targets are lost.

Examples of these image formation methods are shown in Figures 3.16 and 3.17. In both cases, the images produced using the spectrogram and SPWD are similar. In Figure 3.16, which shows the maximum return for each steering direction, the ring of bolts at the bottom of the target is visible; however, the slant is lost. In Figure 3.17, which shows the range of the maximum return for each steering direction, the bolts are noticeable as is the slant, which appears to get darker as it gets farther away. Dark patches appear within the target as a result of the low and nonuniform point target density from the model.

3.6.2 Projection and slice images

Projection and slice images are an alternative to surface rendering. Slice images display a slice through the three-dimensional data set. Projection images integrate through one direction to display the other two as an image. An image of vertical versus horizontal position is formed by summing through the range information. An image of range versus horizontal position is formed by summing through the vertical position information. And an image of vertical position versus range is formed by summing through the horizontal information.

Slice images pick a plane from the three-dimensional data set for display. Sample images using cuts through the data are shown in Figures 3.18, 3.19, and 3.20. Figure 3.18 shows a horizontal slice for the spectrogram and SPWD processing. The horizontal slice was made at the frequency 3.98 MHz because the high frequencies provide the best resolution. The overall shape of the target in the horizontal plane is visible in the SPWD image, but difficult to discern from the spectrogram image. Figure 3.19 shows a slice at a particular range, close to the front of the target. The spectrogram image shows more of the target in the vertical direction because the range resolution of the spectrogram is not as good as that of the SPWD. Figure 3.20 shows a vertical slice through the target and perpendicular to the array, using the

array broadside direction. Both the spectrogram and SPWD images clearly show the outlined shape of the target. The SPWD image is sharper, but with streaking in the vertical direction. In all of the slice images, data are thrown out rather than losing resolution in the data that are displayed. Slice images would perhaps be more useful if combined with a volume rendered image.

Projection images show the same planes as slice images, but with greatly reduced processing. One way to form projection images is to begin with the full three-dimensional volume of data; however, the processing can be simplified. As described above, forming the three-dimensional data set requires time-frequency processing for each horizontal beam. The projection images can be formed much faster using different processing. We already have the horizontal position information from the Radon transform. The image of range versus horizontal position is formed without doing a Fourier transform. We do not need frequency information, and by using the time signal, we already have range information. The image of vertical position versus horizontal position is formed by taking a single Fourier transform of the whole received signal for each steering direction. Since we do not need any range information, we do not need time-frequency processing. Instead, we can use a single, long FFT. Finally, to form the image of vertical position versus range, we need to do the time-frequency processing. But, we do not need to perform the calculation for every horizontal beam. Instead, we can sum through the horizontal beams first, and then calculate the time-frequency distribution once. Sample images formed using each of these methods are shown in Figures 3.21, 3.22, and 3.23. Figure 3.21 shows the projection images through the vertical direction. From these images, we can see the bright reflections of the bolt targets at the top of the images. Then the overall shape of the target in the horizontal plane can be appreciated. We can also see that the SPWD gives a sharper image than the spectrogram. Figure 3.22 shows the projection through range. From these images the differences between the SPWD and the spectrogram are not apparent. Both show bright bolts and overall shape of the target. Figure 3.23 shows the projection through the horizontal direction. Again, the SPWD image is much sharper than the spectrogram image. The overall shape of the target in the

vertical direction is apparent. The target appears "filled in" compared to the slice image in this plane because the projection sums many planes, including the edges of the target. In each of these projection images, one dimension of resolution that is present in the data is given up to display the image.

3.7 Discussion

In this chapter, we have extended the concepts of Chapter 2 to show how the amplitude-steered array can be used for real-time three-dimensional imaging. We began by describing our application as it affects the implementation of the imaging system. Then we discussed the layout of the array, including early versions of the array to show some design tradeoffs. The random array design produced the beam pattern with the lowest peak sidelobe level, and therefore was the design chosen. After describing how data were collected and simulated, an analysis was performed to show the resolution achieved using the amplitude-steered array. Because of the frequency separation in the vertical direction, the transmit beam did not have to be wide in the vertical direction. As a result, the resolution in the vertical direction is better than that in the horizontal direction. Finally, we discussed how images would be displayed. Volume rendering methods were not considered because of the large amount of computation required. Surface rendering techniques that require the identification of surfaces were not considered because noise limits the performance of these methods, and often in acoustic imaging, surfaces do not produce large reflections because of their orientation relative to the insonifying beam. The form that provided the most information while allowing us to reduce the amount of processing was the projection images.

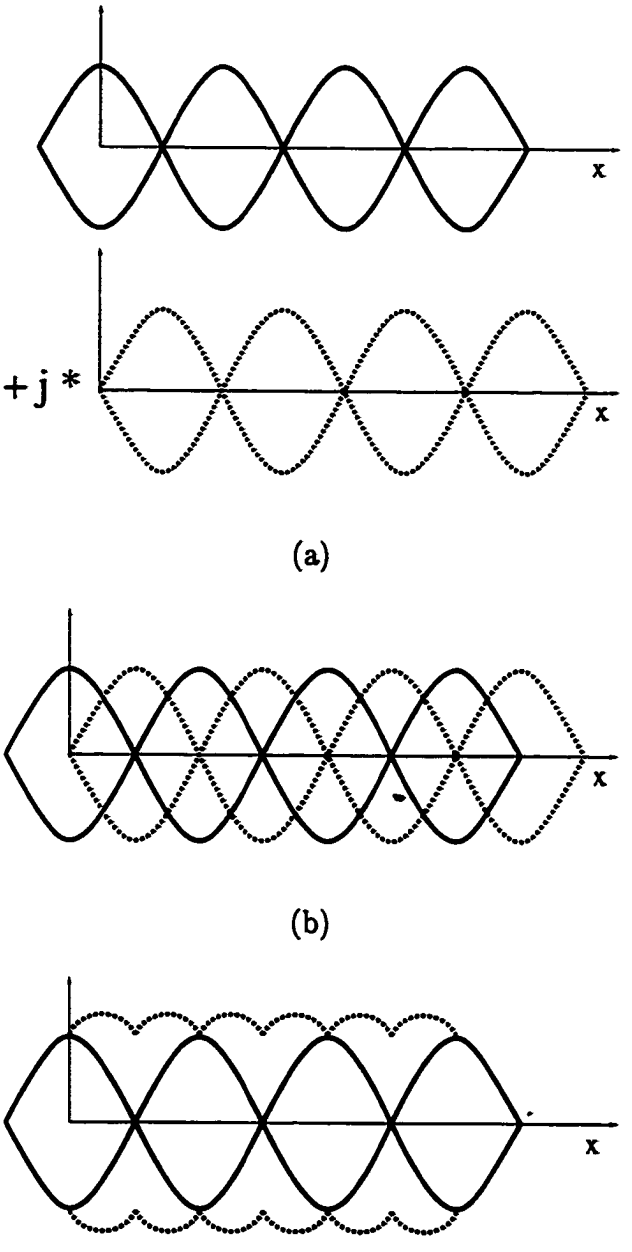

Figure 3.1: Array layout for linear array. (a) The cosine (solid line) and sine (dashed line) phased elements. (b) Cosine and sine phased elements must share space. (c) In the linear array the sharing is calculated using cosine and (sine+cosine) functions.

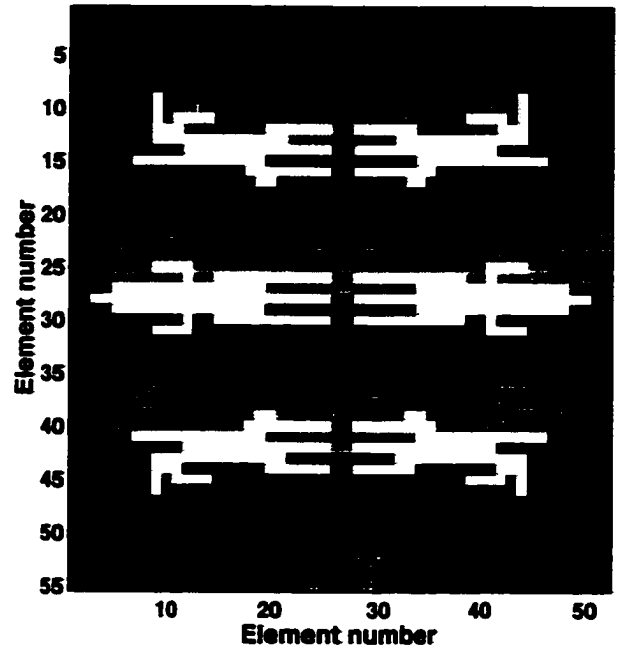

Figure 3.2: Array layout for 2D array based on implementation of linear array. Four grayscale levels represent the four phases for elements: white, cosine; black, negative cosine; light gray, sine; dark gray, negative sine.

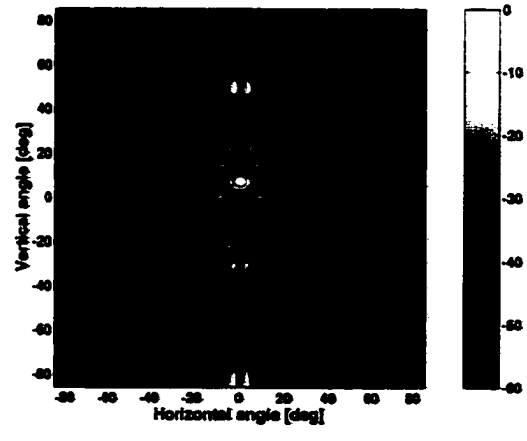

Figure 3.3: Field pattern for 2D array based on implementation of linear array.

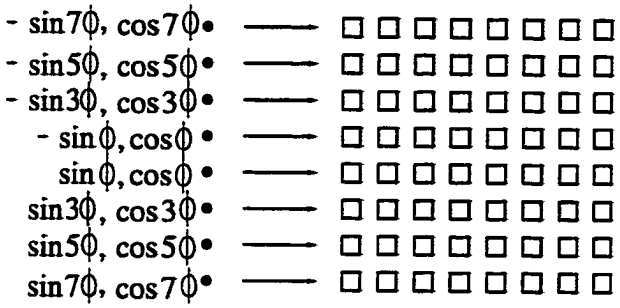

Figure 3.4: Representation of the conversion from amplitude-weights, to the design of the two-dimensional amplitude-steered array. To the left of the arrows, we show the point sources/receivers of the linear array, with the two sets of weights. To the right of the arrows, we show the row of the array, corresponding to the point element.

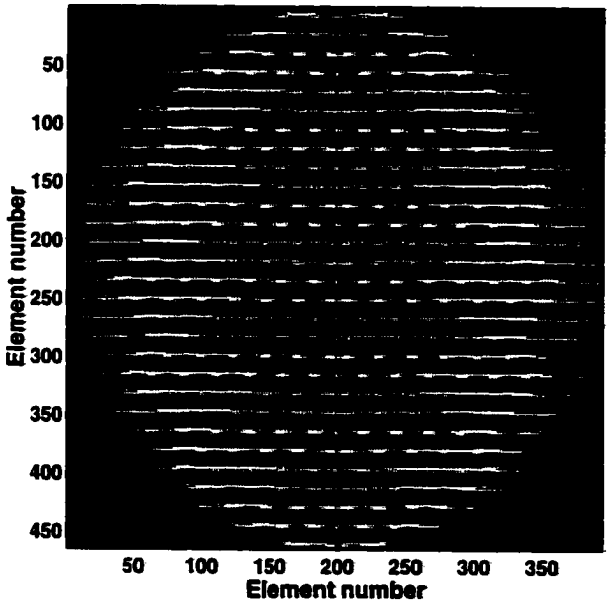

Figure 3.5: Array layout for 2D array with alternating element phases. Four grayscale levels represent the four phases for elements: white, cosine; black, negative cosine; light gray, sine; dark gray, negative sine.

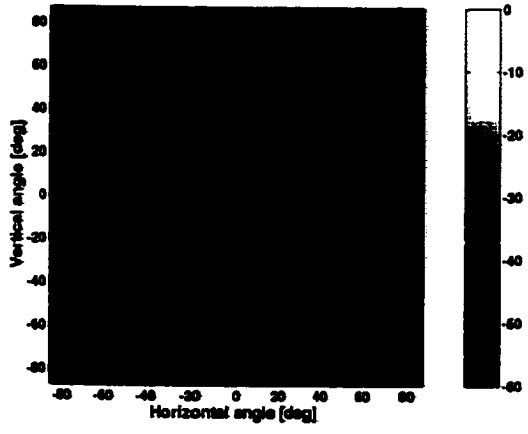

Figure 3.6: Field pattern for array with alternating element phases.

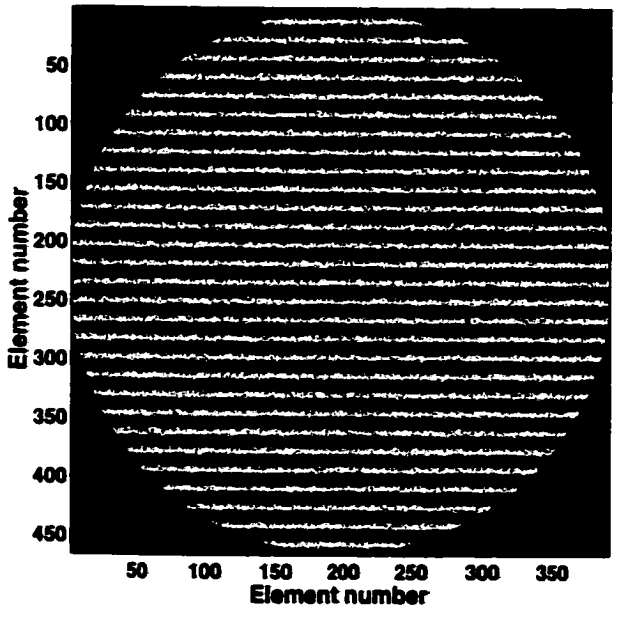

Figure 3.7: Array layout for 2D array with random placement of the four element phases. Four grayscale levels represent the four phases for elements: white, cosine; black, negative cosine; light gray, sine; dark gray, negative sine.

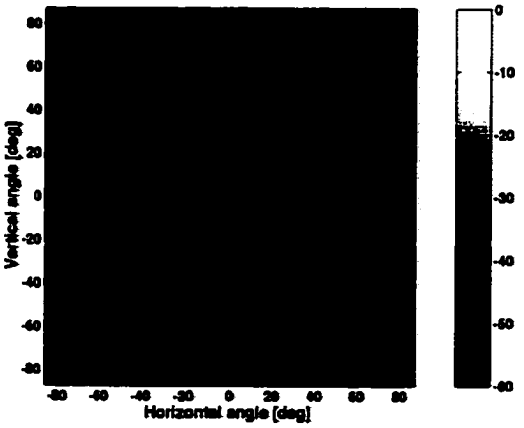

Figure 3.8: Field pattern for array with random placement of elements.

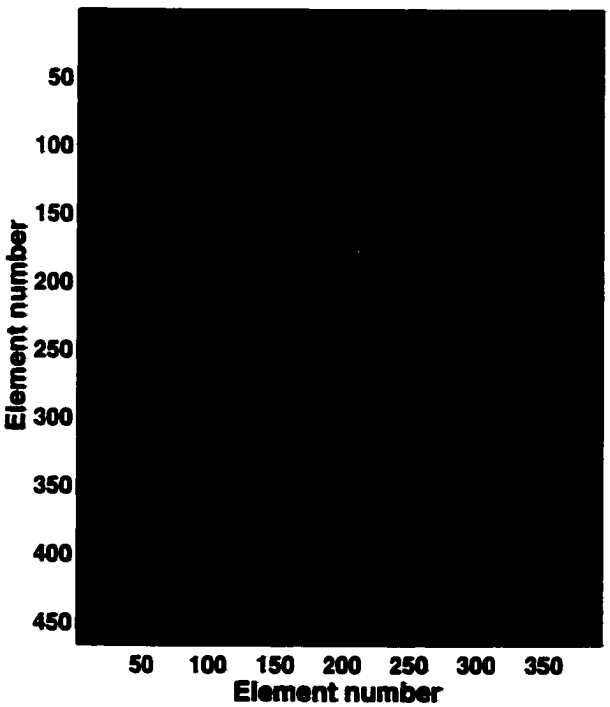

Figure 3.9: Array layout for the very sparse random design. Most elements are nulled.

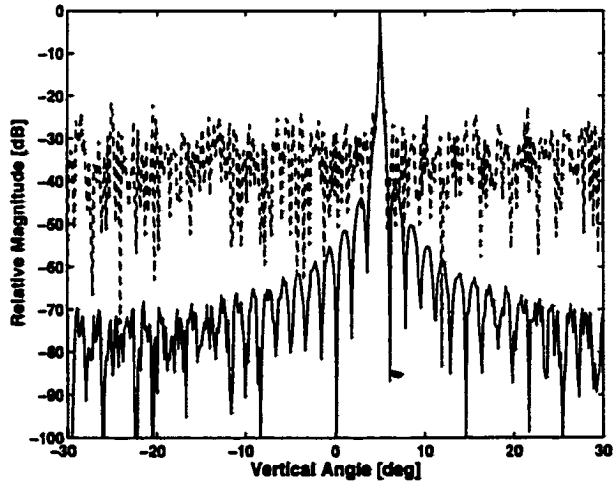

Figure 3.10: Comparison of the very sparse design (dashed line) to the optimal design (solid line). The main lobes are steered to the same direction and have the same beamwidth. However, the mean sidelobe level is much higher for the sparse design.

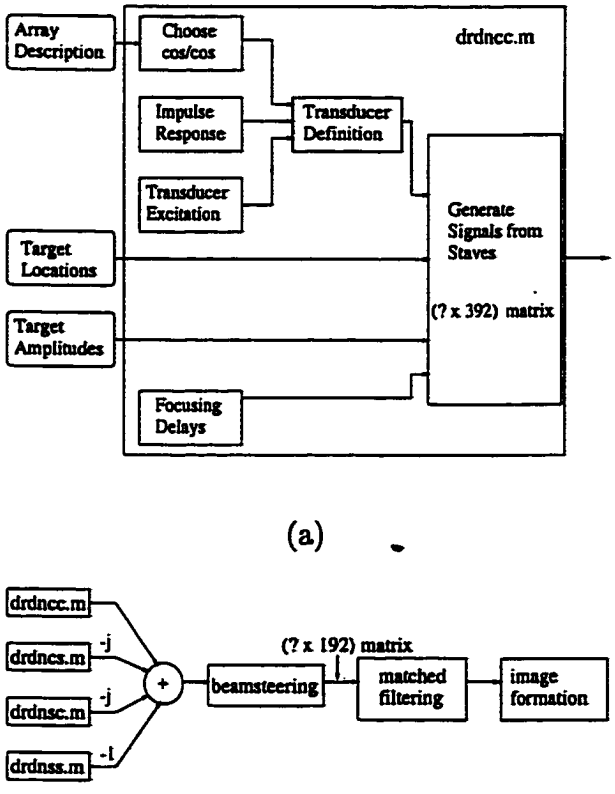

Figure 3.11: Block diagram of simulation. The question mark in the matrix sizes indicates the number of time samples received, which depends on the distance between the closest and farthest point targets.

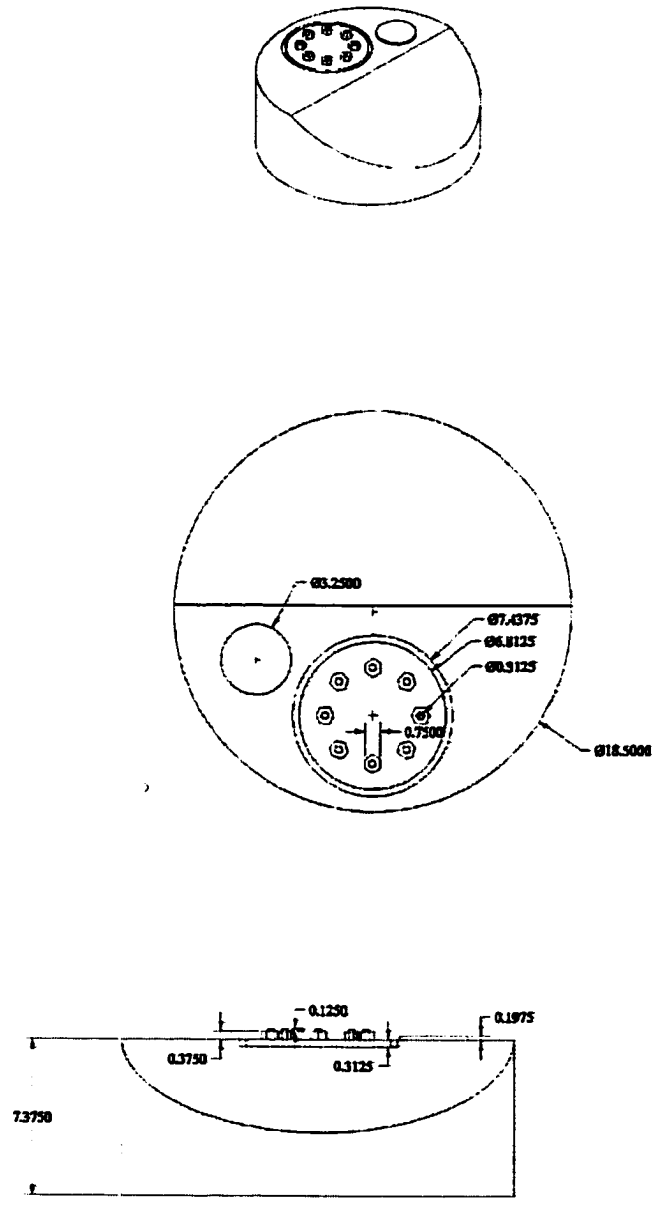

Figure 3.12: Diagram of test target.

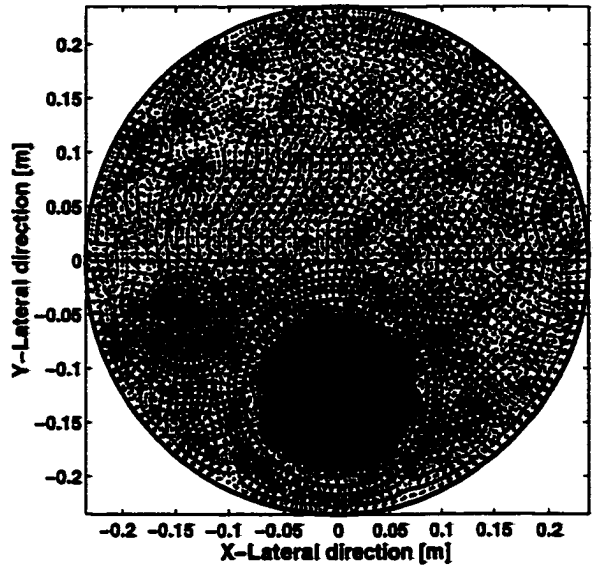

(a)

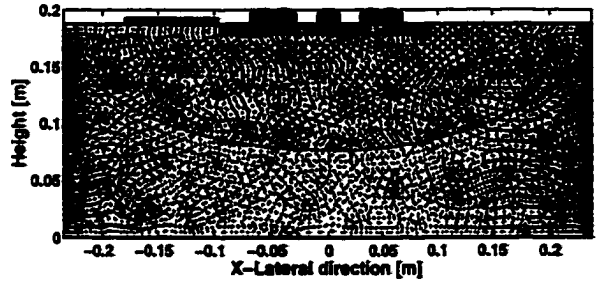

(b)

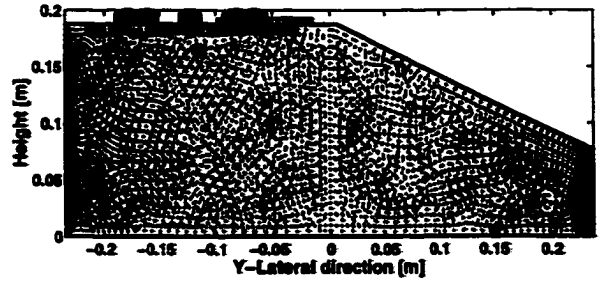

(c)

Figure 3.13: View of target as point sources: (a) top, (b) from horizontal, (c) from vertical.

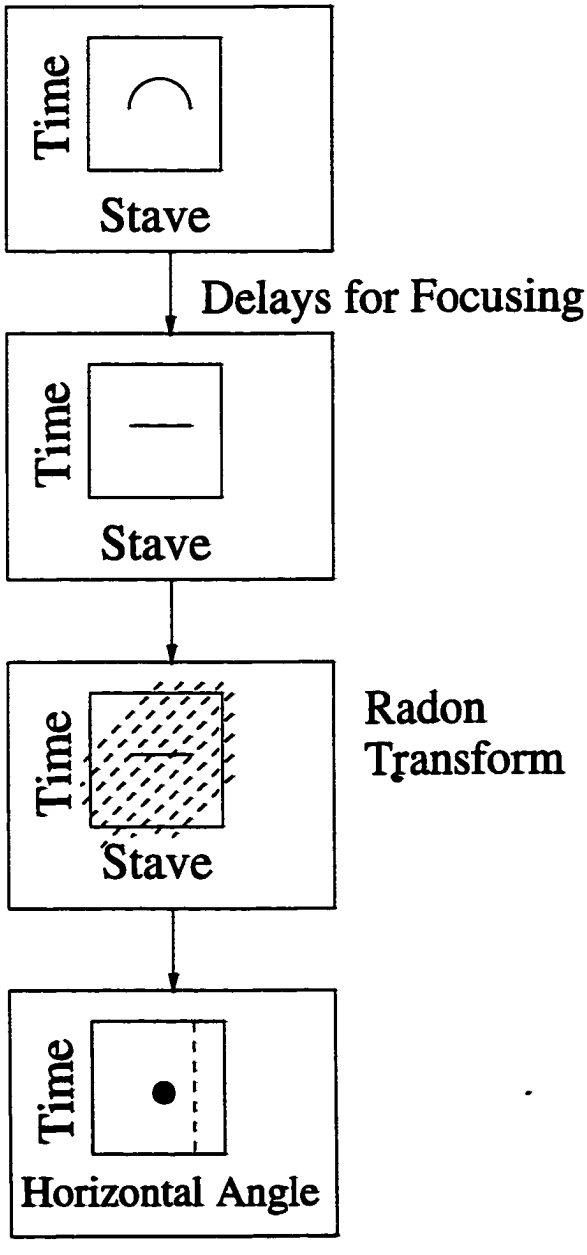

Figure 3.14: Block diagram of initial processing for image formation. Delays for focusing are applied within the Field II program. Beamsteering is accomplished using the Radon transform, which sums through the matrix at different angles, effectively delaying and summing signals from individual staves.

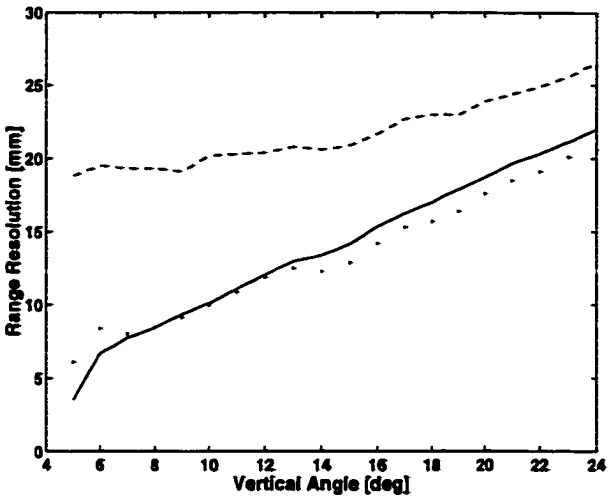

(a)

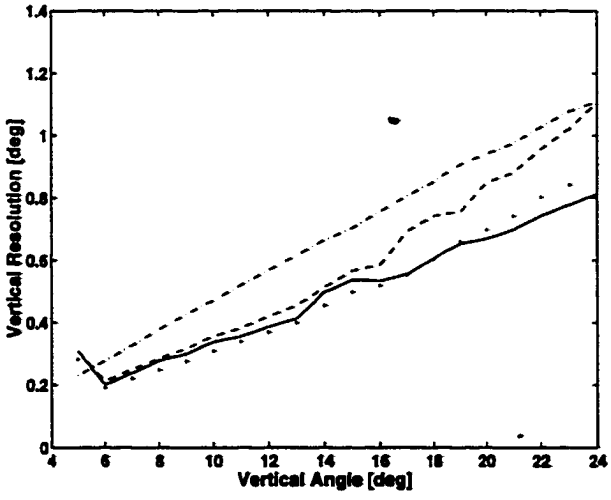

(b)

Figure 3.15: Comparsion of resolutions for no processing (solid line), spectrogram processing (dashed line), and SPWD processing (dotted line), for (a) range resolution and (b) vertical resolution. For comparison, the dash-dotted line in (b) shows the horizontal resolution measured with no processing.

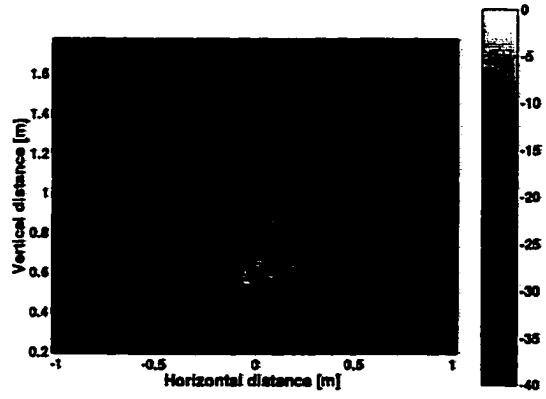

(a)

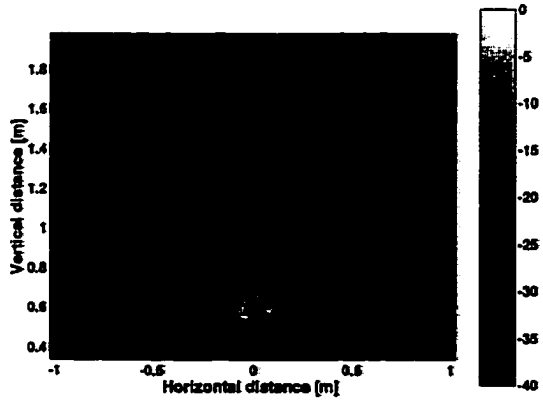

(b)

Figure 3.16: Sample images: maximum for each direction with threshold using (a) spectrogram, (b) SPWD. The target is at 4 m, although that information is not revealed by the image.

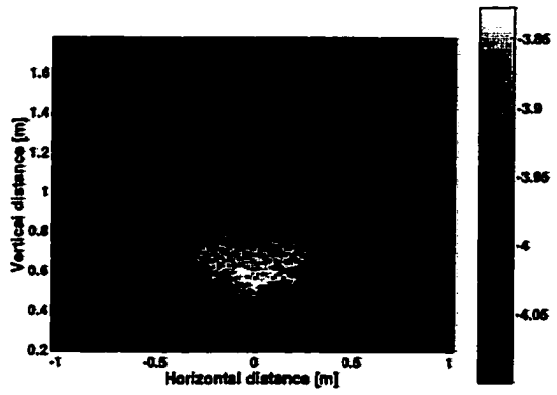

(a)

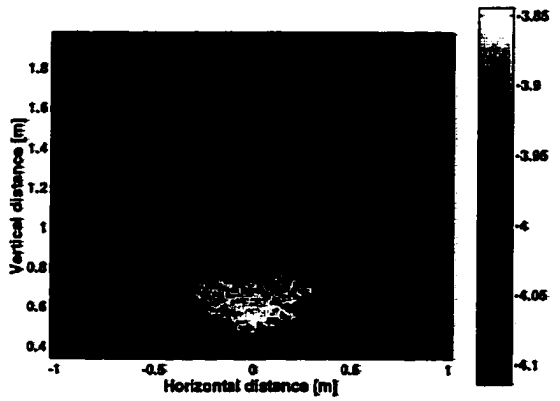

(b)

Figure 3.17: Sample images: range of maximum for each direction with threshold using (a) spectrogram, (b) SPWD.

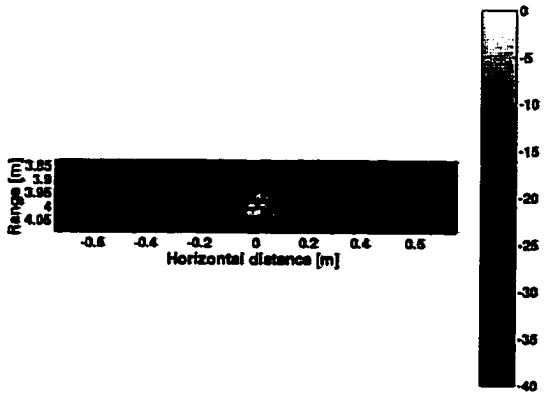

(a)

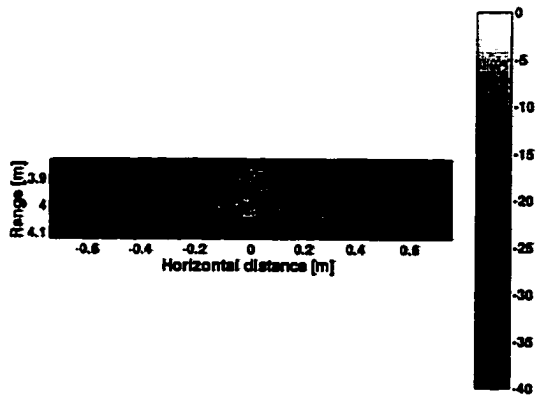

(b)

Figure 3.18: Sample images: a slice at $\theta_v = 6.29°$ using (a) spectrogram, (b) SPWD.

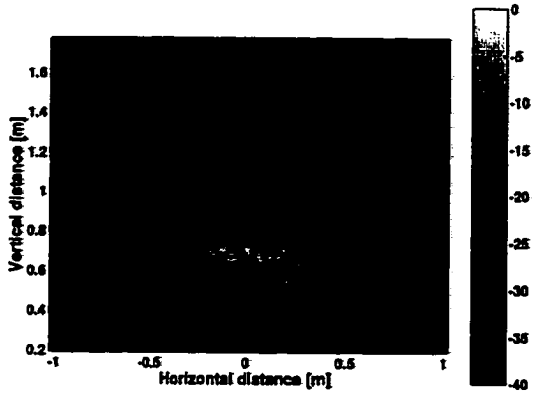

(a)

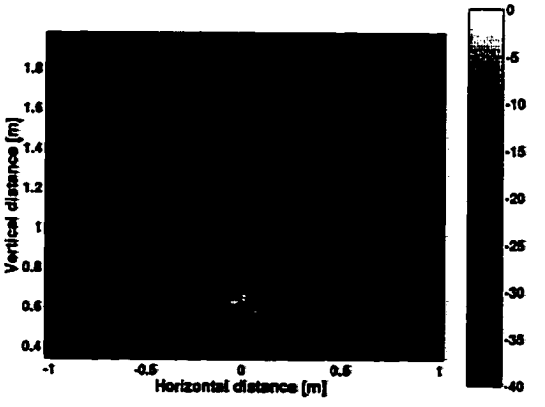

(b)

Figure 3.19: Sample images: a slice at a range of 3.86 m using (a) spectrogram, (b) SPWD.

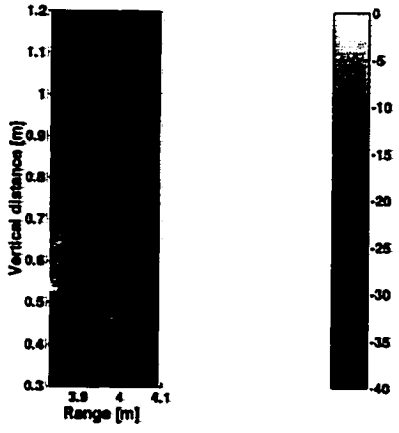

(a)

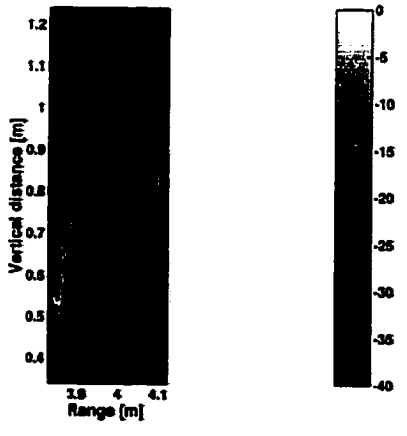

(b)

Figure 3.20: Sample images: a slice at $\theta_h = 0°$ using (a) spectrogram, (b) SPWD.

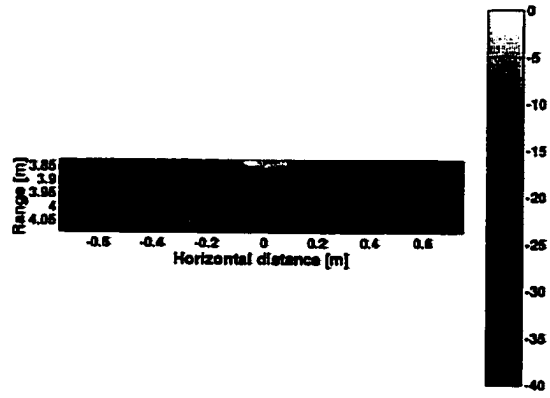

(a)

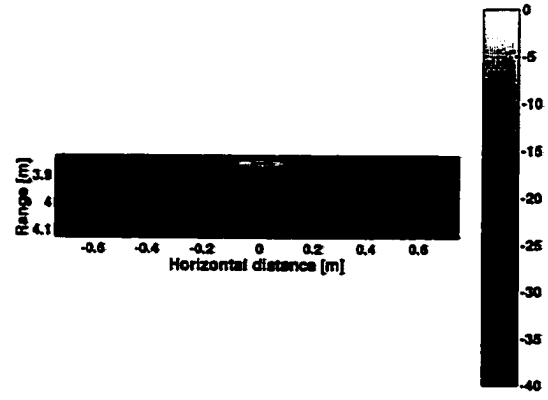

(b)

Figure 3.21: Sample images: projection images with integration through the vertical direction using (a) spectrogram, (b) SPWD.

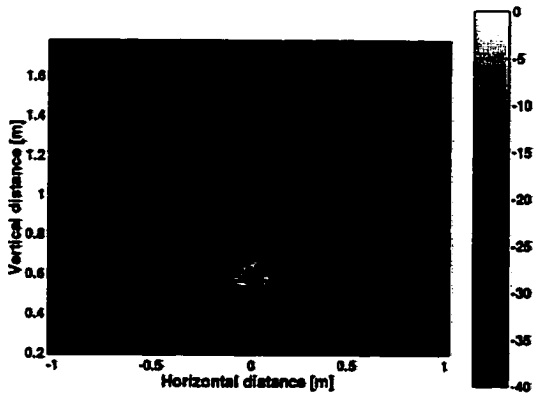

(a)

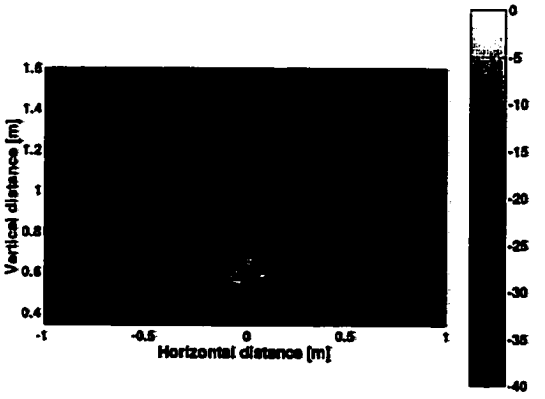

(b)

Figure 3.22: Sample images: projection images with integration through the range using (a) spectrogram, (b) SPWD.

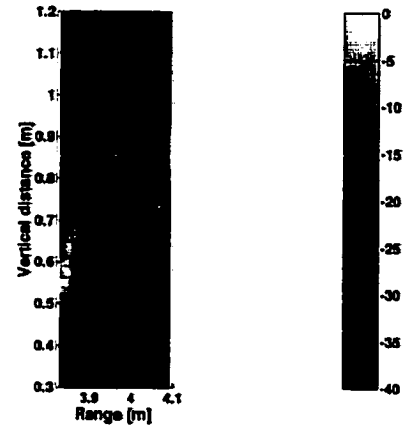

(a)

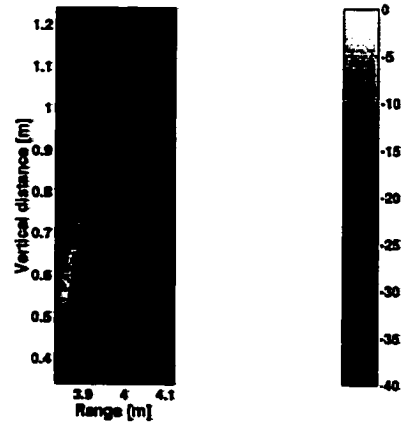

(b)

Figure 3.23: Sample images: projection images with integration through the horizontal direction using (a) spectrogram, (b) SPWD.

CHAPTER 4

EXPERIMENTAL RESULTS

In Chapters 2 and 3, we discuss the operation of the amplitude-steered array using simulated data. In this chapter, we present experimental results with a linear amplitude-steered array, to show that the simulations accurately describe imaging with the array. Although we use a linear amplitude-steered array, we would like to collect a volume of data, so that we may examine our technique of displaying the data with projection images. Three-dimensional data are collected by rotating the array in the direction perpendicular to the frequency separation.

This chapter begins with a description of the array used for data collection. Then the system used to collect data is described. The remainder of the chapter discusses data collection, simulation, and resulting images for four targets: three pipes, a ladder, a cylinder, and a bottle-nosed shell.

4.1 Description of the Array

The array used to collect data has been described briefly in Chapter 3. It is a low frequency amplitude-steered array, with its layout based on the linear amplitude-steered array. Array layout is shown in Figure 3.2, page 59. The array aperture is approximately circular, with a diameter of 10 cm. The maximum array dimensions are 52 by 55 elements. Interelement spacing is 2.11 mm. The array has a geometric focus at 0.61 m formed by curving the crystal slightly; however, the focus does not have much effect as it is very close to the near field/far field transition even at the highest frequencies used. We do not store signals from individual staves, so the array operates as a linear amplitude-steered array, rather than a full two-dimensional amplitude-steered array.

Frequency separation occurs in the vertical direction. The array is oriented such that lower frequencies are steered farther downward than higher frequencies. The array is designed to steer to 30° at 100 kHz. The peak frequency response of the array is at 220 kHz. The transmitted signal uses a frequency range from 80 to 304 kHz, which gives an angular coverage in the vertical direction from 9.5° to 38.7°.

4.2 Data Collection System

The data were collected in an anechoic tank at the Applied Research Laboratory (ARL) at the Pennsylvania State University. The tank measured 5.49 m deep by 5.33 m long by 7.92 m wide and was filled with stale water. The array was held by a custom-built positioning system (Scientific-Atlanta, Inc., Atlanta, GA) with 0.318 cm ($\frac{1}{8}$ in) depth resolution and $\pm 0.02°$ rotational resolution around a vertical axis. Data were collected in 1° rotational steps.

A diagram of the system used to collect pulse-echo data is shown in Figure 4.1. An HP 3314 function generator was used to manually trigger data collection. The transmit signal was generated by an HP 89410A vector signal analyzer. The transmit signal was split so that one signal path proceeded through a 90° phase shift. Each signal path then went through a power amplifier (Model L6, Instruments, Inc., San Diego, CA). The output from each amplifier was fed into a current voltage sensor (Model VIT-13, Instruments, Inc., San Diego, CA), used to monitor the current and voltage into the array electronics. The outputs from both sensors were input into the custom built phased array electronics box (ARL), which excited the amplitude-steered array.

The output from one current voltage sensor was also fed into an HP 59307A VHF switch so that the transmit voltage could be recorded by a second HP 89410A vector signal analyzer. The received signal from the amplitude-steered array was returned back through the phased array electronics, through a Krohn-Hite 3103A filter (passband 500 Hz to 1 MHz), to the VHF switch, and finally to channel 2 of the second vector signal analyzer. The vector signal analyzer digitized both transmit

and receive signals at a sampling rate of 1.024 MHz. Signals were stored on disk in HP format and later converted to Matlab format using software provided by HP.

The transmit signal generated by the first vector signal analyzer is a linear FM chirp, 0.5 ms in length. The start frequency is 304 kHz and the stop frequency is 80 kHz. A sample transmit signal is shown in Figure 4.2. The lower frequencies are given greater initial amplitude in an attempt to compensate for the frequency response of the transducer.

4.3 Experimental Results

Pulse-echo data were collected for several targets using the system described above. The targets were a set of pipes, a ladder, a cylindrical shell, and a bottle-nosed shell, which will be described in more detail in the following sections.

To describe target locations, we give two sets of coordinates, which are pictured in Figure 4.3. The first set of coordinates is in (x, y, z) form, where x is the horizontal position parallel to the face of the array, y is the depth, and z is the horizontal position perpendicular to the face of the array. Positive y is down, and positive z is away from the array in the broadside direction. Positive x follows from the right-hand rule. This convention is in agreement with that used by the Field II program. The second set of coordinates is in (r, θ_v, θ_h) form, where r is the range from the center of the array, θ_v is the vertical angle relative to horizontal with the origin at the center of the array, and θ_h is the horizontal angle relative to the broadside direction, also with the origin at the center of the array. Both sets of coordinates are given because the images of the targets are given using both coordinates.

Data processing has been described in Chapter 3. In this case, because the array was rotated and signals from individual staves were not recorded, no Radon transform was required. The received signals from each horizontal steering direction were first time-gated to remove the initial bleed-through of the transmit. Then the signals were filtered with a matched-filter for pulse-compression.

The projection through the vertical direction was formed by calculating the signal envelope using the Hilbert transform. The projection through the range direction was

formed by taking the absolute value of the Fourier transform of each received signal. The projection through the horizontal direction was formed by summing the received signals from each horizontal steering direction and then calculating the spectrogram or SPWD of the resulting summed signal. The spectrogram uses a 0.02-ms Hanning window. The SPWD uses filters that are Gaussian in shape in both the time and frequency directions, again described by the expression $exp(-t^2/\alpha^2 - \omega^2/\beta^2)$. In this case, α is 4.9 μs and β is 8886 rad/s.

Simulations were performed using Field II, so that the results could be compared to experimental data. In the simulations, the frequency response of the transducer was assumed to be flat, and the excitation signal did not change amplitude with frequency. Signals from individual staves were not recorded, but rather summed together. The target positions were rotated to simulate the rotation of the array. Processing of the simulated data was the same as processing of the experimental data, with the exception of the initial time-gating, which was not necessary for the simulated data.

Comparisons between the simulations and experiments are made on a qualitative basis. Target positions were measured at the water surface and therefore are known only approximately. Gross differences between the images from simulated and experimental data are apparent visually. Numerical comparisons, for example using the energy of a difference image or a correlation technique, would require multiple time-consuming simulations as the targets are translated and rotated to provide a better match, and not much insight would be gained.

4.3.1 Three-pipe target

The first targets used were three steel pipe targets. The pipes are each 3.05 m (10 ft) long, with an outer diameter of 2.54 cm (1 in) and an inner diameter of 0.794 cm ($\frac{5}{16}$ in). The targets are arranged as the three corners of a square, where the side of the square has a length of 30.5 cm (1 ft). The target positions and orientations are shown in Figure 4.4. The pipe locations are given by the coordinates (0 m, -, 1.0 m), (0 m, -, 1.305 m), and (−0.305 m, -, 1.305 m). For the pipe targets, no y coordinate (depth) is specified because the targets extend through the entire depth coverage of

the array. In terms of (r, θ_v, θ_h) coordinates, the targets are at (1.0 m, -, 0°), (1.305 m, -, 0°), and (1.340 m, -, −13.15°). θ_v is the entire insonified depth of the array, 9.5° to 38°. Data were collected over a range of horizontal angles from −25° to 10°. In the simulation, the three pipe targets were defined by 60 003 points. Each pipe was represented as a single line of points.

Figure 4.5 shows the projection through the vertical direction. Part (a) gives the simulated results and part (b) gives the experimental results. In the simulated image, each pipe target appears as a very thin horizontal line. The horizontal lines extend across the whole image because the beamwidth of the lowest frequency, 80 kHz, is 20°, and the image shows only a 35° sector. The image formed with experimental data agrees in character with the image formed with simulated data. The separation in range between the pipes appears to be larger than 0.305 m. This difference in separation is probably due to the pipes hanging at an angle, rather than perfectly vertical. The distances between the pipes were measured at the top of the pipes, above the water level. If the pipe that is supposedly at $x = 0$ m and $z = 1.305$ m is hanging at a 3° angle, the farther pipe would appear to be 0.4 m from the closer pipe, rather than the 0.3 m expected separation. The image formed with experimental data also has a distinct bright spot at 0° in the horizontal direction and 1.0 m in range. This reflection is probably due to a particularly strong reflection from the closest pipe, perhaps due to the pipe orientation. There were no other targets in the water, and there should not have been any air trapped in the pipe.

Figure 4.6 shows the simulated and experimental results for the projection through the range direction. Again the images formed using simulated and experimental data are similar. In particular, both have a diagonal characteristic in the upper left part of the image. Both images are filled with reflections, resulting from the extent of the targets through the frequency range and the wide beamwidths, particularly at low frequencies. However, the image formed using experimental data has the brighter spot at 0° horizontally and 15° vertically, as discussed above.

Figure 4.7 shows the simulated and experimental results for the projection through the horizontal angle where the time-frequency distribution is the spectrogram. To

form the image, signals from $-10°$ to $10°$ were included in the sum to form the projection through the horizontal angle, so that signals were summed symmetrically about $\theta_h = 0$ even though the data were not collected symmetrically around the $\theta_h = 0°$ angle. The images are similar in character, showing two vertical lines, one at 1.0 m and one farther in range. The difference in range separation has been discussed previously. The two vertical lines represent the three targets, although in the projection, it is impossible to separate the two targets at the same range. In the image from simulated data, the brightest reflections occur at lower vertical distances. In the image from experimental data, the brightest reflection occurs at the top of the closer target. This location of the brightest reflection agrees with that of the other two projections for experimental data.

Figure 4.8 shows the simulated and experimental results for the projection through the horizontal angle using the SPWD processing. Images formed with the SPWD are much sharper than the images formed with the spectrogram and provide better range resolution.

4.3.2 Ladder target

The ladder target was a standard 6-ft wooden step ladder. The rungs were 30.5 cm (1 ft) apart. The ladder was placed in the water in the closed position so that it hung approximately vertically, 1.2 m away from the array. The target position and orientation are shown in Figure 4.9. Two rungs appear within the insonified depth of the array; however, a third rung is very close to the insonified region. The locations of these three rungs are given by the coordinates ($\pm$ 0.152 m, 0.406 m, 1.2 m), ($\pm$ 0.152 m, 0.711 m, 1.2 m), and ($\pm$ 0.152 m, 1.02 m, 1.2 m). In terms of angles, the coordinates are (1.27 m, 18.7°, $\pm$7.2°), (1.40 m, 30.7°, $\pm$7.2°), and (1.57 m, 40.2°, $\pm$7.2°). The positive and negative values in the x coordinate and θ_v represent a range which is the extent of a rung. Data were collected over a range of horizontal angles from $-30°$ to $30°$. To represent the targets for the simulations, 53 636 points were used. The sides of the ladder and each rung were represented as a line of point targets.

Figure 4.10 shows the projection images through the vertical angle using simulated and experimental data. The three rungs should be present at 1.27 m, 1.4 m, and 1.57 m. All three rungs are visible in the image from simulated data, at these ranges. In the image from experimental data, the third rung is not visible, probably due to the low response of the array at lower frequencies, and due to the position of the rung just outside of the field of interest. Also, at the closest/highest rung, reflections from the sides of the ladder appear.

Figure 4.11 shows the projection images through the range direction using simulated and experimental data. In these images, the targets are more clear than in the images of the three-pipe targets because in this case the rungs are horizontal rather than vertical. Because the rungs are horizontal, each reflects a smaller range of frequencies and therefore can be separated in this projection. Both the image from simulated data and the image from experimental data show two rungs. The upper rung appears smaller, indicating the smaller beamwidth at the higher frequency. In both cases, the lower rung appears wider. In the image from experimental data, the lower rung also appears less bright due to the lower frequency response of the transducer at the lower frequency.

Figure 4.12 shows the projection images through horizontal angle using simulated and experimental data. Both of these images show three rungs. The third (lowest) rung appears in this projection because summing across the horizontal angles has increased the signal level above the noise. However, only part of the lowest rung is visible. The highest rung appears to be closest in range to the transducer. The middle rung appears the brightest because of the summing operation.

Figure 4.13 shows the projection images through the horizontal angle using simulated and experimental data processed using the SPWD processing. Again, the SPWD images are sharper than the spectrogram images. The middle and bottom rungs are shown with better resolution in the SPWD images. The top rung appears to have some unexpected structure in the SPWD image, which is also present but blurred in the spectrogram image. There is excellent agreement between the simulated and experimental data for these four sets of images.

4.3.3 Cylinder target

The cylinder target was a section of an aluminum shell. It was 85.9 cm in length and 32.4 cm in diameter. The thickness of the aluminum was 0.95 cm ($\frac{3}{8}$ in). The shell was hollow, and once submerged, was water-filled. The target position and orientation are shown in Figure 4.14. The shell was suspended such that its length was parallel with the face of the array, and the axis of the cylinder was horizontal. The axis of the cylinder is given by the coordinates ($\pm$ 0.43 m, 0.30 m, 1.2 m). In terms of angles, the axis of the cylinder is given by the coordinates (1.23 m, 13.8°, $\pm$19.8°). Data were collected over a range of horizontal angles from $-40°$ to 40°.

There is less agreement between the simulated and experimental data for the cylinder target than for the pipes or ladder targets. The cylinder target is a smooth, continuous reflector, which must be represented by closely spaced point targets in Field II. Thus, a large number of points are required to define the target. In this case, 240 120 points were used to represent a cylinder of length 0.2 m, which is smaller than the actual length.

Figure 4.15 shows the projection images through vertical angle for simulated and experimental data. The simulated data shows three distinct reflections. The first is the reflection from the front of the cylinder. It occurs at the closest range, 1.05 m. The second reflection, which extends from 1.1 m to 1.35 m in range, is from the bottom of the cylinder. The reflection from the bottom is possible in the simulations because the point density defining the target is small and Field II considers each target separately. The reflection appears broad because of the wide beamwidth at the lower frequency. The third reflection, at 1.4 m in range, is from the back of the cylinder. The back reflection also appears because the target is represented as a collection of point targets, and the point targets are not close enough together. In the image from experimental data, there is a reflection from the front/bottom of the cylinder, but no reflection from the back. Very little sound is incident on the back of the cylinder as most of the energy is reflected at the front of the cylinder. The image also shows reflections from the ends of the cylinder.

Figure 4.16 shows the projection images through the range direction for simulated and experimental data. From this set of projections, it appears that the cylinder is actually lower in the water than simulated. In the image formed from simulated data, we see that all parts of the cylinder that are insonified reflect energy. In the image from experimental data, we see that the largest reflection comes from the lower front of the cylinder. That refection is not centered at 0° horizontally because the cylinder axis was slightly tipped so that it was not exactly parallel to the face of the array. There are also reflections from the ends of the cylinder.

Figure 4.17 shows the projection images through the horizontal angle for simulated and experimental data. These projections show the major difference between the simulations and the experimental data. In the projection through the horizontal angle, for the simulated data, we see the cross-section of the cylinder. For the experimental data, we see only the brightest reflection towards the bottom of the cylinder.

Figure 4.18 shows the projection images through the horizontal angle for simulated and experimental data using SPWD processing. In the simulated image, the cylinder is much sharper than for the spectrogram processing; however, there is a large amount of interference within the cylinder. The SPWD image may benefit from increased smoothing even though some resolution would be lost.

4.3.4 Shell target

A picture of the bottle-nosed shell is shown in Figure 4.19. The shell had the shape of a baby's bottle. The smaller cylinder was 15.2 cm in diameter and 15.2 cm in height. The top and bottom cylinders were connected at a 45° angle. The bottom cylinder was 38.1 cm in diameter and 45.7 cm in height. The total height of the shell was 72.4 cm. The shell was made of aluminum and it was completely enclosed so that it was not a water-filled target. Instead, it was filled with air and metallic components.

The target position and orientation are shown in Figure 4.20. The shell was suspended such that the smaller cylinder was closer to the array, and the axis of the cylinder was perpendicular to the face of the array. The front of the shell was 1.17 m

from the array. The coordinates of the shell axis were given by (0 m, 0.432 m, 1.17 m to 1.78 m). In terms of angles, the coordinates of the shell axis were given by (1.25 m, 20.3° to 13.6°, 0°). Data were collected over a range of horizontal angles from −30° to 30°.

As is the case with the cylinder target, the bottle-nosed shell target is a smooth, continuous target that requires many points to define in simulation. In this case, the simulation used 457 560 points.

Figure 4.21 shows the projection images through vertical direction for simulated and experimental data. Both simulated and experimental data show a large reflection from the front of the shell. The image from experimental data also shows a reflection later in the range, most likely due to a reflection from the second cylinder of the shell. The orientation of the shell axis is not exactly perpendicular to the array, as it was modelled. Instead, the nose of the shell is tipped up and slightly toward negative x values. Some portion of the second cylinder provides a reflection back to the array.

Figure 4.22 shows the projection images through the range direction for simulated and experimental data. Both images show the large reflection from the front of the shell. The experimental data also show a smaller reflection from a larger vertical angle (between 20° and 35°). This reflection is probably a combination of reflections from the slanted surface between the two cylinders and from the second cylinder. These two reflections are more clear in the projection through the horizontal direction. These surfaces may not be visible to the array in the simulations due to differences in target orientation between simulation and experiment.

In Figure 4.23 the projections through the horizontal angle are shown. The simulated data show only one reflection. The experimental data show three reflections as discussed for the previous two projections. The first reflection, in range, corresponds to the front of the shell. The lower reflection corresponds to a lower surface of the target. And the latest reflection in range is probably due to the second cylinder of the target. It is difficult to discern the shape of the target from these images. It is believed that because of the smooth surfaces of the target, most of the incident energy is scattered away from the array.

In Figure 4.24 the projections through the horizontal angle are shown where we use the SPWD processing to form the image. In this case, the cross-terms of the SPWD detract from the ability to discern targets.

4.4 Conclusions

In this chapter, we compared experimentally collected data with simulated data to verify our simulations. The three-dimensional data sets collected here were not the same as those described in Chapter 3. In Chapter 3, we used two staves of a two-dimensional array to transmit, and we formed several receive beams. Here we rotated a linear array to get the third dimension in the data. It may be possible to use such a configuration for data collection in applications other than sonar, such as medical imaging. However, for imaging ranges up to 5 m, this configuration is not practical for real-time imaging.

The comparison between simulations and experiments showed that our simulations reasonably predict the response of the array. There was excellent agreement between simulations and experiments, especially for point-like targets such as the ladder. Targets with broad smooth surfaces, such as the cylinder, were not well represented as a collection of point targets; however, the representation may be improved by increasing the point density. The limitation in the simulations was primarily due to the processing time required to collect data for a target defined by a large number of points.

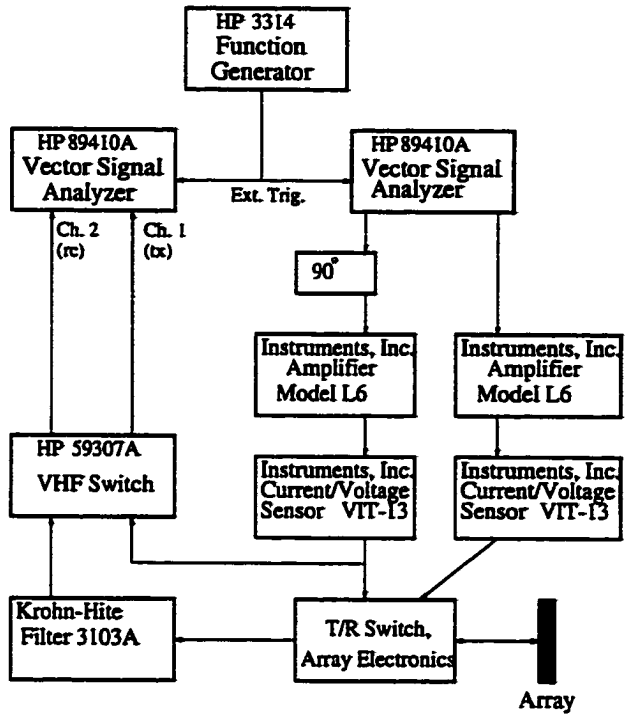

Figure 4.1: Diagram of data acquisition system.

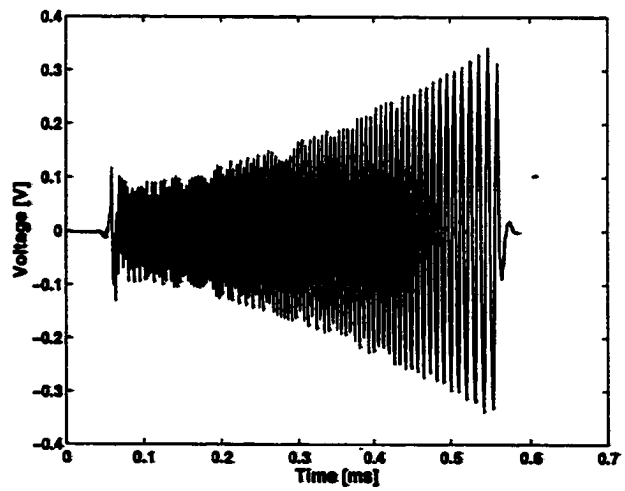

Figure 4.2: Linear FM chirp used as transmit signal.

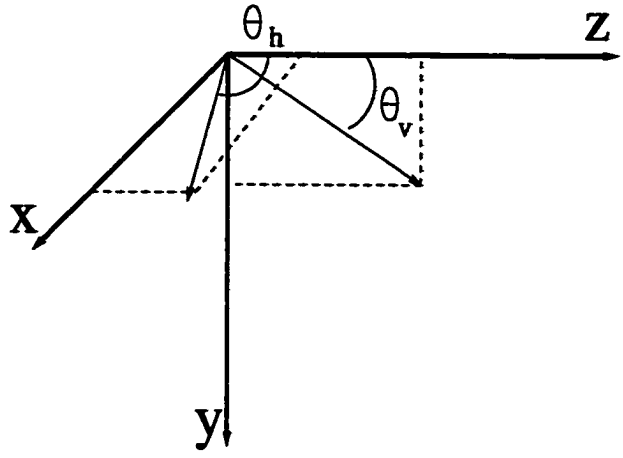

Figure 4.3: Illustration to show axes and angles used to define target positions.

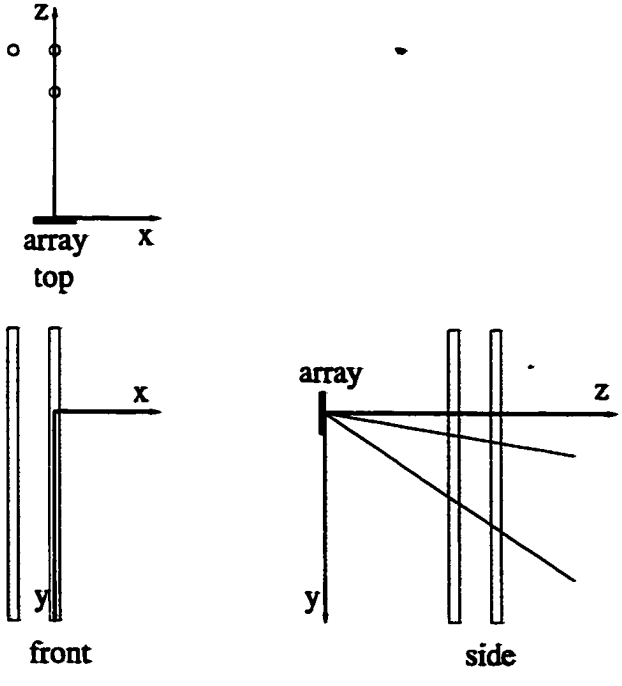

Figure 4.4: Top, front, and side views of the three-pipes target.

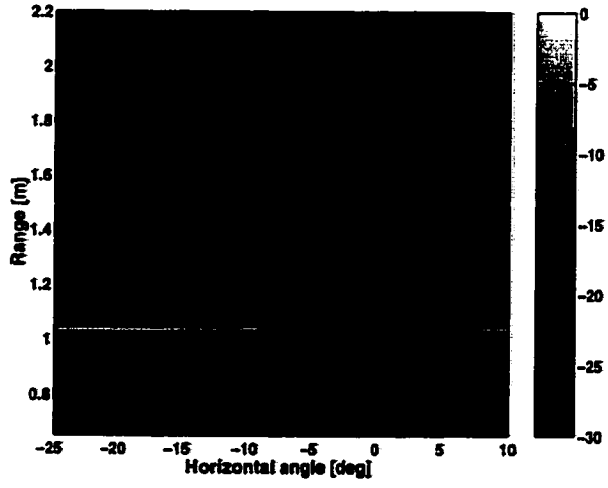

(a)

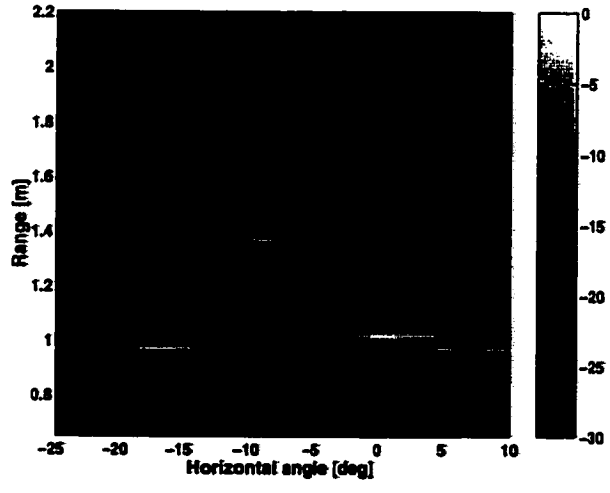

(b)

Figure 4.5: Images of the three-pipes target (top view). Range versus horizontal angle (a) simulated, (b) experimental.

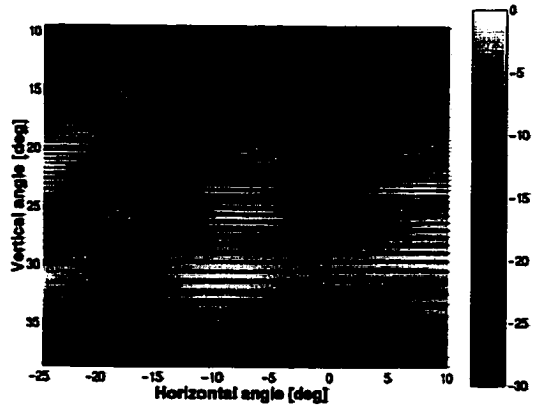

(a)

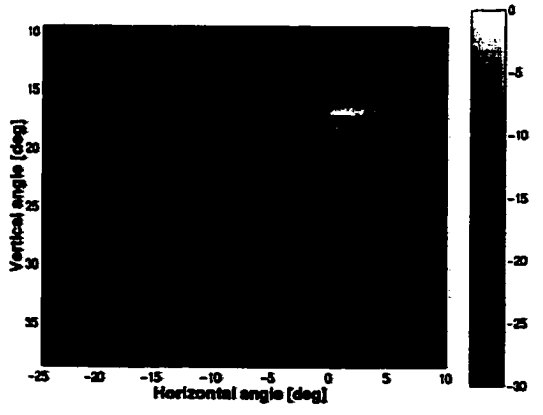

(b)

Figure 4.6: Images of the three-pipes target (front view). Vertical angle versus horizontal angle (a) simulated, (b) experimental.

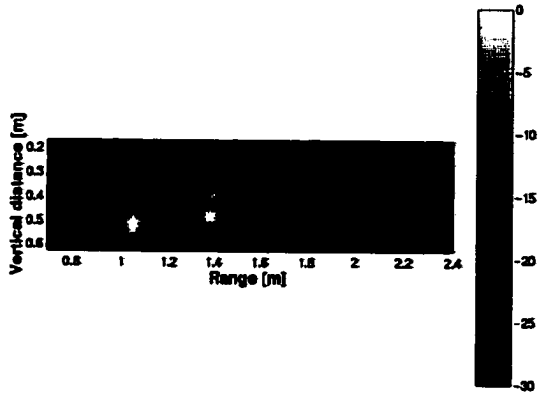

(a)

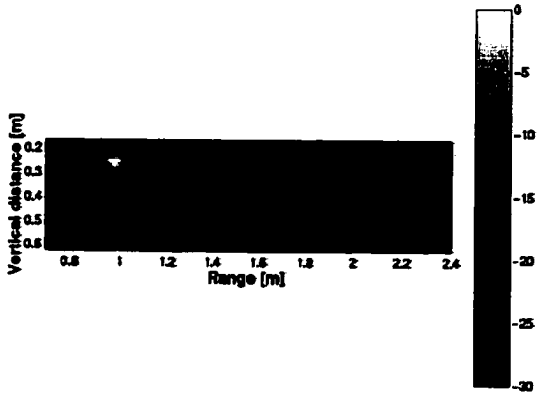

(b)

Figure 4.7: Images of the three-pipes target formed using the spectrogram (side view). Vertical angle versus range (a) simulated, (b) experimental.

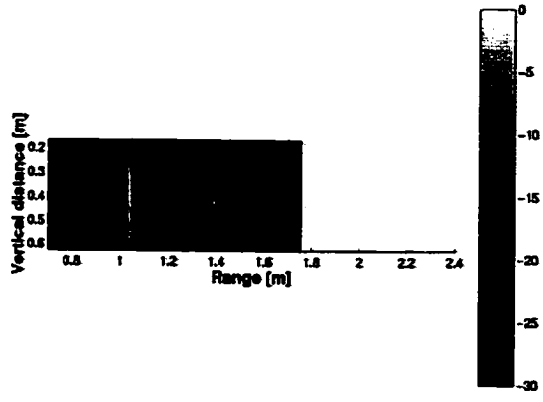

(a)

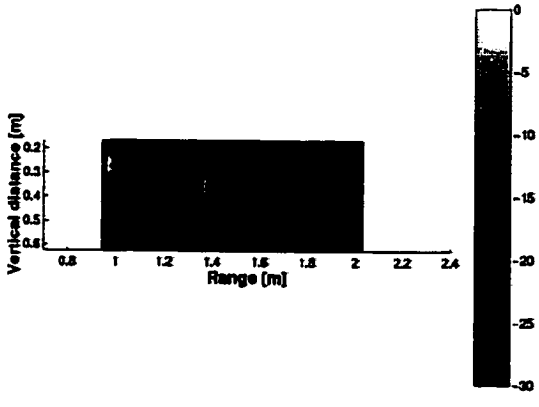

(b)

Figure 4.8: Images of the three-pipes target formed using SPWD (side view). Vertical angle versus range (a) simulated, (b) experimental.

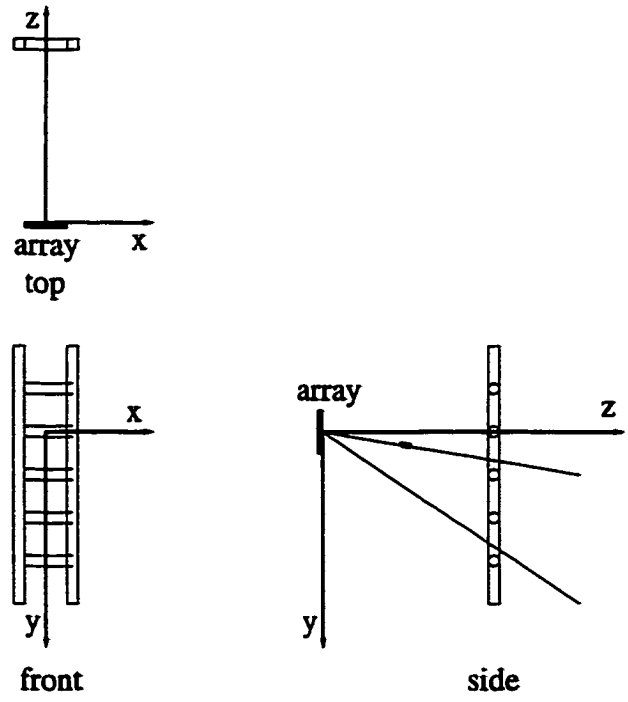

Figure 4.9: Top, front, and side views showing position and orientation of ladder target.

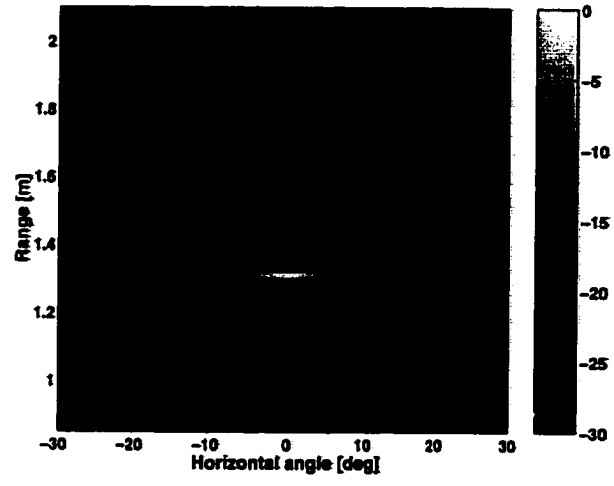

(a)

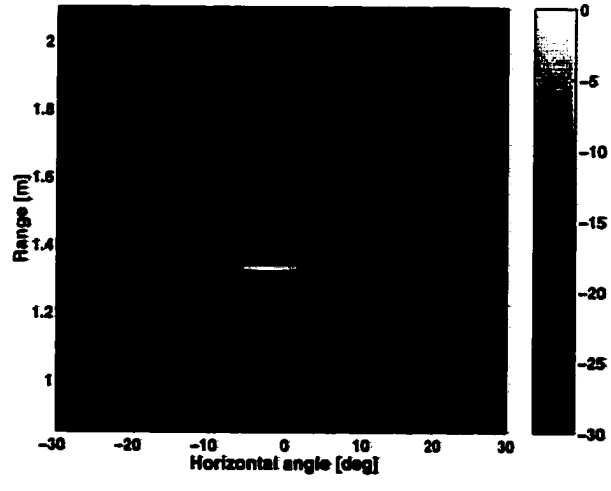

(b)

Figure 4.10: Images of the ladder target (top view). Range versus horizontal angle (a) simulated, (b) experimental.

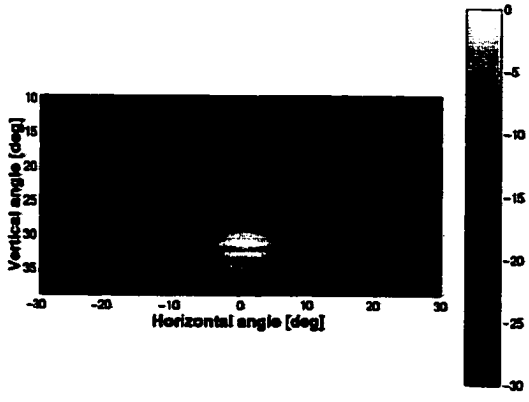

(a)

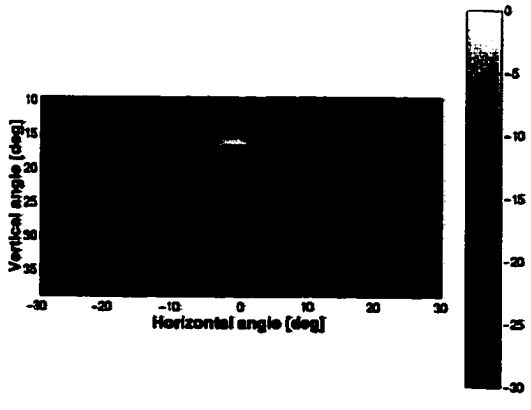

(b)

Figure 4.11: Images of the ladder target (front view). Vertical angle versus horizontal angle (a) simulated, (b) experimental.

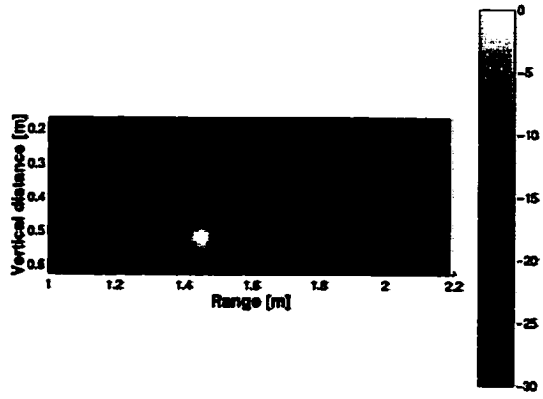

(a)

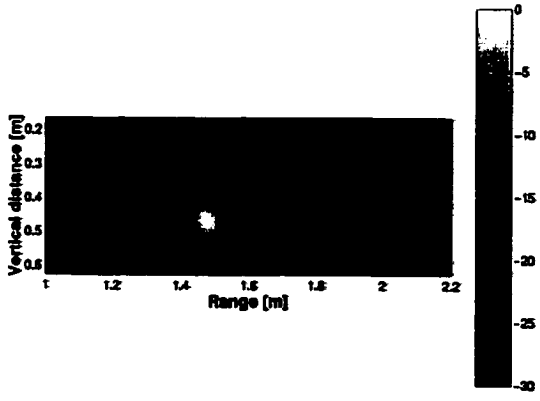

(b)

Figure 4.12: Images of the ladder target formed using the spectrogram (side view). Vertical angle versus range (a) simulated, (b) experimental.

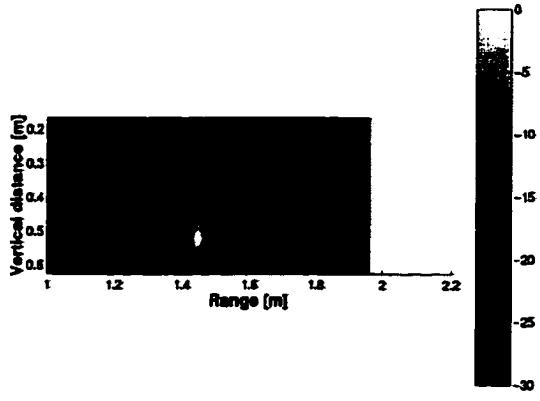

(a)

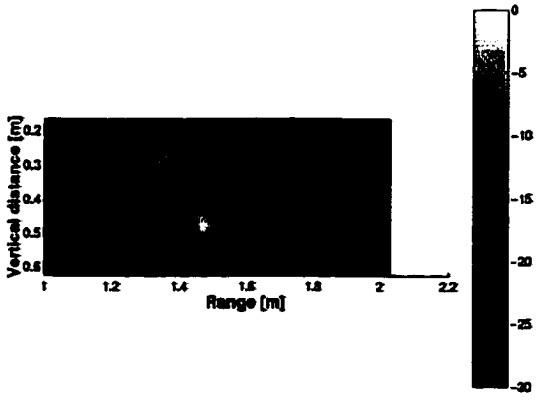

(b)

Figure 4.13: Images of the ladder target formed using SPWD (side view). Vertical angle versus range (a) simulated, (b) experimental.

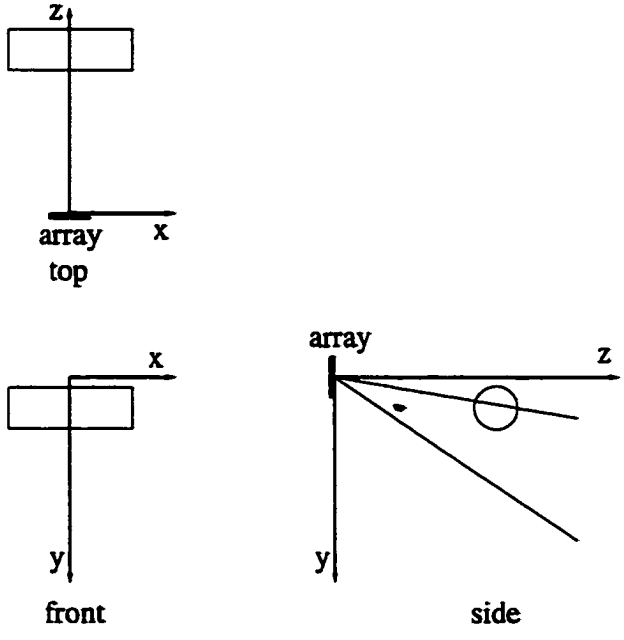

Figure 4.14: Top, front, and side views showing position and orientation of cylinder.

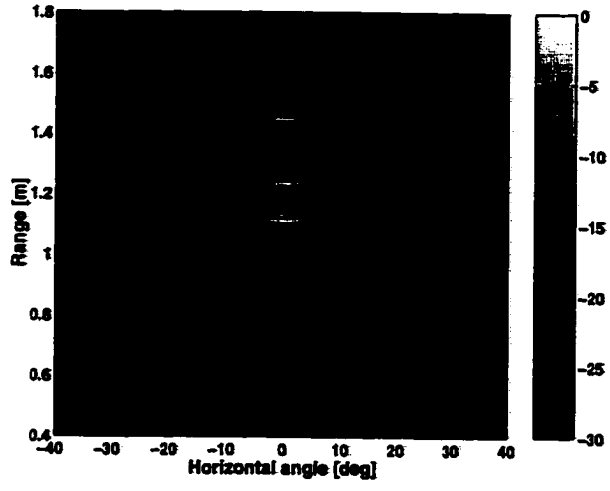

(a)

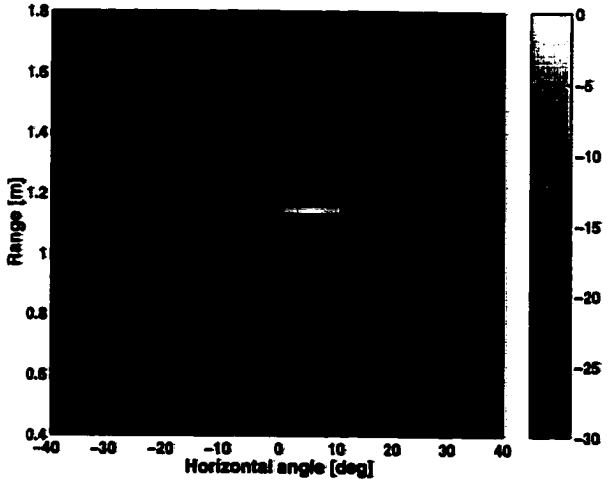

(b)

Figure 4.15: Images of the cylinder target (top view). Range versus horizontal angle (a) simulated, (b) experimental.

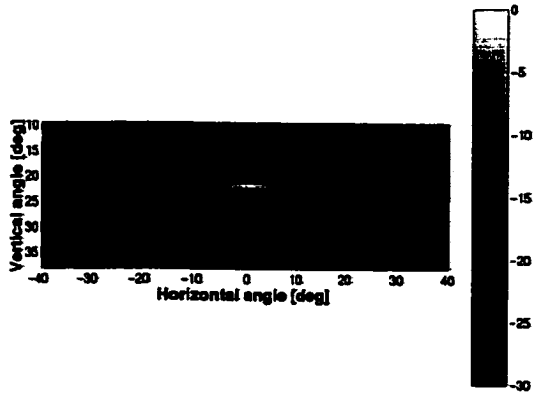

(a)

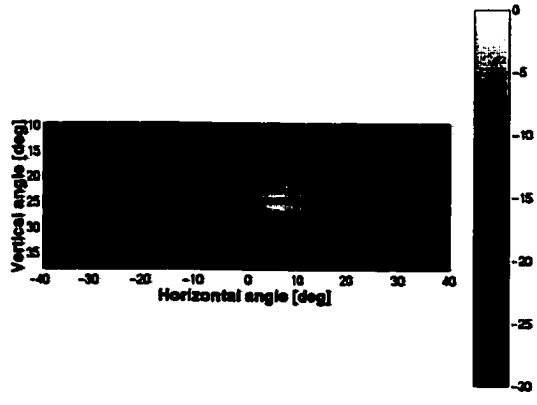

(b)

Figure 4.16: Images of the cylinder target (front view). Vertical angle versus horizontal angle (a) simulated, (b) experimental.

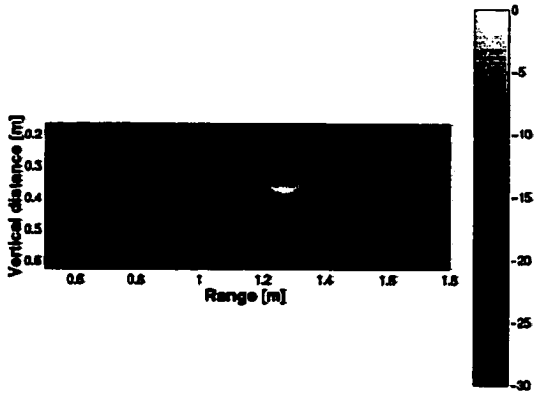

(a)

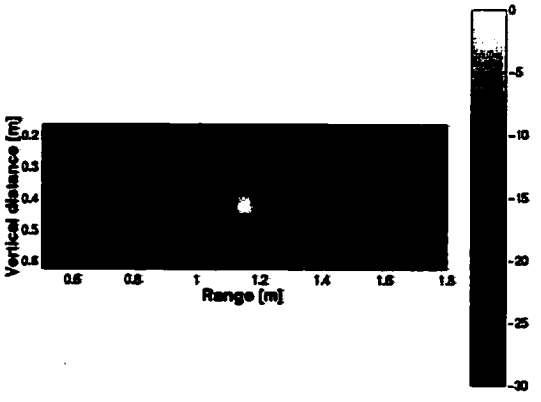

(b)

Figure 4.17: Images of the cylinder target formed using the spectrogram (side view). Vertical angle versus range (a) simulated, (b) experimental.

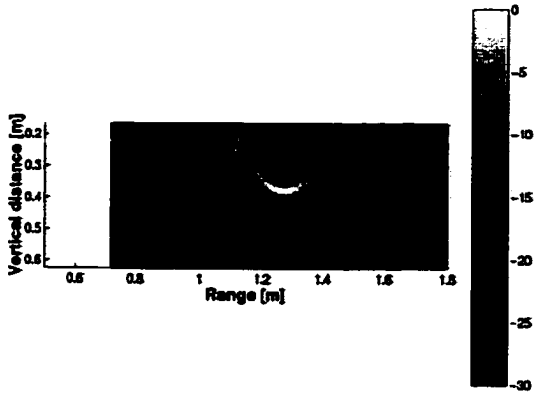

(a)

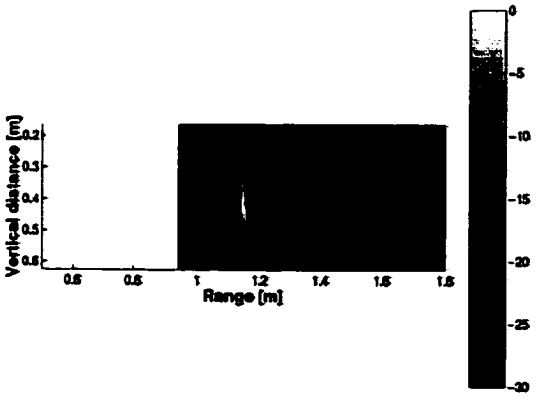

(b)

Figure 4.18: Images of the cylinder target formed using SPWD (side view). Vertical angle versus range (a) simulated, (b) experimental.

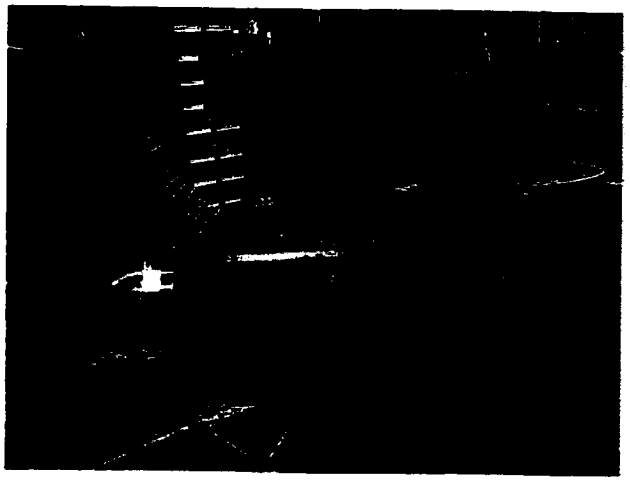

Figure 4.19: Picture of the bottle-nosed shell target.

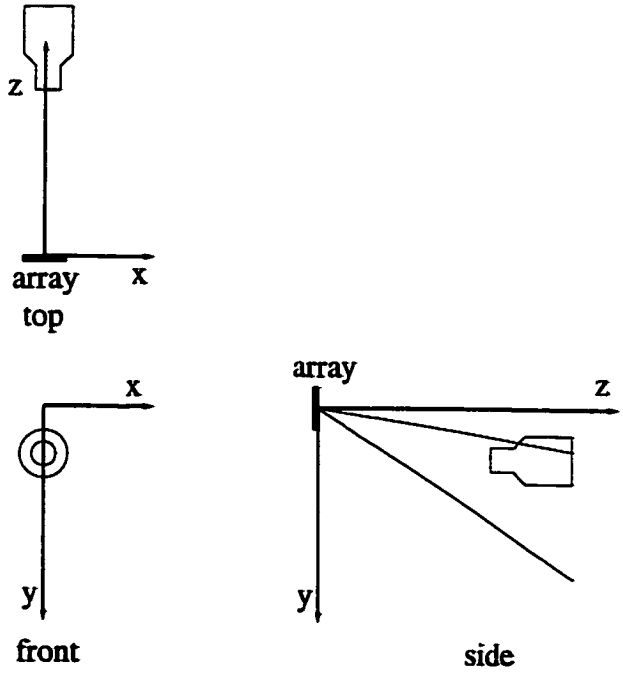

Figure 4.20: Top, front, and side views showing position and orientation of shell target.

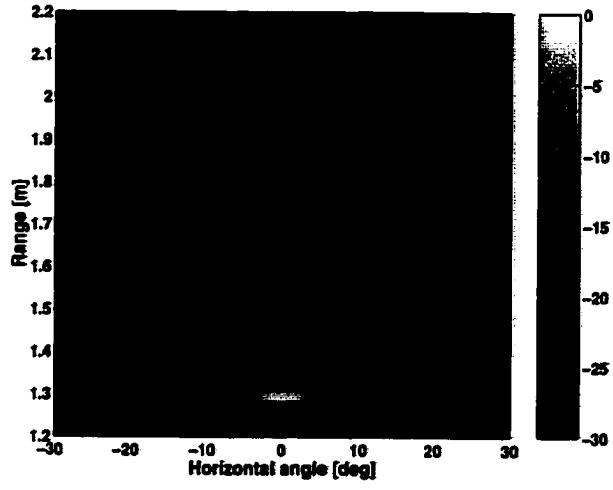

(a)

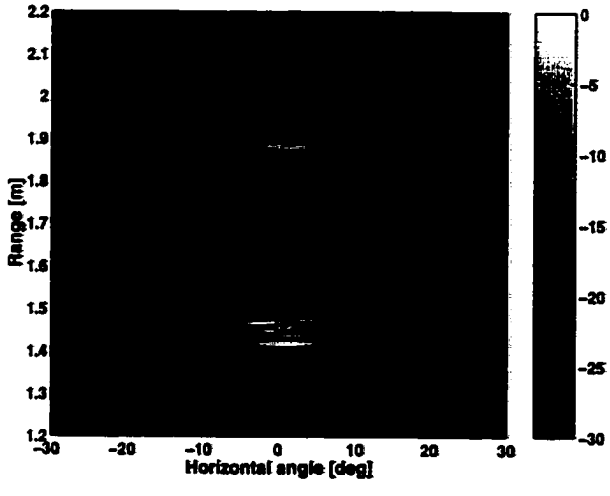

(b)

Figure 4.21: Images of the nose target (top view). Range versus horizontal angle (a) simulated, (b) experimental.

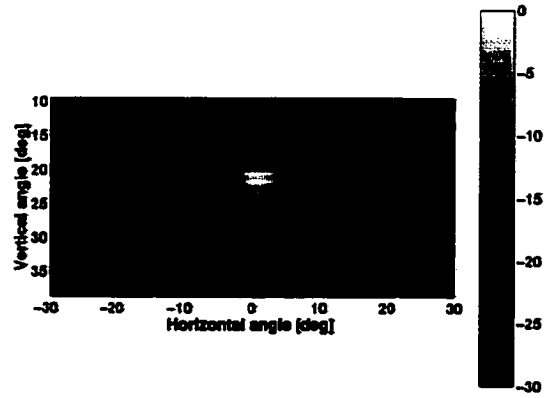

(a)

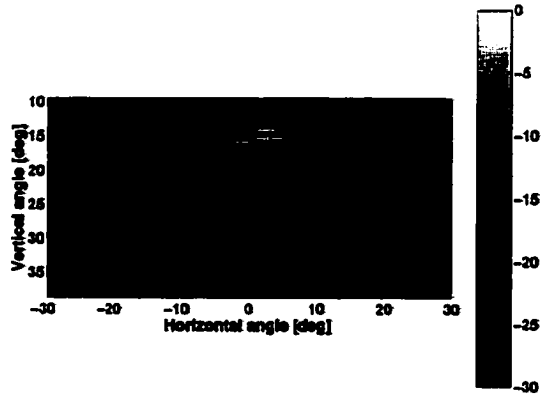

(b)

Figure 4.22: Images of the nose target (front view). Vertical angle versus horizontal angle (a) simulated, (b) experimental.

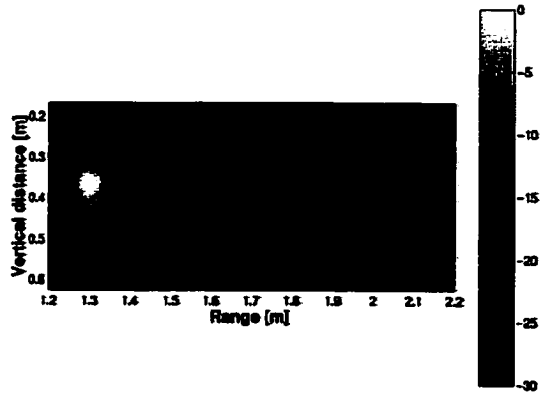

(a)

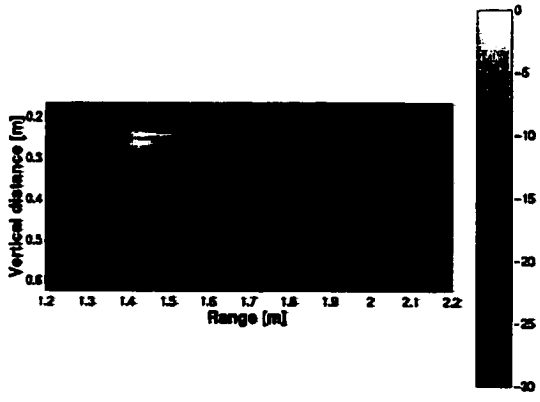

(b)

Figure 4.23: Images of the nose target formed using the spectrogram (side view). Vertical angle versus range (a) simulated, (b) experimental.

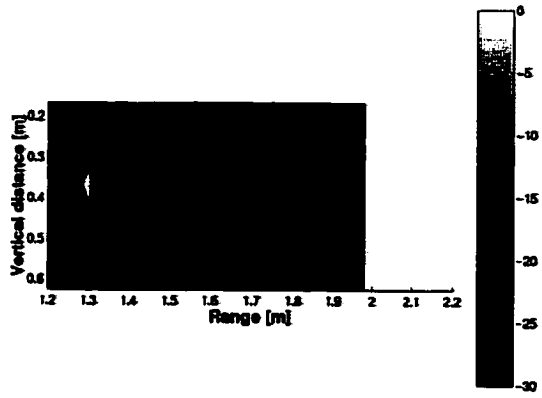

(a)

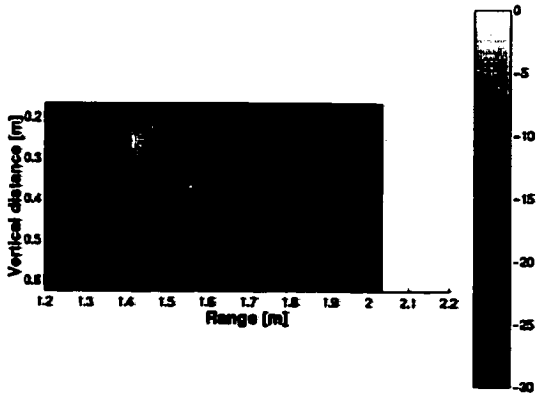

(b)

Figure 4.24: Images of the nose target formed using SPWD (side view). Vertical angle versus range (a) simulated, (b) experimental.

CHAPTER 5

NONLINEAR PROPAGATION

The amplitude-steered array can achieve fast image formation because it equates received frequency with a target's vertical position, eliminating the need to transmit multiple pulses steered in the vertical direction. However, sound propagation in water and other media is nonlinear, so that harmonics of the transmitted signal are generated as the wave propagates. In this chapter, we consider the effect these harmonics have on the operation of the array. The concern is that frequencies generated through nonlinear propagation will be considered additional targets close to the array broadside direction.

In this chapter, we first describe the expected array response to nonlinearly generated harmonics, and then we describe our simulations, which confirm this response. Within this section, we show two methods for simulation of nonlinear propagation from a piston source, choosing one for generating data and the other for confirming the results. We also list the simplifying assumptions we used to perform our simulations. Next, we discuss the simulation of the array receiving a reflected signal that contains higher harmonics, and finally we give the resulting harmonic content of the received signal produced by the array.

5.1 Expected Array Response

The properties of the amplitude-steered array as a receiver are important for determining the response of the array to nonlinear propagation. The transmit signal contains only the fundamental frequency for each steering direction; however, due to the generation of harmonics, the received signal from a particular direction will also

contain higher frequencies. The array, in receive-mode, must reject these harmonics to avoid the appearance of false targets in the images.

We expect the received signal to approach the array at the same angle, or close to the same angle, that the emitted signal was transmitted. A flat target would produce the largest response if it is perpendicular to the insonifying beam. The reflection would then return to the array along the path of the incident beam, so for example, energy transmitted at a 30° angle relative to the array broadside will be received at a 30° angle relative to the array broadside. If the flat target were tilted to a small angle relative to the insonifying beam, the reflection might still be received by the array at a slightly different angle than the original angle of the transmitted signal. However, if the flat target were tilted to a large angle relative to the insonifying beam, then the reflection would be directed away from the array. Similarly, for a point target, which would scatter energy in all directions, only energy from a small range of angles close to the angle of the insonifying beam will be received by the array. This limit to the angle at which the received signal will approach the array is important because the amplitude-steered array accepts (or receives) different frequencies from different angles.

The amplitude-steered array acts as a spatial filter. We use a diagram of the array response in the temporal-frequency/spatial-frequency (ω–k) plane to show that the array will be able to reject higher harmonics that approach the array at the same direction as the fundamental frequency. First, Figure 5.1 shows the spatial and temporal frequency filtering characteristics for an array that uses time delays for beamforming. The figure shows ω versus k_y, where y is the coordinate in the vertical direction. We are interested in signals that approach the array at some vertical angle θ, where θ is measured from the array broadside direction. In the figure, red represents the main lobe of the array and ω is proportional to k_y ($\omega = \frac{k_y c}{\sin\theta}$, $\frac{c}{\sin\theta} = \text{constant}$), indicating that different frequencies are accepted at the same angle and attenuated at other angles of incidence.

In comparison, we show the spatial and temporal frequency filtering characteristics of the amplitude-steered array in Figure 5.2. The array used for this figure is 10 cm in

length, has an interelement spacing of 1.4 mm, and is steered to 30° at 100 kHz. From this figure, we see that the array accepts input of constant k_y value, and attenuates other values of k_y. Since k_y is proportional to frequency and the sine of the steering angle, constant k_y indicates that different frequencies are accepted at different angles of incidence. We make the angular dependence more clear in Figure 5.3 by showing the spatial and temporal frequency filtering properties of the amplitude-steered array as a function of steering angle, rather than of k_y. We can filter out signals of frequencies higher than our frequency range of interest (80–305 kHz), where grating lobes are most likely to occur. We conclude from this diagram that, in the absence of grating lobes, higher harmonics generated by nonlinear propagation will be rejected due to the spatial filtering of the array.

In the presence of grating lobes for frequencies within our range of interest, a narrow beamwidth allows the array to reject higher harmonics. With narrow beamwidths, the fundamental and higher frequencies accepted at a particular angle will have narrow bandwidths. Those higher frequencies generally will not be harmonics of the fundamental frequency steered to that direction. As an example, we have modified the array used for Figure 5.3. The interelement spacing has been increased by a factor of 4 and the total length of the array has been kept at 10 cm to generate Figure 5.4. In Figure 5.4 we show that although there are grating lobes present, the grating lobes do not correspond to harmonics of the fundamental frequency for any particular steering direction. For example, at 40°, the fundamental frequency is 72 kHz. The fourth and fifth harmonics are 288 kHz and 360 kHz, respectively. The grating lobe passes signals at 328 kHz.

Finally, when the array is small, and therefore the beamwidths are wide, higher harmonics may be accepted from the same direction as the fundamental frequency, and so the harmonics will affect the operation of the array. In Figure 5.5 we show an array with very wide beams. From the array used to generate Figure 5.3, the interelement spacing and total array length have been decreased by a factor of 8. At 30°, for example, the center frequency is 100 kHz, but the main lobe is wide enough that 200 kHz is also accepted, although it is somewhat attenuated. This example

shows a design problem that can be solved by increasing the array length. Therefore, we expect that nonlinear propagation will not cause the appearance of extraneous targets for well-designed arrays.

5.2 Field Simulation

We confirm our expected array response through simulation. No analytical solution currently exists to describe the nonlinear propagation of a sound beam. The difficulty in simulating nonlinear propagation arises from the combination of the effects of diffraction, interaction of harmonics, and attenuation. Many authors have considered numerical solutions to three-dimensional wave propagation in nonlinear media. Several algorithms exist for symmetrical sources with sinusoidal [39], [40] or pulsed excitation [41], [42], [43]. Some of the algorithms for sinusoidal excitation have been adapted for nonaxisymmetric sources with sinusoidal excitation [40], [44]. Those codes can also be used for pulsed excitation, but with huge computational cost due to the large number of harmonics needed to represent the distorted pulse.

We implemented two of the algorithms for simulation of nonlinear propagation. We use the algorithm by Christopher and Parker [40] to generate the data for our study. We use the algorithm by Aanonsen et al. [39] to compare our simulation results. We discuss Christopher and Parker's algorithm first, in order to introduce Burger's equation, and then we discuss Aanonsen's algorithm, which is based on an augmented Burger's equation.

5.2.1 Christopher and Parker's algorithm

Christopher and Parker use a two-substep algorithm, propagating the field over small steps, accounting for diffraction and attenuation in the spatial frequency domain in the first substep, and accounting for nonlinear effects in the temporal frequency domain in the second substep. The diffraction is solved using an exact solution to the Kirchoff-Helmholtz intergral, although there is some error associated with the finite transform size. Nonlinear effects are calculated using the frequency domain solution to Burger's equation. The results are accurate, even in the near field of the source.

Diffraction is included by convolving each harmonic field with an appropriate point spread function. This convolution is actually accomplished with multiplication in the spatial frequency domain. The point spread function is given by

$$h_n(\Delta z, r) = -\frac{1}{2\pi}\frac{\Delta z}{d^2}\left(jnk - \frac{1}{d}\right)e^{jnkd} \tag{5.1}$$

where Δz is the incremental distance in the direction of propagation, r is the lateral distance, $r = \sqrt{x^2 + y^2}$, $d = \sqrt{\Delta z^2 + r^2}$, k is the wavenumber, and n is the harmonic. If the source is axially symmetric, computational savings can be achieved by using the Hankel transform rather than the two-dimensional Fourier transform. The Hankel transform of the point spread function is

$$H_n(\Delta z, R) = \begin{cases} exp[j2\pi\Delta z\sqrt{(nf/c)^2 - R^2}] & |R| \leq nf/c \\ exp[-2\pi\Delta z\sqrt{R^2 - (nf/c)^2}] & |R| > nf/c \end{cases} \tag{5.2}$$

where R is the transform variable, the spatial frequency in the radial direction. Attenuation is included in this step in the spatial frequency domain by multiplying $H(\Delta z, R)$ by $exp[-\alpha(nf)^2(\Delta z/\cos(\sin^{-1}(Rc/f))]$, where α is the attenuation coefficient and f is the fundamental frequency. The algorithm accounts for linear effects in the spatial frequency domain, which requires the repeated use of discrete transforms. To avoid wraparound error, the transform of the point spread function is appropriately windowed [45].

The nonlinear effects are accounted for in the temporal frequency domain. A plane wave assumption is made, which means that all phase fronts are assumed to travel in the same direction as the fundamental, allowing the use of Burger's equation for calculating the accretion and depletion of harmonics. This assumption is only loosely justified [40]. Burger's equation is given by

$$\frac{\partial u}{\partial x} = \frac{\beta\omega_0}{c_0^2}u\frac{u}{\partial\tau} + \Gamma\frac{\partial^2 u}{\partial\tau^2} \tag{5.3}$$

where u is the particle velocity, x is the direction of propagation, τ is the retarded, dimensionless time $\tau = \omega_0 t - kx$, and Γ is the Gol'dberg number, the ratio between absorption length and shock formation distance.

The solution to Burger's equation is given by Trivett and van Buren [46] and by Haran and Cook [47], [48]. We write the form given by Christopher in [40]:

$$u_n(z+\Delta z,i) = u'_n(z+\Delta z,i) + j\frac{\beta\pi f\Delta z}{c^2}\left(\sum_{k=1}^{n-1} k u'_k u'_{n-k} + \sum_{k=n+1}^{N} n u'_k u'^{*}_{k-n}\right) \quad (5.4)$$

where u_n is the particle velocity for harmonic n, u'_n represents the output of the diffraction substep, Δz is the length that the field is advanced with each step of the algorithm, and f is the fundamental frequency.

This algorithm is implemented in Matlab, and the results are used to generate the reflected signal to be received by the amplitude-steered array.

5.2.2 Aanonsen's Algorithm

Several of the algorithms mentioned in the introduction to this section calculate the propagation of sound in a bounded beam using the Khokhlov-Zabolotskaya-Kuznetsov (KZK) equation. The KZK equation is a form of Burger's equation, augmented to include diffraction. The KZK equation was originally derived without absorption by Khokhlov and Zabolotskaya in 1969. Kuznetsov added absorption in 1971. Naze Tjøtta and Tjøtta later derived a nondimensional version of the equation using the method of multiple scales. The equation as written by Naze Tjøtta and Tjøtta is

$$\left(4\frac{\partial^2}{\partial\tau\partial\sigma} - \bar{\nabla}_\perp^2 - 4\alpha r_0\frac{\partial^3}{\partial\tau^3}\right)\bar{p} = 2\frac{r_0}{l_d}\frac{\partial^2}{\partial\tau^2}\bar{p}^2 \quad (5.5)$$

where τ is the normalized retarded time $\tau = (t - z/c)/T$ and the normalization time T for a periodic waveform is the period. The normalized axial distance σ equals z/r_0; the normalization distance r_0 is the Rayleigh distance, $r_0 = a^2/2cT$; α is the absorption coefficient; l_d is the plane wave shock formation distance; and $\bar{p}$ is the normalized acoustic pressure, $(p - p_0)/\rho_0 c u_0$ where u_0 is the source velocity. The $\bar{\nabla}_\perp^2\bar{p}$ term accounts for diffraction. Without the diffraction term, the KZK equation would reduce to Burger's equation.

The KZK equation is derived using the parabolic approximation, which means the acoustic variable, pressure or normal particle velocity, is assumed to vary slowly

in the direction of propagation. The solution is not correct very close to the source. The conversion between pressure and normal particle velocity is made using the plane wave impedance relation.

Aanonsen, Barkve, Naze Tjøtta, and Tjøtta formulated a solution to the KZK equation by assuming a Fourier series form for the pressure,

$$\bar{p} = \sum_{n=1}^{\infty} (g_n \sin n\tau + h_n \cos n\tau) \tag{5.6}$$

and substituting the solution into Equation (5.5). A coupled set of equations is obtained:

$$\begin{aligned}
\frac{\partial g_n}{\partial \sigma} &= -n^2 \alpha r_0 g_n + \frac{1}{4n} \bar{\nabla}_\perp^2 h_n \\
&\quad + n \frac{r_0}{2l_d} \left(\frac{1}{2} \sum_{p=1}^{n-1} (g_p g_{n-p} - h_p h_{n-p}) - \sum_{p=n+1}^{\infty} (g_{p-n} g_p + h_{p-n} h_p) \right) \qquad (5.7) \\
\frac{\partial h_n}{\partial \sigma} &= -n^2 \alpha r_0 h_n - \frac{1}{4n} \bar{\nabla}_\perp^2 g_n \\
&\quad + n \frac{r_0}{2l_d} \left(\frac{1}{2} \sum_{p=1}^{n-1} (h_p g_{n-p} + g_p h_{n-p}) + \sum_{p=n+1}^{\infty} (h_{p-n} g_p + g_{p-n} h_p) \right) \qquad (5.8)
\end{aligned}$$

where n is the number of the harmonic and n ranges from 1 to ∞.

We program Equations (5.7) and (5.8) in Matlab using an implicit backward finite difference algorithm to integrate, for stability. The results are used for comparison with the Christopher and Parker algorithm.

5.2.3 Simplifying assumptions

In order to show the effect of harmonic generation on the operation of our array, we simulate nonlinear propagation using Christopher and Parker's algorithm. We make several simplifying assumptions to reduce the complexity of the problem while still illustrating the effects.

First, we simulate the low frequency amplitude-steered array, rather than the high-frequency array. The geometry of the low frequency transmitter is approximately circular, as opposed to the extremely long and narrow geometry of the high frequency transmitter. Despite the symmetry of the low frequency array, we use the

two-dimensional FFT rather than the Hankel transform to calculate diffraction and attenuation, as the Hankel transform is not readily available in Matlab. The circular geometry allows us to calculate the field on a smaller grid of points in the lateral directions because we do not have to account for the large spreading in one dimension. The lower frequency also allows a lateral grid with fewer points because we can sample spatially at a lower rate due to the longer wavelength. In the axial direction, we can calculate fewer points because the variation in the near field is slower than for the high frequency array. Also, we do not have to propagate the field as far to reach the range of interest.

Second, we simulate a case where the nonlinear effect is not very strong. The stronger the nonlinearity (the greater the source amplitude), the more harmonics will be generated, greatly increasing the cost of computation. However, we know *a priori* that frequencies outside the range 80 kHz to 305 kHz are not generated at the source, so we can use a lowpass filter to remove frequencies higher than 305 kHz. Therefore, we do not have to consider the problem where such high harmonic frequencies are generated. We simulate a signal that oscillates sinusoidally at 100 kHz at the source, as it will generate a large number of harmonics within our frequency range of interest. We generate harmonics up to 400 kHz.

In the simulation of the field, we do not include beamsteering. The source is assumed to be a plane circular piston, not a steered array. With this assumption, the grid on which field points are calculated does not have to be large to accomodate the steering angle of the beam. Nor does the grid have to shift to follow the beam. The implication is that a field point on the axis of the simulated beam pattern for the piston source corresponds to a field point on the axis of the 100-kHz beam of the amplitude-steered array, which is steered to 30°. This assumption is reasonable for axial distances greater than or equal to a^2/λ, the near-field/far-field transition, which occurs at 0.17 cm in our case.

5.2.4 Values used in our simulation

Christopher and Parker offer guidelines in the use of their algorithm, based on their experience [40]. If shocks are expected, then 30 to 50 harmonics may be required. If no shocks are expected, 5 to 10 harmonics should be enough to characterize the field. We choose a souce amplitude such that no shock is expected. We calculate the field to 1 m, and the plane-wave shock formation distance is 1.983 m. Satisfactory results are obtained by using five harmonics.

The radial sampling should be fine enough to show the structure of the field for the highest harmonic. For simulations requiring 50 harmonics, radial sampling of four times the Nyquist rate for the fundamental should be adequate. If no shocks are expected, one or two times the Nyquist rate for the fundamental should be adequate. Our fundamental frequency is 100 kHz, which corresponds to a wavelength of 1.5 cm. We use a lateral step size of 3 mm, which is smaller than half the Nyquist step size for the fundamental.

Finally, the step size in the axial direction is chosen to accurately represent the axial variations in the near field. The step size should also be chosen to account for the attenuation of the highest harmonic. That is, the step size should be made small enough that the magnitude of the highest harmonic at the end of the step does not decrease to less than 0.7 times the magnitude at the beginning of the step due to attenuation. In our case, the first condition is more restrictive. We use an axial step size of 1 mm.

5.2.5 Validation of simulation

Our simulation is validated two ways. First we compare our implementation of Christopher and Parker's algorithm with Ted Christopher's results for one case. Christopher and Parker have already satisfactorily compared their results to theory [40]. The case is a piston source with 5-cm radius. The source intensity is 20 W/cm^2, corresponding to an initial normal particle velocity of 51.6 cm/s. The medium is water, so the attenuation coefficient is 25×10^{-15} Np/m-Hz^2 and β is 3.5. The results of our simulation using Christopher and Parker's algorithm are compared with the

results from Christopher's implementation of the algorithm in Figure 5.6. For each harmonic, the maximum amplitude calculated by Ted Christopher is larger than the maximum amplitude calculated by our program. However, the differences are small. Our results are satisfactory for our purpose, which is to show how the amplitude-steered array will accept or reject harmonics.

Second, we compare our results to results calculated using Aanonsen's algorithm for the same case described above. The results for the first three harmonics are shown in Figure 5.7. The agreement between our calculated results and those using Aanonsen's algorithm are good, but not as good as the agreement between our implementation of Christopher's algorithm and his results, which is expected since in the previous comparison, the algorithms were the same. The results using Aanonsen's algorithm are not accurate close to the source, where the parabolic approximation fails. The results using Aanonsen's algorithm also show a higher peak particle velocity and then a faster decline in particle velocity for the fundamental frequency. Ted Christopher's results also showed a higher peak than we calculated; however, in both cases the agreement is reasonable.

5.3 Simulation of Array Operation and Results

Once the field generated by the array is simulated, the data are input into a simulation by Field II to generate the array response. Harmonic amplitudes and phases generated in the nonlinear field simulation using Christopher and Parker's algorithm are inverse Fourier transformed to generate the signal, which will be the signal reflected by a point target at that field point. The point reflector is taken from an axial position in the nonlinear simulation. The transmitted field is assumed to be reflected by a point target at a range of 80 cm along the 30° direction, corresponding to the steering direction for 100 kHz. The maximum array response is steered in the vertical direction but not in the horizontal direction. The reflected field is assumed to propagate back to the array linearly because only a small fraction of the incident energy will be reflected by a point target. Nonlinear effects in the reflected wave therefore will be insignificant.

The truncated signal that is radiated by the point source and the magnitude of its Fourier transform are shown in Figure 5.8. Four harmonics are used to form the signal. The signal has a length of 1 ms, but only one fourth of it is shown to give a clearer figure. Although the nonlinear effect is by design not strong, the peak positive and peak negative pressures are not symmetric.

The magnitude of the Fourier transform of the signal received by the amplitude-steered array is shown in Figure 5.9. The array is 10 cm in length, with an interelement spacing of 1.6 mm, and it is designed to steer to 30° at 100 kHz. The amplitude of the transform has been normalized, and for comparison the amplitudes of the signal harmonics before reception are shown as dots. The harmonics have been attenuated and are no longer visible.

For comparison in Figure 5.10, we show an array that has the same diameter as the original array, but with interelement spacing increased by a factor of 4, so that grating lobes are present. Again, dots in the figure represent the amplitudes of the harmonics before reception by the array. The harmonics are attenuated, but not as well as in the previous case.

Finally in Figure 5.11, we show the results of receiving the same signal with an array of smaller total size. The interelement spacing and total array length have been decreased by a factor of 8. The received beam pattern does not have any grating lobes, but the beamwidth is very wide. Here we see that the higher harmonics are not attenuated as much as in either of the previous two cases.

5.4 Conclusion

In this chapter, we have examined the effect of nonlinear propagation on the performance of the amplitude-steered array. The concern was that harmonics generated during propagation would appear as false targets in the image. We simulated the nonlinear propagation from a piston source, whose dimensions and operating frequency correspond to those of the low frequency amplitude-steered array. The waveform for a spatial point on the beam axis of the piston was formed and assumed to be a reflected waveform in a simulation of the operation of the amplitude-steered array. In

this second simulation, the position of the spatial point was shifted so that it corresponds to a point the same distance away, but along the beam axis of the 100-kHz beam, which was steered to 30° for the amplitude-steered array. The received signal was then formed. We have shown that in the received signal the higher harmonics are attenuated due to the spatial filtering properties of the array. For larger beamwidths, harmonics are accepted by the array, which means that they would appear as false targets in the image. However, nonlinear propagation does not have to cause false targets in the images for a properly designed array, that is, an array that is long enough.

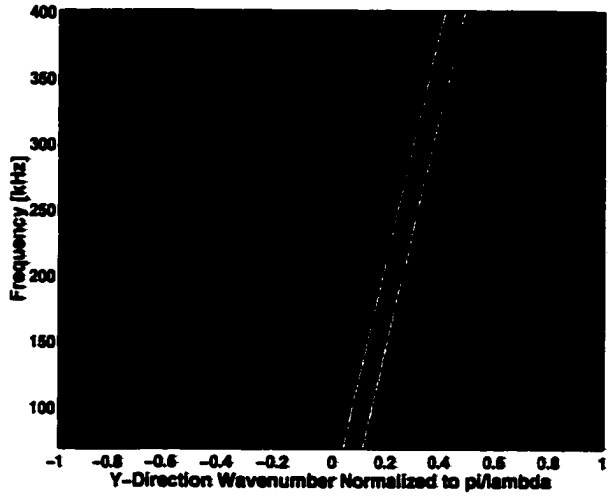

Figure 5.1: ω–k diagram for an array that uses time delays for beamforming.

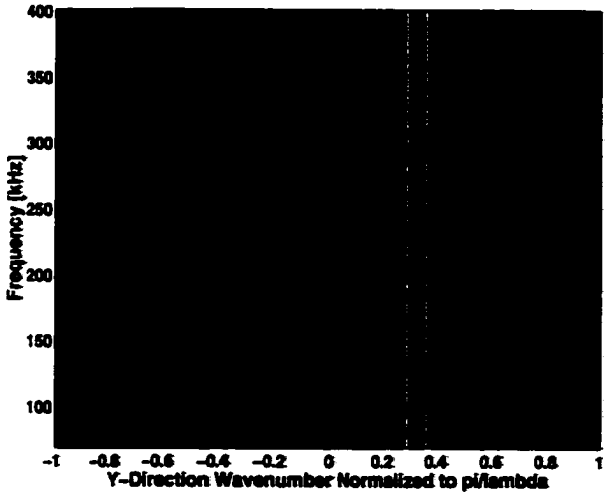

Figure 5.2: ω-k diagram for the amplitude-steered array, which uses amplitude weighting for beamforming.

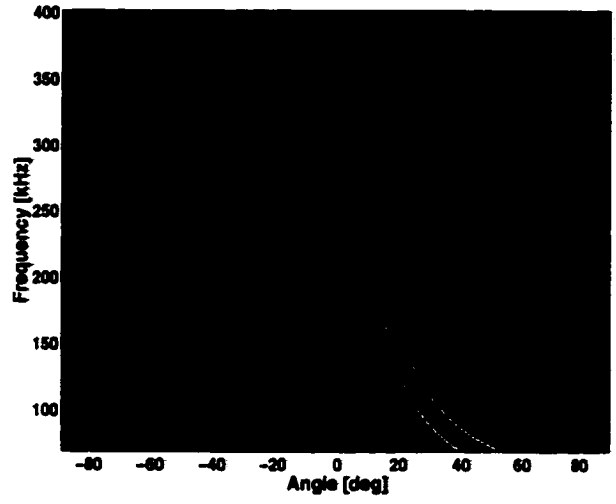

Figure 5.3: Spatial and temporal filtering properties of the amplitude-steered array.

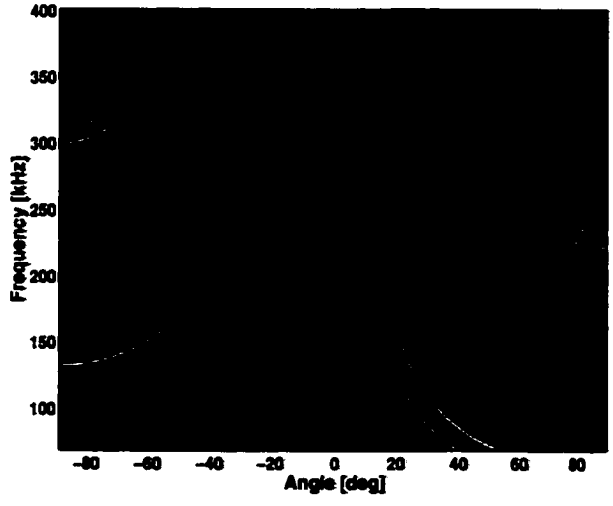

Figure 5.4: Spatial and temporal filtering properties of an amplitude-steered array, with the same length, but fewer elements.

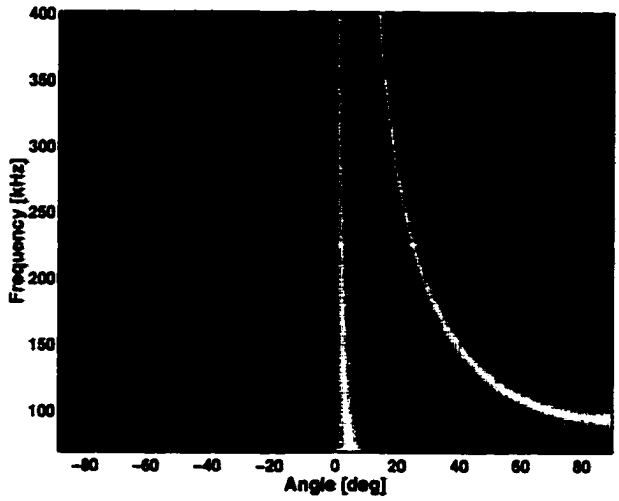

Figure 5.5: Spatial and temporal filtering properties of an amplitude-steered array with shorter length and fewer elements.

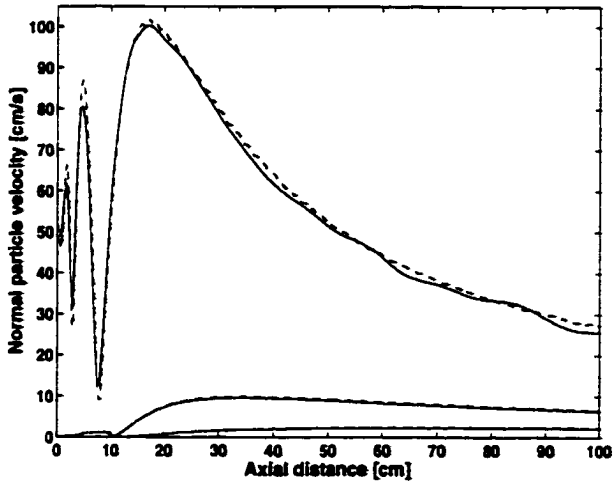

Figure 5.6: Comparison of simulated results (solid lines) with Christopher's results (dashed lines). The fundamental (considered the first harmonic) and two higher harmonics are shown.

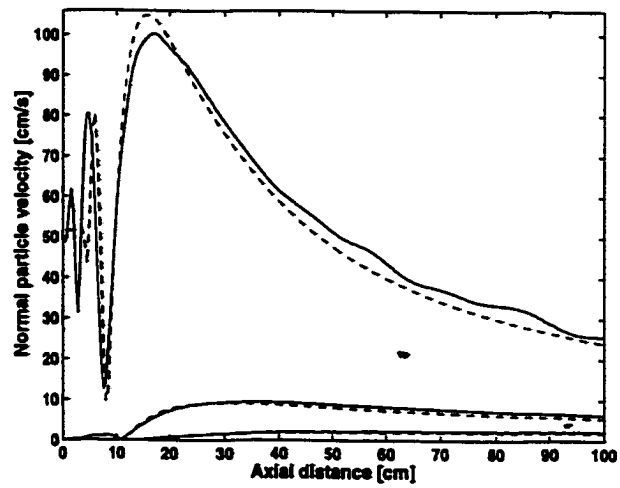

Figure 5.7: Comparison of simulated results (solid lines) with results from Aanonsen's algorithm (dashed lines). The fundamental (considered the first harmonic) and two higher harmonics are shown.

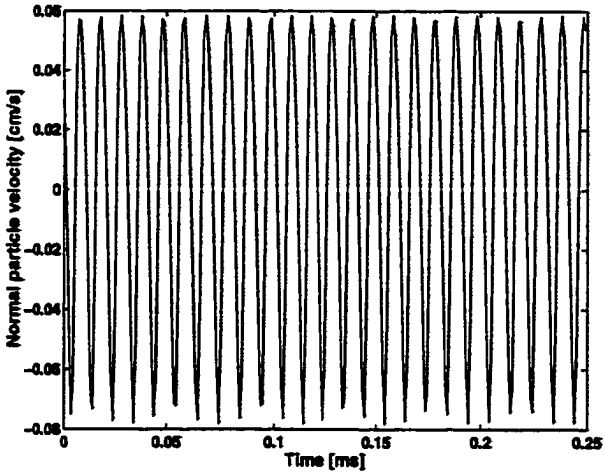

(a)

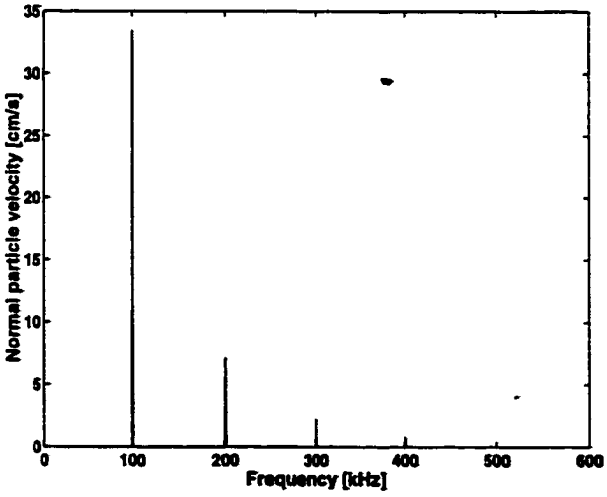

(b)

Figure 5.8: Signal generated by simulation of nonlinear field propagation: (a) time signal, (b) harmonic components.

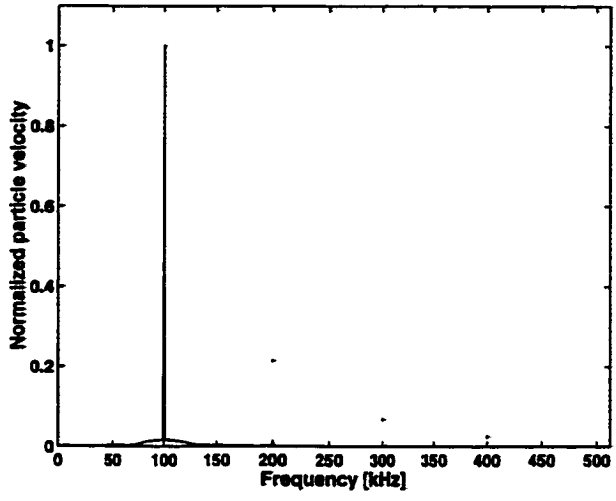

Figure 5.9: Fourier transform of the received signal using the low frequency amplitude-steered array.

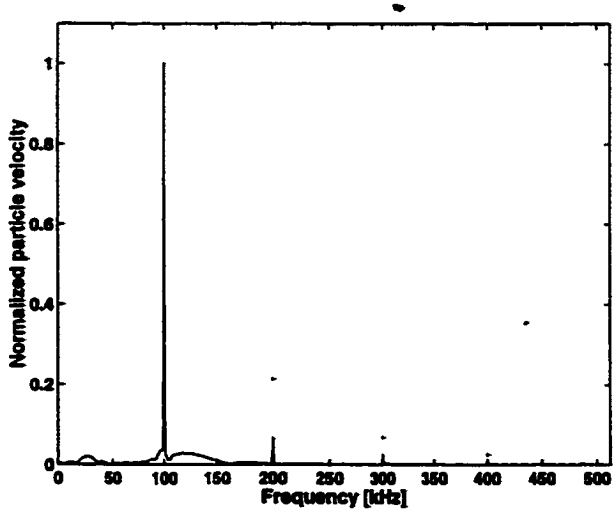

Figure 5.10: Fourier transform of the received signal using the low frequency amplitude-steered array. Interelement spacing has been increased without increasing the total length of the array, so that grating lobes are present.

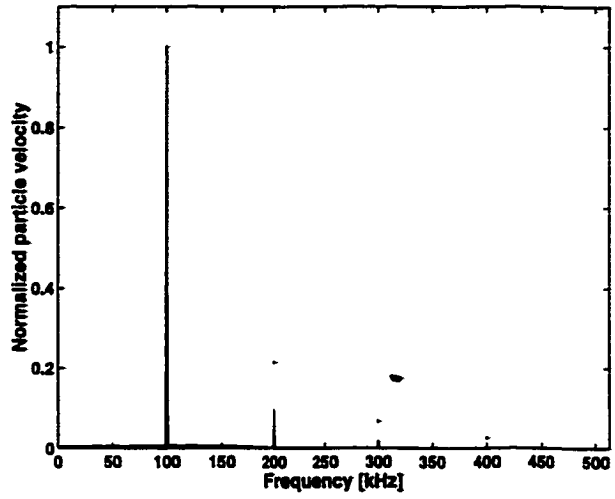

Figure 5.11: Fourier transform of the received signal using the low frequency amplitude-steered array. Interelement spacing has been decreased, changing the total length of the array by a factor of 8, so that beamwidths are greater.

CHAPTER 6

CONCLUSION

Acoustic volumetric imaging is difficult to accomplish in real time due to the speed of sound and the resulting time required to collect data. Conventional methods of data collection require the transmission and reception of at least one pulse per line in the image. For three-dimensional imaging, a reasonable set of data is 100 by 100 lines. The time to collect each line depends on the range of interest. For ranges more than a few centimeters, in order to be able to refresh the volume of data 30 times each second, innovative methods of data collection are required.

This thesis is a comprehensive study of the application of the amplitude-steered array to real-time volumetric acoustic imaging. Previously the linear amplitude-steered array had been used for narrow-band signal detection. The current project seeks to build an acoustic volumetric imaging system that is based on a two-demensional version of this array. The project has involved many groups working on various aspects of system design and implementation including crystal growth, electronics design, and building the array from the crystal (dicing and electrically connecting elements). The work presented in this thesis contributed to the analysis of the acoustic array operation and to the development of imaging algorithms.

6.1 Summary of Research Results

The specific research results produced by the author and presented in this thesis are listed here with some discussion.

- Demonstration of the tradeoff between axial and lateral resolution, which are related by the length of the array.

Initially it was unclear how two targets separated only in range could be distinguished with an array that spatially separates frequencies. If frequencies were perfectly separated, a point target would return a sinusoidal signal that was infinitely long. It was shown that targets separated only in range could be distinguished because frequencies were not separated perfectly, but rather overlapped. As a result, it was shown that there was a relationship between axial and lateral resolution. The width of the beam at each frequency decreases as the array length increases. Thus the overlap of frequencies decreases as the array length increases, leading to poorer axial resolution as lateral resolution improves.

- Analysis of time-frequency distributions for image formation.

  The spectrogram was initially proposed as the means to form an image from the signal received by the array. However, there is an inherent tradeoff between time (axial) and frequeny (lateral) resolution in the spectrogram that depends on the length of the window used for processing. Other distributions had different tradeoffs in time and frequency resolution and cross-term level. The smoothed pseudo-Wigner distribution (SPWD) produced the best combination of axial and lateral resolution, while reducing cross-term levels. Because the SPWD applies smoothing separately in the time and frequency directions, it has the most available parameters that can be adjusted to optimize axial and lateral resolution and to reduce cross-terms.

- Incremental development of the array layout to show that a sparse random array could be used.

  Each of the array designs originated at the Applied Research Laboratory at the Pennsylvania State University. The final array design was a random design that led to a narrow beamwidth with no inordinately high sidelobes. However, the fully sampled array may have too many elements to be implemented with current array fabrication technology, despite needing only four channels per stave rather than one channel per element. Therefore, it was shown that a

beam pattern with a narrow main lobe, but higher average sidelobe level could be achieved with a sparse random design. Average sidelobe level increases with the sparseness of the array.

- Development of projection algorithms to display data with reduced processing.

  Once the three-dimensional data set has been collected, it must be displayed on a two-dimensional screen. Therefore, several processing algorithms were presented for displaying the data. The three-projection method was adopted due to the amount of information displayed for the amount of processing. By forming only the three projection images, and not the entire volume of data, fewer time-frequency distributions had to be calculated. The projection through vertical angle used one Hilbert transform for each horizontal steering direction. The projection through range used one Fourier transform per horizontal steering direction. And the projection through horizontal angle used one calculation of the time-frequency distribution. In contrast, the surface rendering techniques presented showed only one view of the target. Forming slice images or trying to do more sophisticated volume rendering would require the calculation of one time-frequency distribution per horizontal steering direction.

- Demonstration that nonlinear propagation did not have to lead to false targets in the images.

  The processing of data from the amplitude-steered array equates frequency with target position, so it is possible for the generation of harmonics through nonlinear propagation to cause the appearance of false targets in the image. Although nonlinear propagation will cause the generation of harmonics, the spatial filtering properties of the array cause harmonics to be attenuated, as long as the beamwidths are narrow enough and as long as the number of grating lobes within the frequency range of interest is not extensive.

- Verification of simulations through comparison with experiment.

  The demonstration of all of the previously mentioned results was accomplished

through simulation of the array operation. In order to confirm the results, experimental data were collected at the Applied Research Laboratory at the Pennsylvania State University. Analysis of the data and comparison to simulation were accomplished by the author. Comparison between simulated and experimental results showed very good agreement, particularly for point-like targets.

6.2 Future Work

The amplitude-steered array has been characterized for imaging, and algorithms have been designed for processing data from a volumetric imaging system. The actual implementation of the system involves other issues which are currently being investigated. In addition, the use of the array for other applications should be investigated. Some of these issues are discussed below.

6.2.1 Environmental factors

The study of the array operation was carried out through simulation and through operation in a controlled water tank. The actual system will operate in a much more varied environment, which will induce more noise. The effects of current, temperature and pressure gradients, and water turbidity should be determined, although it is expected that temperature and pressure will not vary much over the desired operating range of 5 m. Also, the effect of noise on the image formation algorithms should be determined. The smoothed pseudo-Wigner distribution should not be greatly affected due to the the low-pass filter in each direction.

6.2.2 Full two-dimensional amplitude-steered array

The two-dimensional array discussed in this thesis is an amplitude-steered array in one dimension and a linear phased array in the other dimension. Three-dimensional data are collected with the transmission of a single pulse because the transmitter is narrow in one direction, leading to a broad beam in that direction. A full two-dimensional amplitude-steered array would steer a beam in two directions by changing

frequency. Most likely, to have such a system, amplitude-steering would have to be combined with pulse coding. Using frequency steering in two dimensions would cause a rotated line of data to be collected.

6.2.3 Medical imaging

Our array was discussed within the framework of an underwater imaging system. But the technology could also be used for medical imaging, for example, real-time imaging of the heart. Compared to underwater imaging, some of the requirements on our array could be relaxed for medical imaging, which would make the fabrication and operation easier. This is largely due to the much smaller range of interest. The array could be smaller, meaning many fewer elements. We could use a linear amplitude-steered array that is rocked or rotated to collect the data because there is time to transmit multiple pulses. Our transmit pulse would have to be much shorter to reduce the "dead zone" so that features close to the transducer could be imaged.

REFERENCES

[1] T. R. Nelson and D. H. Pretorius, "Three-dimensional ultrasound imaging," *Ultrasound Med. Biol.*, vol. 24, pp. 1243–1270, Sept. 1998.

[2] S. Berg, H. Torp, D. Martens, E. Steen, S. Samstad, I. Høivik, and B. Olstad, "Dynamic three-dimensional freehand echocardiography using raw digital ultrasound data," *Ultrasound Med. Biol.*, vol. 25, pp. 745–753, May 1999.

[3] R. Canals, G. Lamarque, and P. Chatain, "Volumetric ultrasound system for left ventricle motion imaging," *IEEE Trans. Ultrason. Ferroelect. Freq. Cont.*, vol. 46, pp. 1527–1538, Nov. 1999.

[4] D. H. Turnball and F. S. Foster, "Beam steering with pulsed two-dimensional transducer arrays," *IEEE Trans. Ultrason. Ferroelect. Freq. Cont.*, vol. 38, pp. 320–333, July 1991.

[5] S. W. Smith and E. D. Light, "Two-dimensional array transducers using thick film connection technology," *IEEE Trans. Ultrason. Ferroelect. Freq. Cont.*, vol. 40, pp. 727–734, Nov. 1993.

[6] R. L. Goldberg and S. W. Smith, "Multilayer piezoelectric ceramics for two-dimensional array transducers," *IEEE Trans. Ultrason. Ferroelect. Freq. Cont.*, vol. 41, pp. 761–771, Sept. 1994.

[7] R. E. Davidsen and S. W. Smith, "Two-dimensional arrays for medical ultrasound using multilayer flexible circuit interconnection," *IEEE Trans. Ultrason. Ferroelect. Freq. Cont.*, vol. 45, pp. 338–348, Mar. 1998.

[8] G. R. Lockwood, J. R. Talman, and S. S. Brunke, "Real-time 3-D ultrasound imaging using sparse synthetic aperture beamforming," *IEEE Trans. Ultrason. Ferroelect. Freq. Cont.*, vol. 45, pp. 980–988, July 1998.

[9] J. Shen and E. S. Ebbini, "A new coded-excitation ultrasound imaging system – Part I: Basic principles," *IEEE Trans. Ultrason. Ferroelect. Freq. Cont.*, vol. 43, pp. 131–140, Jan. 1996.

[10] J.-Y. Lu, "2D and 3D high frame rate imaging with limited diffraction beams," *IEEE Trans. Ultrason. Ferroelect. Freq. Contr.*, vol. 44, pp. 839–856, July 1997.

[11] J.-Y. Lu, "Experimental study of high frame rate imaging with limited diffraction beams," *IEEE Trans. Ultrason. Ferroelect. Freq. Cont.*, vol. 45, pp. 84–97, Jan. 1998.

[12] S. W. Smith, H. G. Pavy, Jr., and O. T. von Ramm, "High-speed ultrasound volumetric imaging system – Part I: Transducer design and beam steering," *IEEE Trans. Ultrason. Ferroelect. Freq. Cont.*, vol. 38, pp. 100–108, Mar. 1991.

[13] I. S. F. Jones, "High resolution underwater acoustic imaging," *in Proceedings of Oceans 1999 MTS/IEEE*, 1999, pp. 1093–1097.

[14] V. Murino, C. S. Regazzoni, A. Trucco, and G. Vernazza, "A noncoherent correlation technique and focused beamforming for ultrasonic underwater imaging: A comparative analysis," *IEEE Trans. Ultrason. Ferroelect. Freq. Cont.*, vol. 41, pp. 621–630, Sept. 1994.

[15] C. Ishihara, T. Aoki, O. Takano, N. Ishii, S. Hisamoto, H. Yuasa, and Y. Tamura, "Holographic 3-D imaging system using encoded wavefront: An underwater imaging system," *Acoust. Imaging*, vol. 21, pp. 765–772, 1995.

[16] E. O. Belcher, H. Q. Dinh, D. C. Lynn, and T. J. Laughlin, "Beamforming and imaging with acoustic lenses in small, high-frequency sonars," *Proceedings. of Oceans 1999 MTS/IEEE*, vol. 3, pp. 1495–1499, 1999.

[17] B. Kamgar-Parsi, B. Johnson, D. L. Folds, and E. O. Belcher, "High-resolution underwater acoustic imaging with lens-based systems," *Int. J. Imaging Syst. Technol.*, vol. 8, pp. 377–385, July 1997.

[18] K. Erikson, A. Hairston, A. Nicoli, J. Stockwell, and T. White, "128 × 128 (16K) ultrasonic transducer hybrid array," *Acoustical Imaging*, vol. 23, pp. 485–494, 1998.

[19] F. L. Lizzi and K. W. Weil, "Frequency-controlled scanning of ultrasound beams," United States Patent 4,350,917, Sept. 21, 1982.

[20] W. J. Hughes and W. Thompson, Jr., "Tilted directional response patterns formed by amplitude weighting and a single 90° phase shift," *J. Acoust. Soc. Am.*, vol. 59, pp. 1040–1045, May 1976.

[21] E. J. Skudrzyk, *The Foundations of Acoustics.* New York: Springer-Verlag, 1971.

[22] D. A. Christensen, *Ultrasonic Bioinstrumentation.* New York: John Wiley and Sons, 1988.

[23] A. D. Pierce, *Acoustics: An Introduction to Its Physical Principles and Applications.* Woodbury, NY: Acoustical Society of America, 1989.

[24] D. C. Munson, Jr., and R. L. Visentin, "A signal processing view of strip-mapping synthetic aperture radar," *IEEE Trans. Acoust. Speech Sig. Proc.*, vol. 37, pp. 2131–2147, Dec. 1989.

[25] J. A. Jensen, "Field: A program for simulating ultrasound systems," *Med. Biol. Engr. Comp.*, vol. 34, no. 1, Suppl. 1, pp. 351–353, 1996.

[26] J. A. Jensen, "FIELD II," program available at http://www.it.dtu.dk/~jaj/field/field.html.

[27] L. R. Dragonette, D. M. Drumheller, C. F. Gaumond, D. H. Hughes, B. T. O'Connor, N.-C. Yen, and T. J. Yoder, "The application of two-dimensional signal transformations to the analysis and synthesis of structural excitations observed in acoustical scattering," *Proc. of the IEEE*, vol. 84, pp. 1249–1263, Sept. 1996.

[28] P. Chevret, N. Gache, and V. Zimpfer, "Time-frequency filters for target classification," *J. Acoust. Soc. Am.*, vol. 106, pp. 1829–1837, Oct. 1999.

[29] J. C. Brown, "Calculation of a constant-Q spectral transform," *J. Acoust. Soc. Am.*, vol. 89, pp. 425–434, Jan. 1991.

[30] T. A. C. M. Claasen and W. F. G. Mecklenbrauker, "The Wigner distribution – A tool for time-frequency signal analysis, Part II: Discrete-time signals," *Philips J. Res.*, vol. 35, no. 4/5, pp. 276–300, 1980.

[31] L. Cohen, "Time-frequency distributions – A review," *Proc. IEEE*, vol. 77, pp. 941–981, July 1989.

[32] H.-I. Choi and W. J. Williams, "Improved time-frequency representation of multicomponent signals using exponential kernels," *IEEE Trans. Acoust. Speech Sig. Proc.*, vol. 37, pp. 862–871, June 1989.

[33] F. Hlawatsch and G. F. Boudreaux-Bartels, "Linear and quadratic time-frequency signal representations," *IEEE Sig. Proc. Mag.*, vol. 9, pp. 21–67, Apr. 1992.

[34] D. L. Jones and T. W. Parks, "A resolution comparison of several time-frequency representations," *IEEE Trans. Sig. Proc.*, vol. 40, pp. 413–420, Feb. 1992.

[35] W. J. Pielemeier, G. H. Wakefield, and M. H. Simoni, "Time-frequency analysis of musical signals," *Proc. IEEE*, vol. 84, pp. 1216–1230, Sept. 1996.

[36] B. D. Steinberg, "Comparison between the peak sidelobe of the random array and algorithmically designed aperiodic arrays," *IEEE Trans. Ant. Prop.*, vol. AP–21, pp. 366–370, May 1973.

[37] B. D. Steinberg, "The peak sidelobe of the phased array having randomly located elements," *IEEE Trans. Ant. Prop.*, vol. AP–20, pp. 129–136, Mar. 1972.

[38] D. H. Johnson and D. E. Dudgeon, *Array Signal Processing: Concepts and Techniques*. Englewood Cliffs, NJ: Prentice Hall, 1993.

[39] S. I. Aanonsen, T. Barkve, J. N. Tjøtta, and S. Tjøtta, "Distortion and harmonic generation in the nearfield of a finite amplitude sound beam," *J. Acoust. Soc. Am.*, vol. 75, pp. 749–768, Mar. 1984.

[40] P. T. Christopher and K. J. Parker, "New approaches to nonlinear diffractive field propagation," *J. Acoust. Soc. Am.*, vol. 90, pp. 488–499, July 1991.

[41] Y.-S. Lee and M. F. Hamilton, "Time-domain modeling of pulsed finite-amplitude sound beams," *J. Acoust. Soc. Am.*, vol. 97, pp. 906–917, Feb. 1995.

[42] M. A. Averkiou and M. F. Hamilton, "Nonlinear distortion of short pulses radiated by plane and focused circular pistons," *J. Acoust. Soc. Am.*, vol. 102, pp. 2539–2548, Nov. 1997.

[43] J. Tavakkoli, D. Cathignol, R. Souchon, and O. A. Sapozhnikov, "Modeling of pulsed finite-amplitude focused sound beams in time domain," *J. Acoust. Soc. Am.*, vol. 104, pp. 2061–2072, Oct. 1998.

[44] A. C. Baker, A. M. Berg, A. Sahin, and J. N. Tjøtta, "The nonlinear pressure field of plane, rectangular apertures: Experimental and theoretical results," *J. Acoust. Soc. Am.*, vol. 97, pp. 3510–3517, June 1995.

[45] P. T. Christopher and K. J. Parker, "New approaches to the linear propagation of acoustic fields," *J. Acoust. Soc. Am.*, vol. 90, pp. 507–521, July 1991.

[46] D. H. Trivett and A. L. van Buren, "Propagation of plane, cylindrical, and spherical finite amplitude waves," *J. Acoust. Soc. Am.*, vol. 69, pp. 943–949, Apr. 1981.

[47] M. E. Haran and B. D. Cook, "Distortion of finite amplitude ultrasound in lossy media," *J. Acoust. Soc. Am.*, vol. 73, pp. 774–779, Mar. 1983.

[48] D. H. Trivett and A. L. van Buren, "Comments on 'Distortion of finite amplitude ultrasound in lossy media,' by M. E. Haran and B. D. Cook [J. Acoust. Soc. Am. 73, 774-779 (1983)]," *J. Acoust. Soc. Am.*, vol. 76, pp. 1257–1258, Oct. 1984.

APPENDIX A

DERIVATION OF PRESSURE EXPRESSIONS

We derive the expression for the far-field pressure produced by an array of finite sources with weighting for sidelobe reduction and with electronic phase shifts for beamsteering. Some simplifications are made to arrive at the equations used in Chapter 2. Also, we show that apodization for lowering sidelobes can be used with amplitude-weighting for beamsteering.

Geometry and variables are defined in Figure A.1. There are N elements of the array, labelled $\frac{-(N-1)}{2}$ to $\frac{N-1}{2}$. Each element is a line source of length a. The interelement spacing is d, measured as the distance between the center points of two adjacent elements. The signals from each element are weighted with a factor $w(n)$ to lower sidelobes, and phase-shifted with a factor $e^{j2n\phi}$ to steer the main lobe to θ_0, where $\phi = \frac{k_0 d}{2} sin(\theta_0)$.

The pressure observed at point OP is given by the expression

$$P(r,\theta) = \sum_n \int_{\frac{-a}{2}}^{\frac{a}{2}} w(n) \frac{P_0}{4\pi r'} e^{j(\omega t - kr' - 2n\phi)} dx \qquad \text{(A.1)}$$

where r' is the distance from the position x on an element to the observation point, and P_0 is the pressure amplitude of the point source, related to the initial velocity.

$$r' = r - x\sin\theta - nd\sin\theta \qquad \text{(A.2)}$$

where r is the distance of to the observation point from the center of the array.

In Equation (A.1), we replace $2n\phi$ with $nk_0 d\sin\theta_0$. In the denominator of the integrand, we replace r' with r. In the exponent, we replace r' with the full expression

given in Equation (A.2):

$$P(r,\theta) = \sum_n \int_{\frac{-a}{2}}^{\frac{a}{2}} w(n) \frac{P_0}{4\pi r} e^{j(\omega t - kr + kx\sin\theta + knd\sin\theta - k_0 nd\sin\theta_0)} dx \tag{A.3}$$

Then we move terms out of the sum or integral as we can:

$$P(r,\theta) = \frac{P_0 e^{j(\omega t - kr)}}{4\pi r} \underbrace{\sum_n w(n) e^{jnd(k\sin\theta - k_0\sin\theta_0)}}_{\text{DTFT of weights, } w(n)} \int_{\frac{-a}{2}}^{\frac{a}{2}} e^{jkx\sin\theta} dx \tag{A.4}$$

The sum and integral terms can be simplified separately. The sum term is a discrete time Fourier transform (DTFT) of the element weights, where the general DTFT is expressed as $X_d(\lambda) = \sum_{n=-\infty}^{\infty} x_n e^{-j\lambda n}$. In our expression, $\lambda = -d(k\sin\theta - k_0\sin\theta_0)$. Evaluating the integral results in a sinc function.

In order to continue the derivation of equations in Chapter 2, we choose a rectangular weighting function so that $w(n) = 1$ for all n. We could choose a different weighting function, such as a Hanning window, that would produce lower sidelobes:

$$P(r,\theta) = \frac{P_0 e^{j(\omega t - kr)}}{4\pi r} \frac{\sin(\frac{Nd}{2}(k\sin\theta - k_0\sin\theta_0))}{\sin(\frac{d}{2}(k\sin\theta - k_0\sin\theta_0))} \frac{\sin(\frac{ka}{2}\sin\theta)}{\frac{ka}{2}\sin\theta} \tag{A.5}$$

If a is very small, i.e., if the elements of the array are point elements, the final sinc function is equal to 1 for all angles, corresponding to Equation (2.9) of Chapter 2.

Now we assume we have an array of point sources, we remove the assumption that the weighting function is rectangular, and we evaluate the sum term of Equation (A.4) to find weights for an amplitude-steered array with lowered sidelobes. Note that common windows used to lower sidelobes are symmetric, so that $w(n) = w(-n)$. We begin with the expression

$$H(\theta) = \frac{1}{N} \sum_n w(n) e^{jnd(k\sin\theta - k_0\sin\theta_0)} \tag{A.6}$$

where N is assumed to be odd and n takes values from $\frac{-(N-1)}{2}$ to $\frac{N-1}{2}$. We replace $\frac{kd}{2}\sin\theta$ with u, and $\frac{k_0 d}{2}\sin\theta_0$ with ϕ. Combining terms with the same absolute value of n gives

$$H(\theta) = \frac{1}{N}\left\{ w(0) + \sum_{n=1}^{\frac{N-1}{2}} 2 * w(n)\cos(n(u-\phi)) \right\} \tag{A.7}$$

Using the trigonometric identity for the cosine of a sum, we obtain

$$H(\theta) = \frac{1}{N}\left\{ w(0) + \sum_{n=1}^{\frac{N-1}{2}} 2 * w(n)\cos(nu)\cos(n\phi) + 2 * w(n)\sin(n\phi)\sin(nu) \right\} \quad \text{(A.8)}$$

The terms in the sum can be written to give the same form as Equation (2.5), but we can also see from this form the weights for the combination of beamsteering and sidelobe reduction. Where in Chapter 2 we used weights of $\cos(2n\phi)$ and $\sin(2n\phi)$ for arrays with an odd number of elements, we now have weights of $w(n)\cos(2n\phi)$ and $w(n)\sin(2n\phi)$. Using this derivation, we have shown how to calculate amplitude weights for the combination of beamsteering and sidelobe reduction.

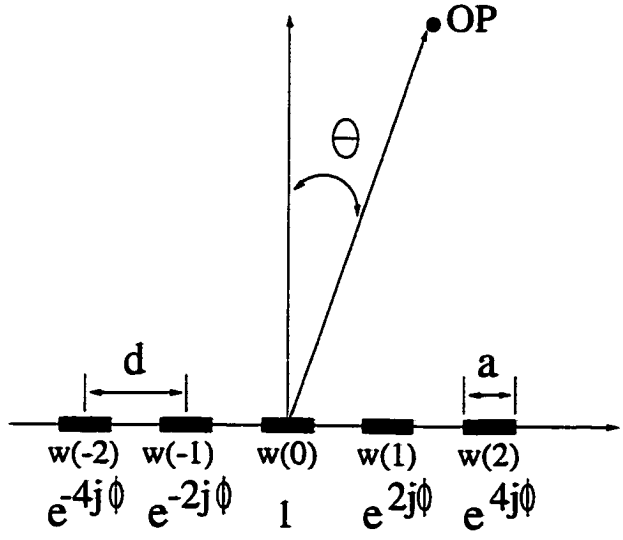

Figure A.1: Definition of variables for derivation.

APPENDIX B

SIMULATION CODE

The Matlab code for simulating data collection is listed here. This program simulates transmitting on cosine elements and receiving on cosine elements. Similar code is used to simulate the other three cases: transmitting on cosine element, receiving on sine elements; transmitting on sine elements, receiving on cosine elements; and transmitting on sine elements, receiving on sine elements. This code implements the block diagram of Figure 3.11 on page 64.

```
% drdncc.m              10 Jun 1999              cahf
%  This version accomodates several changes in the design,  8 Jun 1999.
%     * number of staves (396)
%     * stave spacing    (254 microns)
%     * frequency range  (1-5 MHz)
%
%  Simulation of the linear phased doily array operation
%     with recording of signals from individual staves
%     so that radon transform may be applied for beamforming.
%  This program should take a very long time to generate
%     data, so the processing has been taken out.
%  Four programs must be run to collect all the data:
%     1. drdncc.m
%     2. drdncs.m
%     3. drdnsc.m
%     4. drdnss.m
%     They can be run in any order.
%

tic;
clear
format long g;

fs = 20*1024000;                % [Hz] sampling frequency
c = 1500;                       % [m/s] sound speed in medium  1483
%nele = 396;                     % number of staves
wd = 0.224/1000;
ht = 0.186/1000;
krf = .030/1000;
```

```
focus = [0 0 4];                % used only for defining aperture
tx_t = 0.00005;                 % [s] duration of transmit signal
rad = 180/pi;                   % conversion
ddtheta = 5;                    % [deg] Doily design angle
ddfreq = 5000000;               % [Hz] Doily design freq
dfarg = ddfreq*sin(ddtheta/rad); % parameter to get steering angle
fstart = 1000000;               % [Hz] sweep start frequency
fstop = 5000000;                % [Hz] sweep end frequency

set_field('use_att',0);         % no attenuation
set_field('c',c);
set_field('fs',fs);
set_field('use_rectangles',1);

%%%%  TRANSDUCER DESCRIPTION

load sb02_array.mat;            % tx_array and rc_array
[atx, btx] = size(tx_array);
[arc, brc] = size(rc_array);

temp = tx_array;                % Flip arrays to put them in Field correctly.
                                % MEG figured this out.
tx_array = flipud(tx_array);
tx_array = tx_array.';
temp = rc_array;
rc_array = flipud(rc_array);
rc_array = rc_array.';

tx_en_cos = abs(real(tx_array)); % Separating sin and cos for transmit.
rc_en_cos = abs(real(rc_array));
rc = zeros(size(rc_array));
tx_apod_cos = reshape(real(tx_array), 1, atx*btx);
rc_apod_cos = real(rc_array);

%impulse_response = [1 0 0 0 0 0 0 0 0 0];    % 'true' impulse
load ir20mhz.mat;
impulse_repsonse = temp;

emit_cos = xdc_2d_array(btx, atx, wd, ht, krf, krf, tx_en_cos, 1, 1, focus);
[trash1, trash2, tx_apod_cos] = find(tx_apod_cos);
xdc_apodization(emit_cos, 0, tx_apod_cos);

%%%%  TRANSMITTED SIGNAL
t = (0:1/fs:tx_t);
excit_c = real(exp(j*2*pi*(fstart + (fstop-fstart)/(2*tx_t)*t).*t));
xdc_excitation(emit_cos, excit_c);


%%%%  TARGET PARAMETERS
% horizontal: linear phased array -- hang's -- between -15 and 15 degrees.
% vertical: doily array -- vang's -- between 5 and 25 degrees.
load myplatpts.mat
```

```
%x = x;
y = y + 4*sin(10/180*pi);
z = z + 4;
targetloc = [x, y, z];
[l,w] = size(targetloc);
targweights = ones([l,1]);
%%%%   FOCUSING DELAYS   %%%%
Ft = 4.0;                    % range for transmit and receive foci.
Fr1 = 3.0;
Fr2 = 3.3;
Fr3 = 3.65;
Fr4 = 4.0;
Fr5 = 4.6;
Fr6 = 5.2;
d = wd + krf;
nv = [0:atx-1]-atx/2;
nh = [0:brc-1]-brc/2;
delayst = Ft/c*(1-sqrt(1 + (nv*d/Ft).^2));
delaysr1 = Fr1/c*(1-sqrt(1 + (nh*d/Fr1).^2));
delaysr2 = Fr2/c*(1-sqrt(1 + (nh*d/Fr2).^2));
delaysr3 = Fr3/c*(1-sqrt(1 + (nh*d/Fr3).^2));
delaysr4 = Fr4/c*(1-sqrt(1 + (nh*d/Fr4).^2));
delaysr5 = Fr5/c*(1-sqrt(1 + (nh*d/Fr5).^2));
delaysr6 = Fr6/c*(1-sqrt(1 + (nh*d/Fr6).^2));

temp = [delayst; delayst]+.1;          % +.1 to keep elements with zero delay.
[trash1 trash2 delaystc] = find(temp.*tx_en_cos);
delaystc = delaystc.'-.1;
xdc_focus_times(emit_cos, 0, delaystc);
timesr = [0; 3.032/c; 3.325/c; 3.613/c; 4.095/c; 4.564/c];

%%%%  COLLECT DATA
istart = 0;
for(i=1:brc)
     i
    if (sum(abs(rc_en_cos(i,:))) ~= 0)
     clear delays
     dlys = (delayst+.1).*rc_en_cos(i,:);
     [trash1, trash2, dlys] = find(dlys);
     dlys = dlys-.1;
     delays = [dlys+delaysr1(i); dlys+delaysr2(i); dlys+delaysr3(i)];
     delays = [delays; dlys+delaysr4(i); dlys+delaysr5(i); dlys+delaysr6(i)];
     rc_en_c = rc;
     rc_en_c(i,:) = rc_en_cos(i,:);
     [trash1, trash2, rc_apod_c] = find(rc_apod_cos(i,:)');
```

```
      %%%  transmit on cosines, receive on cosines.
      rec_cos = xdc_2d_array(brc,arc,wd,ht,krf,krf,rc_en_c,1,1,focus);
      xdc_focus_times(rec_cos, timesr, delays);
      xdc_apodization(rec_cos, 0, rc_apod_c');
      [v, t1] = calc_scat(emit_cos,rec_cos,targetloc,targweights);
      imagedata(1:max(size(v)),i-istart) = v;
      times1(i-istart) = t1;
      xdc_free(rec_cos);
     end

%%%%% This commented part was for seeing the aperture I was making.
%      clear data data2 x y z c
%      data = xdc_get(rec_cos, 'rect');
%      data2 = xdc_get(rec_cos, 'apo');
%      [N1, M1] = size(data);
%      for(k=1:M1)
%         x = [data(11,k), data(20,k); data(14,k), data(17,k)]*1000;
%         y = [data(12,k), data(21,k); data(15,k), data(18,k)]*1000;
%         z = [data(13,k), data(22,k); data(16,k), data(19,k)]*1000;
%         c = data2(k+1)*ones(2,2);
%         figure(1)
%         hold on
%         h(k) = surf(x, y, z, c);
%         set(h(k), 'LineStyle', 'none');
%      end

end

xdc_free(emit_cos);

mintime = min(times1);
maxtime = max(times1);
min_sample = round(mintime*fs);
max_sample = round(maxtime*fs);
[n, m] = size(imagedata);
n = n+(max_sample - min_sample);
for(i=1:m)
   temp = [zeros(round(times1(i)*fs) - min_sample, 1); imagedata(:,i)];
   data(1:max(size(temp)),i) = temp;
end
clear imagedata
save tempcc.mat data mintime;
%save tempcc.mat imagedata times1;


%field_end;

toc;
```

APPENDIX C

RESOLUTION RESULTS WITH PROCESSING

Tables C.1–C.12 present resolution measurements for the high frequency two-dimensional amplitude-steered array without any time-frequency processing. The array is approximately 10 cm in diameter. There are 392 staves with a center-to-center spacing of 254 μm, and there are 466 rows with a center-to-center spacing of 215.9 μm. The array is designed to steer in the vertical direction to 5° at 5 MHz. Frequencies range from 1 MHz to 5 MHz. The center two staves are used as the transmit array.

Table C.1: Range resolution in mm for angles $5° - 14°$, horizontal angle $= 0°$.

Vertical Angle (deg) Range (m)	5	6	7	8	9	10	11	12	13	14
3.0	4.76	5.46	6.34	7.25	8.09	9.01	9.96	11.0	12.0	12.3
3.1	5.02	5.60	6.48	7.36	8.28	9.12	10.1	11.1	12.1	12.4
3.2	5.31	5.75	6.59	7.47	8.31	9.23	10.2	11.2	12.2	12.5
3.3	5.53	5.82	6.74	7.58	8.42	9.34	10.3	11.2	12.2	12.6
3.4	5.57	6.04	6.88	7.76	8.61	9.45	10.4	11.4	12.5	12.7
3.5	5.42	6.23	7.03	7.87	8.75	9.59	10.5	11.5	12.5	12.9
3.6	5.20	6.30	7.25	8.02	8.86	9.78	10.7	11.6	12.6	13.0
3.7	3.59	6.45	7.32	8.20	9.08	9.89	10.8	11.8	12.8	13.1
3.8	3.59	6.63	7.40	8.31	9.12	10.0	11.0	11.9	12.8	13.2
3.9	3.48	6.67	7.51	8.35	9.23	10.1	11.0	12.0	12.9	13.3
4.0	3.52	6.70	7.62	8.46	9.38	10.1	11.1	12.1	13.0	13.4
4.1	3.59	6.96	7.72	8.68	9.52	10.4	11.4	12.3	13.3	13.6
4.2	3.41	7.07	7.87	8.72	9.56	10.5	11.4	12.3	13.3	13.7
4.3	3.48	6.99	7.87	8.75	9.63	10.5	11.4	12.5	13.4	13.8
4.4	3.66	7.18	7.91	8.83	9.74	10.6	11.6	12.5	13.4	13.8
4.5	3.52	7.21	8.13	8.94	9.78	10.6	11.6	12.6	13.5	13.9
4.6	3.59	7.25	8.17	9.01	9.92	10.8	11.7	12.7	13.6	14.1
4.7	3.66	7.36	8.17	9.08	9.92	10.8	11.8	12.7	13.7	14.1
4.8	3.66	7.43	8.28	9.16	10.0	10.9	11.9	12.8	13.7	14.2
4.9	3.66	7.40	8.31	9.23	10.1	11.0	11.9	12.9	13.8	14.2
5.0	3.66	7.43	8.31	9.27	10.1	11.0	11.9	12.9	13.8	14.3

Table C.2: Range resolution in mm for angles 15° – 24°, horizontal angle = 0°.

Vertical Angle (deg) Range (m)	15	16	17	18	19	20	21	22	23	24
3.0	13.0	14.3	15.5	16.0	16.8	18.0	18.8	19.5	20.3	21.1
3.1	13.0	14.4	15.6	16.1	17.0	18.1	18.9	19.7	20.5	21.3
3.2	13.1	14.6	15.6	16.2	17.1	18.1	18.9	19.7	20.5	21.3
3.3	13.2	14.6	15.7	16.3	17.1	18.2	19.0	19.7	20.6	21.3
3.4	13.4	14.8	15.9	16.4	17.3	18.3	19.1	19.9	20.7	21.5
3.5	13.5	14.8	15.9	16.5	17.4	18.4	19.2	20.0	20.9	21.6
3.6	13.6	14.9	15.9	16.6	17.5	18.4	19.2	20.0	20.8	21.5
3.7	13.8	15.1	16.1	16.8	17.6	18.5	19.4	20.1	20.9	21.9
3.8	13.9	15.2	16.2	16.9	17.7	18.6	19.4	20.2	21.0	21.9
3.9	14.0	15.3	16.3	17.0	17.8	18.7	19.4	20.3	21.2	21.8
4.0	14.2	15.4	16.3	17.0	17.9	18.7	19.5	20.3	21.1	22.0
4.1	14.4	15.6	16.5	17.2	18.1	18.9	19.7	20.4	21.2	22.1
4.2	14.4	15.6	16.5	17.4	18.1	19.0	19.7	20.5	21.4	22.2
4.3	14.6	15.7	16.6	17.4	18.2	19.0	19.8	20.6	21.4	22.2
4.4	14.6	15.8	16.6	17.5	18.3	19.0	19.8	20.6	21.4	22.3
4.5	14.6	15.9	16.7	17.6	18.3	19.0	19.9	20.7	21.5	22.2
4.6	14.9	16.0	16.8	17.7	18.5	19.3	20.0	20.8	21.7	22.4
4.7	14.9	16.1	16.9	17.8	18.6	19.2	20.0	20.9	21.7	22.6
4.8	15.0	16.2	16.9	17.8	18.6	19.3	20.1	20.9	21.9	22.5
4.9	15.1	16.2	17.0	17.9	18.7	19.4	20.2	21.0	21.8	22.6
5.0	15.1	16.3	17.0	18.0	18.7	19.4	20.1	20.0	21.8	22.7

Table C.3: Range resolution in mm for angles $5° - 14°$, horizontal angle $= 15°$.

Vertical Angle (deg) Range (m)	5	6	7	8	9	10	11	12	13	14
3.0	4.65	5.42	6.30	7.18	8.06	8.90	9.81	10.7	11.6	12.1
3.1	5.05	5.60	6.48	7.36	8.20	9.01	9.89	10.8	11.6	12.1
3.2	5.24	5.75	6.67	7.54	8.42	9.27	10.1	11.0	11.8	12.4
3.3	5.57	5.93	6.81	7.73	8.68	9.59	10.6	11.4	12.2	12.8
3.4	5.57	6.23	7.07	7.95	8.90	9.81	10.8	11.5	12.2	12.6
3.5	5.42	6.30	7.25	8.17	9.12	10.0	11.1	12.3	12.5	12.9
3.6	5.46	6.41	7.32	8.35	9.30	10.2	11.5	12.7	14.3	13.1
3.7	5.13	6.59	7.51	8.46	9.45	10.5	11.6	12.9	14.1	13.0
3.8	3.59	6.67	7.62	8.57	9.56	10.7	11.9	13.2	14.7	13.3
3.9	3.63	6.81	7.69	8.68	9.70	10.8	12.1	13.6	15.0	16.0
4.0	3.63	6.96	7.76	8.83	9.81	10.9	12.3	13.8	15.3	16.5
4.1	3.63	6.92	7.80	8.72	9.78	10.8	12.0	13.5	14.9	15.9
4.2	3.66	7.14	8.06	9.01	10.0	11.1	12.4	13.9	15.3	16.1
4.3	3.70	7.29	8.13	9.16	10.1	11.2	12.5	14.0	15.6	16.6
4.4	3.66	7.32	8.28	9.23	10.3	11.3	12.7	14.2	15.8	17.0
4.5	3.74	7.40	8.31	9.27	10.4	11.5	12.8	14.3	16.0	17.8
4.6	3.81	7.54	8.42	9.41	10.4	11.5	12.9	14.3	15.7	16.7
4.7	3.77	7.51	8.50	9.52	10.6	11.6	12.9	14.4	16.0	17.3
4.8	3.77	7.54	8.50	9.56	10.6	11.7	13.1	14.5	16.1	18.0
4.9	3.85	7.69	8.57	9.63	10.7	11.8	13.2	14.6	16.3	18.2
5.0	3.88	7.69	8.68	9.67	10.8	11.9	13.3	14.7	16.5	18.4

Table C.4: Range resolution in mm for angles $15° - 24°$, horizontal angle $= 15°$.

Vertical Angle (deg) Range (m)	15	16	17	18	19	20	21	22	23	24
3.0	13.2	21.5	25.6	28.4	22.9	16.0	17.1	18.2	19.0	19.7
3.1	13.0	14.0	25.7	28.3	23.0	16.0	17.0	18.0	18.9	19.6
3.2	13.2	21.3	25.8	28.4	23.0	16.0	17.1	18.0	18.9	19.6
3.3	13.4	22.1	25.9	28.5	23.1	16.1	17.1	18.0	19.0	19.6
3.4	13.1	13.9	25.2	27.8	22.8	15.7	16.9	17.8	18.5	19.4
3.5	13.4	21.3	25.8	28.1	22.9	15.8	16.9	17.8	18.6	19.4
3.6	13.8	21.6	25.9	28.1	22.7	15.8	16.9	17.7	18.6	19.3
3.7	13.4	14.0	23.6	19.6	21.6	15.4	16.5	17.7	18.5	19.0
3.8	13.6	21.2	25.0	20.2	21.8	15.4	16.5	17.7	18.5	19.0
3.9	18.1	22.1	25.5	26.8	21.9	15.5	16.5	17.7	18.5	19.0
4.0	19.0	22.7	26.0	27.3	21.9	15.5	16.6	17.7	18.5	19.2
4.1	14.4	14.3	15.5	15.9	20.5	14.7	16.2	17.3	18.2	18.9
4.2	14.0	14.0	15.2	15.8	11.8	14.5	16.0	17.2	18.0	18.4
4.3	18.1	21.1	15.2	15.6	11.5	14.5	16.0	17.2	18.0	18.4
4.4	19.6	21.9	23.8	15.8	11.5	14.5	16.0	17.2	18.0	18.5
4.5	20.1	22.5	24.8	15.7	11.5	14.5	16.0	17.2	18.0	18.5
4.6	14.3	14.0	14.9	5.60	7.80	13.9	15.6	16.9	17.7	18.4
4.7	18.3	14.1	15.1	5.20	7.54	13.9	15.5	16.9	17.7	18.4
4.8	19.7	21.1	15.1	5.13	7.43	13.8	15.5	16.9	17.7	18.4
4.9	20.3	21.8	15.2	14.0	7.25	13.7	15.6	16.9	17.7	18.4
5.0	20.7	22.4	15.3	14.1	6.74	13.7	15.6	16.9	17.7	18.4

Table C.5: Vertical resolution in degrees for angles $5° - 14°$, horizontal angle $= 0°$.

Vertical Angle (deg) Range (m)	5	6	7	8	9	10	11	12	13	14
3.0	0.151	0.167	0.221	0.257	0.283	0.317	0.338	0.374	0.403	0.482
3.1	0.153	0.170	0.223	0.258	0.285	0.320	0.343	0.375	0.404	0.483
3.2	0.155	0.172	0.225	0.259	0.287	0.322	0.343	0.376	0.404	0.486
3.3	0.162	0.174	0.224	0.261	0.288	0.321	0.342	0.378	0.402	0.487
3.4	0.165	0.176	0.228	0.264	0.289	0.324	0.346	0.378	0.406	0.489
3.5	0.178	0.182	0.231	0.265	0.292	0.327	0.344	0.380	0.407	0.484
3.6	0.264	0.181	0.230	0.266	0.291	0.328	0.349	0.380	0.408	0.490
3.7	0.292	0.189	0.237	0.271	0.296	0.327	0.351	0.384	0.407	0.495
3.8	0.298	0.192	0.241	0.274	0.298	0.333	0.353	0.384	0.408	0.498
3.9	0.311	0.197	0.240	0.276	0.299	0.337	0.355	0.385	0.411	0.491
4.0	0.310	0.201	0.244	0.279	0.301	0.339	0.356	0.387	0.413	0.498
4.1	0.299	0.213	0.255	0.287	0.307	0.340	0.357	0.390	0.414	0.506
4.2	0.295	0.225	0.255	0.289	0.307	0.343	0.360	0.391	0.414	0.506
4.3	0.280	0.246	0.259	0.296	0.309	0.350	0.362	0.392	0.417	0.499
4.4	0.265	0.257	0.267	0.297	0.312	0.348	0.362	0.395	0.419	0.505
4.5	0.260	0.266	0.275	0.303	0.317	0.350	0.363	0.397	0.418	0.510
4.6	0.238	0.295	0.281	0.316	0.318	0.358	0.368	0.400	0.420	0.514
4.7	0.229	0.312	0.289	0.321	0.323	0.362	0.369	0.402	0.423	0.508
4.8	0.221	0.327	0.301	0.322	0.328	0.362	0.370	0.405	0.424	0.514
4.9	0.216	0.339	0.315	0.336	0.332	0.363	0.373	0.406	0.425	0.518
5.0	0.213	0.355	0.340	0.343	0.333	0.371	0.373	0.408	0.426	0.520

Table C.6: Vertical resolution in degrees for angles $15° - 24°$, horizontal angle $= 0°$.

Vertical Angle (deg) Range (m)	15	16	17	18	19	20	21	22	23	24
3.0	0.521	0.522	0.547	0.604	0.643	0.660	0.688	0.736	0.766	0.799
3.1	0.523	0.523	0.545	0.605	0.642	0.661	0.689	0.732	0.767	0.800
3.2	0.522	0.523	0.548	0.606	0.643	0.661	0.691	0.734	0.768	0.805
3.3	0.523	0.524	0.549	0.606	0.645	0.663	0.691	0.735	0.768	0.802
3.4	0.525	0.525	0.550	0.608	0.647	0.665	0.693	0.739	0.770	0.803
3.5	0.526	0.528	0.549	0.602	0.648	0.667	0.701	0.738	0.773	0.804
3.6	0.530	0.528	0.551	0.610	0.648	0.665	0.695	0.737	0.773	0.805
3.7	0.533	0.529	0.553	0.611	0.649	0.667	0.696	0.742	0.773	0.803
3.8	0.536	0.530	0.552	0.613	0.651	0.666	0.696	0.743	0.773	0.807
3.9	0.536	0.536	0.554	0.614	0.652	0.673	0.704	0.740	0.777	0.812
4.0	0.537	0.534	0.556	0.607	0.653	0.669	0.698	0.743	0.778	0.813
4.1	0.541	0.534	0.558	0.616	0.654	0.671	0.701	0.745	0.776	0.808
4.2	0.542	0.535	0.557	0.613	0.656	0.670	0.701	0.746	0.780	0.811
4.3	0.544	0.541	0.559	0.615	0.657	0.678	0.707	0.745	0.781	0.812
4.4	0.546	0.539	0.560	0.612	0.658	0.673	0.704	0.749	0.784	0.810
4.5	0.547	0.539	0.561	0.621	0.658	0.673	0.706	0.749	0.780	0.811
4.6	0.547	0.541	0.560	0.619	0.661	0.675	0.705	0.748	0.785	0.812
4.7	0.552	0.547	0.565	0.620	0.662	0.682	0.711	0.751	0.788	0.816
4.8	0.553	0.546	0.563	0.613	0.662	0.676	0.709	0.753	0.787	0.817
4.9	0.555	0.545	0.566	0.625	0.664	0.677	0.712	0.753	0.785	0.818
5.0	0.555	0.545	0.563	0.625	0.664	0.680	0.710	0.753	0.788	0.815

Table C.7: Vertical resolution in degrees for angles $5° - 14°$, horizontal angle $= 15°$.

Vertical Angle (deg) Range (m)	5	6	7	8	9	10	11	12	13	14
3.0	0.150	0.163	0.216	0.250	0.275	0.298	0.320	0.341	0.357	0.410
3.1	0.153	0.164	0.217	0.251	0.276	0.300	0.322	0.342	0.357	0.413
3.2	0.154	0.165	0.218	0.252	0.275	0.300	0.321	0.343	0.358	0.412
3.3	0.156	0.167	0.220	0.253	0.278	0.304	0.323	0.343	0.358	0.412
3.4	0.168	0.170	0.222	0.254	0.279	0.303	0.322	0.344	0.359	0.412
3.5	0.181	0.173	0.223	0.257	0.280	0.305	0.323	0.345	0.359	0.415
3.6	0.198	0.175	0.226	0.259	0.281	0.306	0.326	0.346	0.360	0.415
3.7	0.294	0.182	0.230	0.261	0.283	0.309	0.327	0.347	0.361	0.415
3.8	0.302	0.185	0.232	0.264	0.286	0.311	0.325	0.347	0.362	0.414
3.9	0.303	0.189	0.236	0.267	0.287	0.313	0.327	0.349	0.362	0.417
4.0	0.310	0.196	0.240	0.270	0.290	0.316	0.330	0.349	0.363	0.418
4.1	0.274	0.212	0.247	0.279	0.295	0.324	0.336	0.357	0.370	0.427
4.2	0.277	0.220	0.250	0.279	0.295	0.321	0.330	0.351	0.364	0.419
4.3	0.266	0.234	0.256	0.283	0.296	0.323	0.334	0.353	0.365	0.420
4.4	0.255	0.250	0.260	0.289	0.299	0.326	0.336	0.354	0.366	0.421
4.5	0.242	0.262	0.267	0.293	0.302	0.330	0.336	0.355	0.367	0.418
4.6	0.216	0.293	0.277	0.300	0.307	0.331	0.337	0.356	0.368	0.422
4.7	0.211	0.313	0.287	0.308	0.310	0.333	0.340	0.358	0.368	0.421
4.8	0.209	0.324	0.300	0.316	0.315	0.340	0.342	0.358	0.369	0.423
4.9	0.197	0.347	0.320	0.321	0.318	0.343	0.344	0.360	0.370	0.424
5.0	0.194	0.431	0.344	0.328	0.325	0.343	0.344	0.361	0.370	0.423

Table C.8: Vertical resolution in degrees for angles $15° - 24°$, horizontal angle $= 15°$.

Vertical Angle (deg) Range (m)	15	16	17	18	19	20	21	22	23	24
3.0	0.423	0.396	0.392	1.880	1.920	1.063	1.010	0.983	0.993	0.999
3.1	0.420	0.396	0.383	0.891	1.595	1.042	0.988	0.964	0.980	0.992
3.2	0.421	0.392	0.377	1.856	1.613	1.055	0.994	0.970	0.985	0.999
3.3	0.421	0.391	0.377	1.879	1.918	1.068	1.001	0.977	0.988	1.002
3.4	0.421	0.396	0.391	0.974	1.586	1.031	0.971	0.955	0.976	0.988
3.5	0.420	0.392	0.380	1.857	1.611	1.044	0.984	0.961	0.979	0.992
3.6	0.420	0.391	0.367	1.912	1.932	1.062	0.996	0.974	0.983	1.001
3.7	0.421	0.399	0.398	1.834	1.571	1.014	0.960	0.951	0.970	0.988
3.8	0.421	0.394	0.385	1.859	1.597	1.035	0.970	0.955	0.975	0.989
3.9	0.421	0.390	0.379	1.877	1.893	1.048	0.978	0.960	0.980	0.992
4.0	0.421	0.388	0.367	1.891	1.922	1.060	0.986	0.966	0.981	0.999
4.1	0.433	0.408	0.399	1.880	1.596	1.030	0.962	0.960	0.974	0.995
4.2	0.423	0.401	0.410	1.042	1.528	0.983	0.941	0.942	0.965	0.984
4.3	0.424	0.398	0.402	1.839	1.554	1.004	0.949	0.946	0.970	0.985
4.4	0.422	0.394	0.390	1.876	1.580	1.019	0.955	0.950	0.969	0.988
4.5	0.422	0.391	0.382	1.886	1.606	1.041	0.965	0.958	0.977	0.992
4.6	0.427	0.407	0.424	0.997	1.456	0.935	0.917	0.930	0.958	0.980
4.7	0.426	0.408	0.418	1.028	1.495	0.950	0.925	0.935	0.961	0.981
4.8	0.425	0.403	0.410	1.042	1.517	0.973	0.930	0.940	0.962	0.986
4.9	0.425	0.398	0.404	1.801	1.539	0.991	0.940	0.946	0.965	0.988
5.0	0.424	0.394	0.397	1.842	1.560	1.007	0.947	0.950	0.971	0.987

Table C.9: Horizontal resolution in degrees for angles $5° - 14°$, horizontal angle = $0°$.

Vertical Angle (deg) Range (m)	5	6	7	8	9	10	11	12	13	14
3.0	0.239	0.282	0.332	0.382	0.429	0.477	0.525	0.572	0.619	0.671
3.1	0.243	0.284	0.334	0.384	0.432	0.478	0.527	0.575	0.621	0.672
3.2	0.240	0.284	0.333	0.384	0.431	0.478	0.526	0.574	0.620	0.670
3.3	0.237	0.283	0.333	0.383	0.430	0.477	0.525	0.573	0.620	0.670
3.4	0.244	0.287	0.336	0.387	0.434	0.480	0.528	0.576	0.623	0.673
3.5	0.237	0.285	0.335	0.385	0.432	0.479	0.527	0.575	0.621	0.671
3.6	0.227	0.284	0.333	0.383	0.430	0.477	0.525	0.573	0.619	0.669
3.7	0.227	0.289	0.337	0.388	0.435	0.480	0.529	0.576	0.623	0.673
3.8	0.227	0.286	0.334	0.385	0.431	0.479	0.526	0.574	0.620	0.670
3.9	0.230	0.283	0.332	0.382	0.429	0.476	0.524	0.572	0.618	0.668
4.0	0.231	0.279	0.329	0.379	0.427	0.472	0.521	0.570	0.616	0.666
4.1	0.236	0.292	0.340	0.389	0.435	0.483	0.530	0.577	0.622	0.669
4.2	0.236	0.287	0.335	0.385	0.432	0.480	0.526	0.574	0.620	0.671
4.3	0.236	0.279	0.329	0.380	0.428	0.474	0.523	0.571	0.617	0.667
4.4	0.236	0.265	0.326	0.378	0.423	0.472	0.520	0.569	0.615	0.661
4.5	0.237	0.266	0.322	0.374	0.419	0.465	0.517	0.565	0.613	0.659
4.6	0.240	0.269	0.317	0.380	0.425	0.473	0.522	0.571	0.618	0.664
4.7	0.239	0.269	0.316	0.376	0.419	0.468	0.521	0.568	0.614	0.661
4.8	0.239	0.269	0.313	0.361	0.413	0.462	0.516	0.564	0.612	0.659
4.9	0.238	0.268	0.311	0.361	0.412	0.462	0.512	0.561	0.609	0.655
5.0	0.238	0.268	0.316	0.359	0.407	0.457	0.508	0.559	0.606	0.652

Table C.10: Horizontal resolution in degrees for angles 15°−24°, horizontal angle = 0°.

Vertical Angle (deg) Range (m)	15	16	17	18	19	20	21	22	23	24
3.0	0.710	0.761	0.810	0.858	0.907	0.944	0.983	1.034	1.082	1.117
3.1	0.712	0.764	0.813	0.860	0.910	0.946	0.985	1.035	1.085	1.120
3.2	0.711	0.763	0.810	0.858	0.909	0.944	0.983	1.033	1.083	1.117
3.3	0.709	0.761	0.809	0.857	0.908	0.944	0.981	1.032	1.081	1.115
3.4	0.713	0.764	0.813	0.860	0.912	0.948	0.981	1.035	1.084	1.119
3.5	0.710	0.763	0.811	0.858	0.911	0.945	0.981	1.033	1.081	1.115
3.6	0.708	0.761	0.809	0.857	0.909	0.943	0.979	1.030	1.079	1.113
3.7	0.711	0.764	0.811	0.857	0.913	0.946	0.980	1.032	1.083	1.116
3.8	0.709	0.761	0.809	0.858	0.907	0.945	0.979	1.030	1.082	1.114
3.9	0.707	0.759	0.808	0.856	0.905	0.943	0.976	1.029	1.078	1.110
4.0	0.704	0.757	0.806	0.851	0.907	0.941	0.974	1.027	1.079	1.109
4.1	0.712	0.764	0.808	0.855	0.908	0.947	0.978	1.029	1.085	1.109
4.2	0.708	0.761	0.809	0.856	0.907	0.946	0.977	1.030	1.083	1.111
4.3	0.705	0.759	0.809	0.852	0.906	0.942	0.974	1.027	1.081	1.110
4.4	0.702	0.757	0.804	0.850	0.903	0.940	0.972	1.026	1.080	1.106
4.5	0.700	0.753	0.802	0.849	0.902	0.939	0.970	1.025	1.078	1.104
4.6	0.706	0.760	0.808	0.853	0.907	0.944	0.974	1.028	1.083	1.109
4.7	0.702	0.758	0.805	0.851	0.904	0.941	0.972	1.026	1.082	1.107
4.8	0.699	0.755	0.802	0.849	0.904	0.941	0.970	1.024	1.079	1.105
4.9	0.696	0.751	0.801	0.847	0.901	0.940	0.968	1.023	1.077	1.103
5.0	0.694	0.750	0.799	0.844	0.900	0.936	0.966	1.021	1.076	1.102

Table C.11: Horizontal resolution in degrees for angles 5°−14°, horizontal angle = 15°.

Vertical Angle (deg) Range (m)	5	6	7	8	9	10	11	12	13	14
3.0	0.249	0.295	0.346	0.398	0.447	0.494	0.545	0.594	0.643	0.694
3.1	0.248	0.293	0.345	0.396	0.446	0.494	0.544	0.593	0.642	0.694
3.2	0.246	0.294	0.345	0.397	0.446	0.494	0.544	0.593	0.642	0.693
3.3	0.244	0.293	0.344	0.396	0.446	0.493	0.543	0.593	0.641	0.692
3.4	0.244	0.294	0.345	0.397	0.447	0.494	0.544	0.594	0.642	0.694
3.5	0.237	0.293	0.344	0.396	0.445	0.493	0.542	0.592	0.641	0.692
3.6	0.233	0.291	0.342	0.394	0.443	0.491	0.541	0.591	0.640	0.690
3.7	0.235	0.294	0.344	0.396	0.446	0.493	0.543	0.593	0.641	0.692
3.8	0.239	0.291	0.342	0.394	0.442	0.491	0.540	0.591	0.639	0.690
3.9	0.241	0.288	0.339	0.391	0.441	0.488	0.538	0.589	0.637	0.688
4.0	0.245	0.285	0.336	0.388	0.439	0.486	0.536	0.587	0.635	0.686
4.1	0.245	0.285	0.337	0.389	0.437	0.487	0.536	0.588	0.636	0.687
4.2	0.245	0.288	0.340	0.392	0.442	0.489	0.539	0.590	0.638	0.689
4.3	0.247	0.276	0.336	0.388	0.439	0.486	0.536	0.587	0.636	0.687
4.4	0.248	0.276	0.331	0.384	0.436	0.483	0.533	0.584	0.633	0.684
4.5	0.249	0.277	0.326	0.380	0.432	0.480	0.530	0.581	0.631	0.682
4.6	0.249	0.278	0.322	0.387	0.434	0.484	0.536	0.585	0.636	0.683
4.7	0.249	0.278	0.322	0.382	0.431	0.480	0.532	0.582	0.633	0.680
4.8	0.249	0.279	0.322	0.370	0.426	0.477	0.529	0.579	0.630	0.677
4.9	0.250	0.279	0.322	0.370	0.422	0.474	0.526	0.577	0.627	0.675
5.0	0.250	0.279	0.322	0.371	0.416	0.470	0.521	0.573	0.624	0.673

Table C.12: Horizontal resolution in degrees for angles 15° – 24°, horizontal angle = 15°.

Vertical Angle (deg) Range (m)	15	16	17	18	19	20	21	22	23	24
3.0	0.734	0.787	0.840	0.886	0.933	0.973	1.015	1.065	1.114	1.151
3.1	0.734	0.788	0.841	0.887	0.934	0.974	1.015	1.065	1.115	1.151
3.2	0.733	0.786	0.840	0.886	0.934	0.973	1.013	1.064	1.113	1.150
3.3	0.732	0.785	0.839	0.884	0.933	0.972	1.012	1.063	1.111	1.148
3.4	0.733	0.787	0.840	0.886	0.936	0.974	1.013	1.064	1.114	1.149
3.5	0.732	0.785	0.838	0.885	0.934	0.972	1.011	1.060	1.111	1.147
3.6	0.730	0.784	0.835	0.883	0.934	0.971	1.010	1.059	1.109	1.146
3.7	0.731	0.786	0.838	0.885	0.936	0.973	1.010	1.060	1.111	1.147
3.8	0.729	0.783	0.836	0.883	0.931	0.971	1.008	1.058	1.109	1.145
3.9	0.727	0.781	0.834	0.881	0.929	0.969	1.006	1.057	1.111	1.143
4.0	0.725	0.779	0.833	0.879	0.927	0.968	1.004	1.056	1.109	1.140
4.1	0.726	0.780	0.831	0.878	0.931	0.969	1.005	1.057	1.111	1.140
4.2	0.727	0.782	0.835	0.879	0.930	0.971	1.006	1.057	1.113	1.141
4.3	0.724	0.780	0.832	0.877	0.929	0.969	1.004	1.055	1.111	1.139
4.4	0.722	0.777	0.831	0.876	0.927	0.967	1.001	1.054	1.108	1.137
4.5	0.719	0.775	0.829	0.874	0.925	0.965	0.999	1.053	1.107	1.136
4.6	0.723	0.781	0.832	0.878	0.930	0.970	1.003	1.055	1.112	1.139
4.7	0.720	0.778	0.830	0.876	0.928	0.968	1.001	1.054	1.110	1.137
4.8	0.717	0.776	0.828	0.874	0.926	0.966	0.999	1.053	1.107	1.136
4.9	0.715	0.774	0.826	0.872	0.924	0.964	0.997	1.051	1.106	1.134
5.0	0.712	0.771	0.823	0.870	0.922	0.962	0.995	1.050	1.104	1.133

APPENDIX D

RESOLUTION RESULTS WITH PROCESSING

Tables D.1–D.16 present resolution measurements for the high frequency two-dimensional amplitude-steered array, first using the spectrogram and then using the smoothed pseudo-Wigner distribution (SPWD). Horizontal resolution is not expected to be affected by the processing, and so only range and vertical resolutions are given. The array is approximately 10 cm in diameter. There are 392 staves with a center-to-center spacing of 254 μm, and there are 466 rows with a center-to-center spacing of 215.9 μm. The array is designed to steer in the vertical direction to 5° at 5 MHz. Frequencies range from 1 MHz to 5 MHz. The center two staves are used as the transmit array.

Table D.1: Resolution results with spectrogram processing: range resolution in mm for angles $5° - 14°$, horizontal angle = $0°$.

Vertical Angle (deg) Range (m)	5	6	7	8	9	10	11	12	13	14
3.0	19.0	19.6	19.3	19.4	19.2	20.3	20.3	20.5	20.9	20.7
3.1	19.0	19.6	19.3	19.4	19.2	20.3	20.3	20.5	20.9	20.7
3.2	19.0	19.6	19.3	19.4	19.2	20.3	20.3	20.5	20.9	20.7
3.3	19.0	19.6	19.3	19.4	19.2	20.3	20.3	20.5	20.9	20.7
3.4	19.0	19.6	19.3	19.4	19.2	19.7	20.3	20.5	20.9	20.7
3.5	19.0	19.6	19.3	19.4	19.2	20.2	20.3	20.5	20.9	20.6
3.6	19.0	19.6	19.3	19.4	19.2	20.2	20.3	20.5	20.9	20.6
3.7	18.9	19.6	19.3	19.4	19.2	20.2	20.3	20.5	20.9	20.6
3.8	18.9	19.5	19.3	19.3	19.1	19.6	20.3	20.5	20.9	20.6
3.9	18.9	19.6	19.3	19.3	19.1	19.6	20.3	20.5	20.9	20.6
4.0	18.8	19.5	19.3	19.3	19.1	20.2	20.3	20.4	20.9	20.6
4.1	18.9	19.5	19.2	19.3	19.1	19.6	20.3	20.4	20.8	20.6
4.2	18.9	19.5	19.3	19.3	19.1	19.6	20.3	20.4	20.8	20.6
4.3	18.9	19.5	19.2	19.3	19.1	19.6	20.3	20.4	20.8	20.5
4.4	18.9	19.5	19.2	19.3	19.1	20.1	20.3	20.4	20.8	20.5
4.5	18.9	19.5	19.2	19.3	19.1	19.6	20.3	20.4	20.8	20.5
4.6	18.9	19.4	19.2	19.3	19.1	19.6	20.2	20.4	20.8	20.5
4.7	18.9	19.4	19.2	19.2	19.1	19.6	20.2	20.4	20.8	20.5
4.8	18.9	19.4	19.2	19.3	19.0	19.5	20.2	20.4	20.8	20.5
4.9	18.9	19.4	19.2	19.1	19.0	19.5	20.2	20.3	20.8	20.5
5.0	18.9	19.4	19.2	19.2	19.0	19.5	20.2	20.4	20.8	20.5

Table D.2: Resolution results with spectrogram processing: range resolution in mm for angles 15° – 24°, horizontal angle = 0°.

Vertical Angle (deg) Range (m)	15	16	17	18	19	20	21	22	23	24
3.0	20.9	21.8	22.8	23.0	23.0	24.0	24.4	24.9	25.6	26.6
3.1	20.9	21.7	22.7	23.0	23.0	24.0	24.5	24.9	25.6	26.6
3.2	20.9	21.8	22.7	23.0	23.0	24.0	24.4	24.9	25.6	26.6
3.3	20.9	21.7	22.7	23.0	23.0	24.0	24.4	24.9	25.6	26.6
3.4	20.9	21.7	22.7	23.0	23.0	24.0	24.4	24.9	25.6	26.6
3.5	20.9	21.7	22.7	23.0	23.0	23.9	24.4	24.9	25.6	26.6
3.6	20.9	21.7	22.7	23.0	23.0	24.0	24.4	24.9	25.6	26.6
3.7	20.9	21.7	22.7	23.0	23.0	24.0	24.4	24.9	25.6	26.6
3.8	20.9	21.7	22.7	23.0	23.0	24.0	24.4	24.9	25.6	26.6
3.9	20.9	21.6	22.7	23.0	23.0	24.0	24.4	24.9	25.6	26.6
4.0	20.9	21.7	22.7	23.0	23.0	23.9	24.4	24.9	25.6	26.6
4.1	20.8	21.7	22.6	23.0	23.0	24.0	24.4	24.9	25.6	26.6
4.2	20.8	21.6	22.6	22.9	23.0	24.0	24.4	24.9	25.6	26.6
4.3	20.8	21.6	22.6	22.9	23.0	23.9	24.4	24.9	25.6	26.6
4.4	20.8	21.6	22.6	22.9	23.0	23.9	24.4	24.9	25.6	26.6
4.5	20.8	21.6	22.6	22.9	23.0	23.9	24.4	24.9	25.6	26.6
4.6	20.8	21.6	22.6	22.9	23.0	23.9	24.4	24.9	25.6	26.6
4.7	20.8	21.6	22.6	22.9	23.0	23.9	24.4	24.9	25.6	26.6
4.8	20.8	21.6	22.6	22.9	23.0	23.9	24.4	24.9	25.6	26.6
4.9	20.8	21.6	22.6	22.9	23.0	23.9	24.4	24.8	25.6	26.6
5.0	20.8	21.6	22.6	22.8	22.9	23.9	24.4	24.9	25.6	26.6

Table D.3: Resolution results with spectrogram processing: range resolution in mm for angles $5° - 14°$, horizontal angle = $15°$.

Vertical Angle (deg) Range (m)	5	6	7	8	9	10	11	12	13	14
3.0	19.0	20.1	19.3	19.4	19.3	19.8	20.5	20.9	21.5	21.5
3.1	19.0	19.7	19.3	19.4	19.3	19.8	20.5	20.9	21.5	21.5
3.2	19.0	19.8	19.3	19.4	19.2	19.8	20.5	20.9	21.5	21.6
3.3	19.0	20.0	19.3	19.4	19.2	19.8	20.5	20.9	21.5	21.5
3.4	19.0	19.5	19.3	19.4	19.2	19.8	20.5	20.9	21.5	21.6
3.5	19.0	19.6	19.3	19.3	19.2	19.8	20.5	20.9	21.5	21.6
3.6	19.0	19.9	19.3	19.4	19.2	19.8	20.5	20.9	21.5	21.5
3.7	19.0	19.3	19.3	19.4	19.2	19.8	20.5	20.9	21.5	21.5
3.8	18.9	19.6	19.3	19.3	19.2	19.7	20.5	20.8	21.5	21.5
3.9	18.9	19.8	19.3	19.3	19.2	19.7	20.5	20.9	21.5	21.5
4.0	18.9	19.6	19.3	19.3	19.2	19.7	20.5	20.8	21.5	21.5
4.1	18.9	19.4	19.2	19.2	19.2	19.7	20.4	20.8	21.4	21.4
4.2	18.9	19.4	19.2	19.2	19.2	19.7	20.5	20.8	21.5	21.5
4.3	18.9	19.4	19.2	19.2	19.2	19.7	20.4	20.8	21.5	21.5
4.4	18.9	19.5	19.2	19.2	19.2	19.7	20.4	20.8	21.5	21.5
4.5	18.9	19.5	19.2	19.2	19.2	19.7	20.4	20.8	21.5	21.5
4.6	18.9	19.3	19.2	19.2	19.2	19.7	20.4	20.8	21.4	21.5
4.7	19.0	19.4	19.2	19.2	19.1	19.7	20.4	20.8	21.4	21.5
4.8	19.0	19.4	19.2	19.2	19.1	19.6	20.4	20.8	21.4	21.5
4.9	19.0	19.4	19.2	19.2	19.1	19.6	20.4	20.8	21.4	21.5
5.0	18.9	19.6	19.2	19.2	19.1	19.6	20.4	20.8	21.4	21.5

Table D.4: Resolution results with spectrogram processing: range resolution in mm for angles $15° - 24°$, horizontal angle = 15°.

Vertical Angle (deg) Range (m)	15	16	17	18	19	20	21	22	23	24
3.0	22.4	24.7	25.5	37.0	16.6	19.7	20.8	21.6	22.9	24.3
3.1	22.4	24.5	23.8	22.8	17.8	20.2	21.1	21.7	22.9	24.3
3.2	22.4	24.6	27.2	31.7	17.1	20.1	20.9	21.6	22.9	24.3
3.3	22.4	24.8	26.4	17.9	16.8	19.9	20.9	21.6	22.9	24.3
3.4	22.4	24.4	23.4	22.2	19.3	20.6	21.2	21.8	23.0	24.3
3.5	22.4	24.6	24.0	31.7	18.6	20.4	21.1	21.7	23.0	24.3
3.6	22.5	24.7	26.0	18.2	18.2	20.3	21.1	21.7	22.9	24.2
3.7	22.4	24.4	23.4	21.7	20.2	20.8	21.4	21.8	23.0	24.3
3.8	22.4	24.6	23.6	21.8	19.6	20.7	21.2	21.8	23.0	24.3
3.9	22.5	24.7	23.9	29.0	19.1	20.5	21.2	21.7	22.9	24.2
4.0	22.5	24.9	24.6	18.6	18.6	20.4	21.1	21.7	22.9	24.2
4.1	22.2	24.1	24.2	21.7	20.5	20.9	21.4	21.8	23.0	24.2
4.2	22.4	24.3	23.5	21.5	20.9	21.2	21.5	21.9	23.0	24.3
4.3	22.4	24.4	23.5	21.4	20.7	21.1	21.5	21.9	23.0	24.2
4.4	22.5	24.6	23.6	21.4	20.4	20.9	21.4	21.9	23.0	24.2
4.5	22.5	24.7	23.7	21.3	20.1	20.8	21.3	21.8	23.0	24.2
4.6	22.4	24.1	23.5	21.5	21.5	21.5	21.7	22.0	23.1	24.2
4.7	22.4	24.2	23.5	21.5	21.3	21.4	21.7	22.0	23.0	24.2
4.8	22.4	24.4	23.5	21.3	21.1	21.3	21.6	22.0	23.0	24.2
4.9	22.5	24.5	23.6	21.2	20.9	21.2	21.6	21.9	23.0	24.2
5.0	22.5	24.6	23.6	21.2	20.8	21.1	21.5	21.9	23.0	24.1

Table D.5: Resolution results with spectrogram processing: vertical resolution in degrees for angles $5° - 14°$, horizontal hngle $= 0°$.

Vertical Angle (deg) Range (m)	5	6	7	8	9	10	11	12	13	14
3.0	0.153	0.182	0.230	0.270	0.305	0.344	0.373	0.415	0.447	0.508
3.1	0.156	0.184	0.232	0.271	0.306	0.344	0.374	0.415	0.448	0.509
3.2	0.160	0.186	0.233	0.272	0.306	0.345	0.374	0.415	0.449	0.510
3.3	0.165	0.187	0.233	0.273	0.308	0.346	0.375	0.416	0.449	0.510
3.4	0.169	0.190	0.237	0.275	0.309	0.348	0.377	0.416	0.450	0.510
3.5	0.183	0.193	0.239	0.276	0.310	0.349	0.377	0.416	0.450	0.511
3.6	0.264	0.195	0.239	0.277	0.311	0.350	0.378	0.418	0.452	0.511
3.7	0.290	0.200	0.244	0.280	0.313	0.352	0.380	0.419	0.452	0.512
3.8	0.296	0.205	0.248	0.282	0.315	0.354	0.381	0.419	0.452	0.513
3.9	0.311	0.209	0.248	0.284	0.316	0.355	0.382	0.420	0.454	0.513
4.0	0.309	0.213	0.252	0.286	0.318	0.357	0.383	0.421	0.455	0.514
4.1	0.298	0.223	0.260	0.290	0.321	0.362	0.385	0.422	0.456	0.515
4.2	0.294	0.232	0.261	0.292	0.323	0.361	0.387	0.423	0.456	0.516
4.3	0.281	0.244	0.264	0.297	0.326	0.365	0.389	0.424	0.458	0.517
4.4	0.266	0.255	0.272	0.298	0.327	0.366	0.389	0.425	0.459	0.517
4.5	0.262	0.263	0.278	0.301	0.330	0.369	0.391	0.427	0.459	0.519
4.6	0.241	0.292	0.284	0.310	0.334	0.371	0.394	0.427	0.460	0.520
4.7	0.233	0.311	0.290	0.313	0.338	0.375	0.395	0.428	0.463	0.521
4.8	0.228	0.327	0.300	0.314	0.340	0.378	0.397	0.431	0.463	0.521
4.9	0.221	0.344	0.311	0.323	0.342	0.378	0.399	0.432	0.463	0.523
5.0	0.218	0.366	0.321	0.329	0.346	0.381	0.400	0.432	0.465	0.525

Table D.6: Resolution results with spectrogram processing: vertical resolution in degrees for angles $15° - 24°$, horizontal angle = $0°$.

Vertical Angle (deg) Range (m)	15	16	17	18	19	20	21	22	23	24
3.0	0.564	0.586	0.695	0.747	0.760	0.851	0.885	0.964	1.030	1.124
3.1	0.565	0.586	0.694	0.746	0.759	0.849	0.884	0.963	1.029	1.122
3.2	0.565	0.585	0.695	0.745	0.758	0.850	0.884	0.963	1.028	1.120
3.3	0.565	0.585	0.694	0.745	0.758	0.851	0.884	0.962	1.028	1.119
3.4	0.565	0.585	0.691	0.745	0.758	0.850	0.882	0.961	1.026	1.117
3.5	0.566	0.586	0.691	0.744	0.757	0.847	0.882	0.960	1.026	1.115
3.6	0.566	0.586	0.694	0.744	0.757	0.849	0.882	0.959	1.025	1.115
3.7	0.566	0.585	0.693	0.743	0.756	0.850	0.881	0.958	1.024	1.111
3.8	0.567	0.586	0.689	0.743	0.756	0.845	0.880	0.957	1.023	1.110
3.9	0.567	0.586	0.690	0.742	0.756	0.846	0.880	0.957	1.022	1.109
4.0	0.567	0.586	0.694	0.742	0.755	0.849	0.880	0.956	1.022	1.108
4.1	0.567	0.585	0.687	0.743	0.755	0.847	0.880	0.954	1.021	1.105
4.2	0.568	0.587	0.687	0.740	0.754	0.844	0.878	0.954	1.020	1.103
4.3	0.569	0.587	0.691	0.741	0.754	0.846	0.878	0.953	1.019	1.102
4.4	0.570	0.587	0.690	0.740	0.754	0.846	0.878	0.953	1.019	1.101
4.5	0.570	0.588	0.687	0.739	0.754	0.843	0.877	0.953	1.018	1.100
4.6	0.571	0.587	0.688	0.739	0.752	0.844	0.876	0.951	1.016	1.098
4.7	0.572	0.588	0.689	0.739	0.753	0.845	0.876	0.950	1.016	1.097
4.8	0.572	0.588	0.687	0.738	0.752	0.842	0.875	0.950	1.016	1.096
4.9	0.573	0.589	0.688	0.738	0.753	0.843	0.875	0.950	1.015	1.095
5.0	0.574	0.589	0.688	0.738	0.752	0.845	0.875	0.948	1.015	1.094

Table D.7: Resolution results with spectrogram processing: vertical resolution in degrees for angles $5° - 14°$, horizontal angle $= 15°$.

Vertical Angle (deg) Range (m)	5	6	7	8	9	10	11	12	13	14
3.0	0.152	0.119	0.226	0.265	0.295	0.327	0.354	0.390	0.413	0.444
3.1	0.155	0.131	0.227	0.266	0.295	0.328	0.355	0.390	0.412	0.445
3.2	0.158	0.129	0.228	0.267	0.295	0.328	0.355	0.390	0.412	0.443
3.3	0.160	0.126	0.229	0.267	0.296	0.329	0.355	0.390	0.413	0.442
3.4	0.172	0.141	0.231	0.268	0.297	0.330	0.356	0.391	0.412	0.443
3.5	0.184	0.137	0.233	0.270	0.298	0.331	0.357	0.391	0.412	0.441
3.6	0.199	0.131	0.235	0.272	0.299	0.332	0.357	0.391	0.411	0.440
3.7	0.293	0.151	0.238	0.273	0.300	0.333	0.358	0.391	0.412	0.441
3.8	0.301	0.144	0.240	0.275	0.302	0.334	0.359	0.391	0.412	0.439
3.9	0.303	0.138	0.243	0.277	0.303	0.335	0.359	0.391	0.411	0.438
4.0	0.309	0.134	0.246	0.279	0.304	0.337	0.360	0.391	0.411	0.436
4.1	0.293	0.159	0.253	0.285	0.310	0.343	0.367	0.396	0.419	0.447
4.2	0.277	0.151	0.255	0.285	0.308	0.340	0.363	0.392	0.412	0.439
4.3	0.266	0.147	0.260	0.287	0.310	0.342	0.364	0.392	0.411	0.437
4.4	0.256	0.148	0.265	0.291	0.312	0.343	0.365	0.393	0.411	0.435
4.5	0.246	0.141	0.270	0.294	0.314	0.345	0.366	0.393	0.411	0.433
4.6	0.222	0.159	0.278	0.298	0.317	0.347	0.367	0.394	0.412	0.438
4.7	0.217	0.153	0.285	0.302	0.320	0.349	0.369	0.394	0.411	0.436
4.8	0.214	0.148	0.296	0.307	0.322	0.351	0.370	0.394	0.411	0.435
4.9	0.205	0.149	0.304	0.310	0.325	0.353	0.371	0.394	0.411	0.433
5.0	0.200	0.137	0.318	0.315	0.328	0.355	0.372	0.395	0.411	0.432

Table D.8: Resolution results with spectrogram processing: vertical resolution in degrees for angles $15° - 24°$, horizontal angle = $15°$.

Vertical Angle (deg) Range (m)	15	16	17	18	19	20	21	22	23	24
3.0	0.472	0.492	0.614	0.897	1.061	0.973	0.955	1.037	1.065	1.186
3.1	0.477	0.504	0.682	1.488	1.056	0.966	0.958	1.046	1.067	1.188
3.2	0.472	0.496	0.700	0.713	1.101	0.977	0.963	1.048	1.069	1.189
3.3	0.468	0.489	0.699	0.761	1.126	0.986	0.968	1.049	1.071	1.190
3.4	0.475	0.508	0.611	0.477	1.079	0.982	0.971	1.058	1.074	1.191
3.5	0.470	0.500	0.657	0.940	1.133	0.995	0.977	1.061	1.076	1.193
3.6	0.466	0.490	0.650	0.667	1.179	1.016	0.986	1.061	1.081	1.198
3.7	0.474	0.512	0.579	0.562	1.113	1.001	0.985	1.069	1.082	1.195
3.8	0.469	0.504	0.601	1.195	1.167	1.016	0.991	1.072	1.084	1.196
3.9	0.464	0.497	0.637	1.000	1.219	1.027	0.996	1.075	1.086	1.198
4.0	0.460	0.491	1.235	0.691	1.305	1.035	1.001	1.077	1.088	1.198
4.1	0.476	0.510	0.588	0.607	1.292	1.046	1.008	1.078	1.094	1.207
4.2	0.471	0.517	0.566	0.676	1.177	1.032	1.005	1.085	1.093	1.202
4.3	0.466	0.511	0.568	0.669	1.249	1.042	1.011	1.087	1.095	1.203
4.4	0.462	0.505	0.575	1.218	1.323	1.055	1.016	1.090	1.097	1.204
4.5	0.459	0.500	0.590	1.399	1.401	1.069	1.021	1.093	1.098	1.204
4.6	0.472	0.527	0.584	0.736	1.163	1.041	1.016	1.094	1.100	1.207
4.7	0.468	0.522	0.578	0.742	1.219	1.052	1.022	1.096	1.102	1.208
4.8	0.464	0.516	0.573	0.749	1.274	1.067	1.027	1.099	1.104	1.208
4.9	0.461	0.511	0.569	0.753	1.330	1.076	1.032	1.102	1.106	1.209
5.0	0.457	0.503	0.568	0.757	1.389	1.086	1.037	1.104	1.107	1.210

Table D.9: Resolution results with SPWD processing: range resolution in mm for angles $5° - 14°$, horizontal angle $= 0°$.

Vertical Angle (deg) Range (m)	5	6	7	8	9	10	11	12	13	14
3.0	7.40	8.64	8.28	8.72	9.41	10.3	11.1	11.8	12.6	12.5
3.1	7.32	8.64	8.28	8.68	9.41	10.3	11.1	11.8	12.6	12.5
3.2	7.36	8.61	8.24	8.68	9.38	10.2	11.1	11.7	12.6	12.5
3.3	7.25	8.61	8.24	8.68	9.37	10.2	11.1	11.7	12.6	12.4
3.4	7.25	8.57	8.17	8.64	9.30	10.2	11.1	11.7	12.6	12.4
3.5	7.18	8.53	8.17	8.64	9.34	10.2	11.1	11.7	12.6	12.4
3.6	7.03	8.53	8.17	8.64	9.30	10.2	11.0	11.6	12.5	12.4
3.7	6.92	8.46	8.06	8.57	9.23	10.1	11.0	11.6	12.5	12.3
3.8	6.88	8.46	8.06	8.53	9.19	10.1	11.0	11.6	12.5	12.3
3.9	6.45	8.39	8.06	8.50	9.19	10.1	10.9	11.6	12.5	12.3
4.0	6.12	8.39	8.02	8.50	9.16	10.0	10.9	11.9	12.5	12.3
4.1	6.26	8.31	7.91	8.42	9.01	10.0	10.9	11.8	12.4	12.2
4.2	6.63	8.28	7.91	8.42	9.08	9.96	10.8	11.8	12.4	12.2
4.3	6.70	8.20	7.87	8.35	9.05	9.92	10.8	11.8	12.4	12.2
4.4	6.63	8.17	7.80	8.31	9.01	9.89	10.8	11.8	12.3	12.2
4.5	6.77	8.13	7.51	8.35	8.90	9.85	10.7	11.7	12.3	12.2
4.6	6.88	8.06	7.47	8.20	8.94	9.81	10.7	11.7	12.3	12.1
4.7	6.88	8.02	7.43	8.20	8.90	9.78	10.7	11.6	12.3	12.1
4.8	6.92	7.95	7.40	8.20	8.79	9.74	10.6	11.6	12.2	12.1
4.9	6.92	7.91	7.36	8.13	8.75	9.74	10.6	11.6	12.2	12.0
5.0	6.96	7.80	7.32	8.06	8.79	9.70	10.6	11.6	12.2	12.0

Table D.10: Resolution results with SPWD processing: range resolution in mm for angles $15° - 24°$, horizontal angle $= 0°$.

Vertical Angle (deg) Range (m)	15	16	17	18	19	20	21	22	23	24
3.0	13.0	14.4	15.5	15.9	16.6	17.7	18.6	19.2	20.2	20.7
3.1	13.0	14.4	15.5	15.8	16.5	17.7	18.6	19.2	20.1	20.7
3.2	13.0	14.4	15.5	15.8	16.6	17.7	18.6	19.2	20.2	20.7
3.3	13.0	14.4	15.5	15.8	16.5	17.7	18.6	19.2	20.1	20.7
3.4	13.0	14.3	15.5	15.8	16.5	17.7	18.5	19.2	20.1	20.7
3.5	12.9	14.4	15.5	15.8	16.5	17.7	18.5	19.2	20.1	20.7
3.6	13.0	14.3	15.4	15.7	16.5	17.7	18.5	19.1	20.1	20.7
3.7	12.9	14.3	15.3	15.7	16.4	17.7	18.5	19.1	20.1	20.6
3.8	12.9	14.3	15.4	15.7	16.4	17.7	18.5	19.1	20.1	20.6
3.9	12.9	14.3	15.4	15.7	16.4	17.6	18.5	19.1	20.1	20.6
4.0	12.9	14.2	15.3	15.7	16.4	17.6	18.5	19.1	20.1	20.6
4.1	12.8	14.2	15.3	15.7	16.4	17.6	18.5	19.0	20.1	20.6
4.2	12.8	14.2	15.3	15.7	16.4	17.6	18.5	19.0	20.0	20.6
4.3	12.8	14.2	15.3	15.6	16.4	17.5	18.5	19.0	20.0	20.5
4.4	12.7	14.2	15.2	15.6	16.4	17.5	18.4	19.0	20.0	20.5
4.5	12.7	14.1	15.3	15.6	16.3	17.5	18.4	19.0	20.0	20.5
4.6	12.7	14.1	15.2	15.6	16.3	17.5	18.4	19.0	20.0	20.5
4.7	12.7	14.1	15.2	15.5	16.3	17.5	18.3	19.0	20.0	20.5
4.8	12.7	14.1	15.2	15.6	16.3	17.5	18.3	19.0	20.0	20.5
4.9	12.6	14.1	15.2	15.5	16.3	17.5	18.3	19.0	20.0	20.5
5.0	12.6	14.1	15.2	15.5	16.3	17.4	18.3	19.0	19.9	20.5

Table D.11: Resolution results with SPWD processing: range resolution in mm for angles $5° - 14°$, horizontal angle $= 15°$.

Vertical Angle (deg) Range (m)	5	6	7	8	9	10	11	12	13	14
3.0	7.36	10.4	8.35	8.86	9.52	10.6	11.7	12.9	14.0	14.2
3.1	7.40	9.67	8.35	8.86	9.52	10.6	11.7	12.8	13.8	14.2
3.2	7.40	9.92	8.31	8.83	9.52	10.6	11.6	12.8	14.0	14.2
3.3	7.36	10.1	8.02	8.83	9.52	10.6	11.6	12.8	14.0	14.2
3.4	7.25	9.34	7.98	8.79	9.45	10.6	11.6	12.8	13.8	14.2
3.5	7.14	9.52	7.98	8.79	9.45	10.6	11.6	12.7	13.9	14.2
3.6	7.10	9.89	7.95	8.75	9.41	10.5	11.6	12.7	14.0	14.2
3.7	6.96	8.83	7.87	8.72	9.37	10.5	11.5	12.7	13.9	14.2
3.8	6.70	9.23	7.87	8.68	9.37	10.5	11.5	12.7	13.8	14.2
3.9	6.52	9.56	7.84	8.64	9.34	10.4	11.5	12.7	13.9	14.2
4.0	6.12	9.70	7.80	8.64	9.30	10.4	11.5	12.7	13.8	14.2
4.1	6.26	8.57	7.73	8.53	9.23	10.3	11.4	12.5	13.6	13.9
4.2	6.70	8.75	7.73	8.53	9.23	10.4	11.4	12.6	13.8	14.2
4.3	6.77	8.90	7.69	8.53	9.23	10.3	11.4	12.6	13.8	14.2
4.4	6.81	9.23	7.62	8.46	9.19	10.3	11.4	12.6	13.8	14.2
4.5	6.85	9.37	7.62	8.42	9.12	10.3	11.3	12.6	13.7	14.2
4.6	6.99	8.20	7.54	8.39	9.08	10.3	11.3	12.5	13.7	14.1
4.7	6.99	8.90	7.51	8.35	9.05	10.2	11.3	12.5	13.7	14.1
4.8	6.99	8.97	7.43	8.31	9.01	10.2	11.2	12.5	13.7	14.1
4.9	7.14	8.90	7.40	8.28	9.01	10.1	11.2	12.5	13.7	14.1
5.0	7.14	9.52	7.36	8.24	8.94	10.1	11.2	12.4	13.7	14.1

Table D.12: Resolution results with SPWD processing: range resolution in mm for angles $15° - 24°$, horizontal angle $= 15°$.

Vertical Angle (deg) Range (m)	15	16	17	18	19	20	21	22	23	24
3.0	15.7	19.0	18.9	64.6	15.8	12.3	13.8	15.9	16.7	17.2
3.1	15.8	18.7	20.4	18.9	13.9	12.5	14.0	16.0	16.8	17.3
3.2	15.8	18.9	21.0	16.0	14.7	12.7	14.0	15.9	16.7	17.2
3.3	15.8	19.1	19.5	62.7	15.0	12.3	13.8	15.9	16.7	17.2
3.4	15.8	18.7	20.5	20.0	9.37	13.0	14.2	16.0	16.8	17.3
3.5	15.8	18.9	20.8	20.8	8.90	12.8	14.0	15.9	16.7	17.3
3.6	15.9	19.0	21.9	20.3	8.68	12.6	13.9	15.9	16.7	17.2
3.7	15.8	18.6	20.7	18.4	9.92	13.3	14.2	16.0	16.8	17.3
3.8	15.8	18.9	20.9	28.6	9.41	13.1	14.1	15.9	16.7	17.3
3.9	15.9	19.1	21.2	18.9	8.97	12.9	14.1	15.9	16.7	17.2
4.0	15.9	19.3	21.5	19.6	8.61	12.7	14.0	15.8	16.7	17.2
4.1	15.4	18.3	20.7	16.7	9.81	13.3	14.2	15.9	16.7	17.3
4.2	15.7	18.5	15.1	8.94	11.1	13.7	14.4	16.0	16.8	17.3
4.3	15.8	18.7	21.1	9.08	10.5	13.5	14.3	16.0	16.7	17.3
4.4	15.8	18.9	21.3	9.19	9.96	13.3	14.2	15.9	16.7	17.2
4.5	15.9	19.1	21.6	9.41	9.52	13.1	14.1	15.8	16.6	17.2
4.6	15.6	18.2	20.1	15.6	12.3	14.0	14.6	16.1	16.8	17.4
4.7	15.7	18.4	20.4	20.7	11.9	13.9	14.5	16.0	16.8	17.3
4.8	15.7	18.6	20.7	8.64	11.5	13.7	14.5	16.0	16.7	17.3
4.9	15.8	18.7	21.1	8.75	11.0	13.6	14.4	15.9	16.7	17.2
5.0	15.8	18.9	21.4	8.83	10.6	13.5	14.3	15.8	16.7	17.2

Table D.13: Resolution results with SPWD processing: vertical resolution in degrees for angles $5° - 14°$, horizontal angle = $0°$.

Vertical Angle (deg) Range (m)	5	6	7	8	9	10	11	12	13	14
3.0	0.147	0.184	0.220	0.252	0.286	0.318	0.351	0.384	0.414	0.469
3.1	0.149	0.184	0.221	0.252	0.285	0.317	0.350	0.382	0.412	0.468
3.2	0.150	0.185	0.221	0.252	0.285	0.317	0.348	0.381	0.411	0.468
3.3	0.153	0.185	0.220	0.251	0.284	0.316	0.348	0.381	0.411	0.466
3.4	0.153	0.186	0.222	0.251	0.284	0.316	0.347	0.378	0.408	0.464
3.5	0.160	0.186	0.222	0.251	0.283	0.314	0.345	0.376	0.407	0.462
3.6	0.177	0.186	0.219	0.250	0.281	0.312	0.344	0.376	0.406	0.461
3.7	0.267	0.189	0.221	0.250	0.280	0.312	0.343	0.374	0.403	0.459
3.8	0.276	0.190	0.223	0.250	0.281	0.311	0.341	0.372	0.402	0.458
3.9	0.288	0.190	0.221	0.250	0.280	0.310	0.341	0.370	0.401	0.455
4.0	0.283	0.192	0.222	0.250	0.278	0.310	0.340	0.370	0.400	0.454
4.1	0.270	0.195	0.224	0.249	0.279	0.307	0.335	0.365	0.396	0.452
4.2	0.269	0.196	0.222	0.249	0.278	0.306	0.336	0.365	0.396	0.450
4.3	0.260	0.201	0.224	0.251	0.277	0.307	0.336	0.364	0.394	0.448
4.4	0.249	0.204	0.225	0.249	0.276	0.305	0.333	0.363	0.394	0.448
4.5	0.249	0.203	0.227	0.249	0.278	0.305	0.333	0.363	0.392	0.447
4.6	0.236	0.212	0.227	0.251	0.275	0.303	0.332	0.360	0.390	0.444
4.7	0.230	0.225	0.230	0.251	0.276	0.303	0.330	0.358	0.389	0.443
4.8	0.226	0.226	0.232	0.250	0.276	0.302	0.329	0.358	0.388	0.441
4.9	0.221	0.235	0.235	0.251	0.276	0.302	0.330	0.358	0.386	0.441
5.0	0.218	0.255	0.237	0.255	0.276	0.302	0.329	0.356	0.386	0.440

Table D.14: Resolution results with SPWD processing: vertical resolution in degrees for angles $15° - 24°$, horizontal angle $= 0°$.

Vertical Angle (deg) Range (m)	15	16	17	18	19	20	21	22	23	24
3.0	0.516	0.539	0.568	0.626	0.684	0.717	0.766	0.826	0.873	0.934
3.1	0.515	0.537	0.567	0.624	0.681	0.714	0.762	0.823	0.869	0.930
3.2	0.514	0.535	0.567	0.622	0.679	0.714	0.761	0.821	0.866	0.928
3.3	0.512	0.534	0.566	0.620	0.678	0.712	0.759	0.819	0.864	0.926
3.4	0.509	0.531	0.562	0.617	0.674	0.708	0.755	0.815	0.859	0.922
3.5	0.507	0.530	0.560	0.615	0.672	0.706	0.753	0.813	0.856	0.920
3.6	0.505	0.528	0.560	0.613	0.670	0.706	0.752	0.811	0.854	0.918
3.7	0.503	0.525	0.558	0.610	0.666	0.703	0.747	0.808	0.848	0.913
3.8	0.502	0.523	0.555	0.608	0.664	0.699	0.746	0.806	0.846	0.911
3.9	0.499	0.522	0.554	0.606	0.662	0.697	0.744	0.803	0.844	0.909
4.0	0.498	0.520	0.554	0.604	0.660	0.698	0.741	0.802	0.841	0.907
4.1	0.493	0.514	0.550	0.599	0.653	0.692	0.737	0.797	0.835	0.903
4.2	0.493	0.515	0.548	0.598	0.653	0.689	0.735	0.795	0.832	0.900
4.3	0.491	0.513	0.547	0.596	0.651	0.689	0.733	0.793	0.830	0.898
4.4	0.490	0.511	0.546	0.595	0.648	0.689	0.731	0.791	0.828	0.896
4.5	0.489	0.510	0.545	0.593	0.647	0.686	0.729	0.790	0.826	0.894
4.6	0.486	0.506	0.542	0.589	0.642	0.682	0.725	0.785	0.820	0.890
4.7	0.484	0.504	0.540	0.588	0.640	0.682	0.724	0.783	0.818	0.888
4.8	0.484	0.503	0.540	0.587	0.638	0.679	0.722	0.783	0.816	0.887
4.9	0.483	0.503	0.539	0.584	0.637	0.678	0.720	0.781	0.814	0.885
5.0	0.481	0.500	0.537	0.583	0.635	0.678	0.719	0.779	0.812	0.883

Table D.15: Resolution results with SPWD processing: vertical resolution in degrees for angles $5° - 14°$, horizontal angle $= 15°$.

Vertical Angle (deg) Range (m)	5	6	7	8	9	10	11	12	13	14
3.0	0.147	0.104	0.217	0.246	0.276	0.304	0.331	0.357	0.386	0.419
3.1	0.148	0.112	0.217	0.245	0.276	0.304	0.331	0.357	0.388	0.421
3.2	0.148	0.113	0.217	0.245	0.275	0.303	0.329	0.354	0.384	0.416
3.3	0.148	0.112	0.217	0.244	0.273	0.301	0.327	0.351	0.380	0.410
3.4	0.154	0.120	0.216	0.243	0.273	0.300	0.327	0.351	0.383	0.415
3.5	0.159	0.116	0.216	0.243	0.272	0.299	0.325	0.348	0.379	0.408
3.6	0.166	0.115	0.217	0.242	0.271	0.297	0.323	0.346	0.375	0.403
3.7	0.271	0.130	0.216	0.242	0.270	0.296	0.322	0.345	0.377	0.408
3.8	0.280	0.120	0.216	0.241	0.268	0.294	0.320	0.342	0.373	0.401
3.9	0.279	0.118	0.216	0.240	0.267	0.292	0.318	0.339	0.369	0.394
4.0	0.281	0.116	0.216	0.240	0.266	0.291	0.316	0.336	0.365	0.387
4.1	0.265	0.133	0.219	0.243	0.269	0.294	0.319	0.340	0.371	0.399
4.2	0.255	0.126	0.217	0.239	0.264	0.288	0.314	0.334	0.367	0.395
4.3	0.247	0.125	0.217	0.238	0.264	0.286	0.312	0.332	0.364	0.389
4.4	0.243	0.123	0.218	0.238	0.263	0.285	0.310	0.329	0.360	0.382
4.5	0.235	0.119	0.219	0.239	0.262	0.283	0.308	0.326	0.356	0.375
4.6	0.220	0.137	0.220	0.238	0.262	0.283	0.307	0.327	0.362	0.389
4.7	0.216	0.122	0.221	0.237	0.261	0.281	0.306	0.325	0.358	0.383
4.8	0.214	0.122	0.223	0.239	0.260	0.280	0.304	0.323	0.356	0.376
4.9	0.206	0.122	0.224	0.238	0.260	0.278	0.302	0.320	0.354	0.370
5.0	0.201	0.113	0.225	0.237	0.260	0.277	0.300	0.318	0.352	0.362

Table D.16: Resolution results with SPWD processing: vertical resolution in degrees for angles $15° - 24°$, horizontal angle $= 15°$.

Vertical Angle (deg) Range (m)	15	16	17	18	19	20	21	22	23	24
3.0	0.438	0.421	0.509	1.084	1.135	0.784	0.788	0.843	0.896	0.977
3.1	0.449	0.444	0.469	0.823	1.210	0.778	0.794	0.850	0.904	0.985
3.2	0.442	0.446	0.502	0.543	1.210	0.780	0.794	0.851	0.905	0.985
3.3	0.434	0.448	0.785	0.621	1.197	0.779	0.795	0.852	0.905	0.985
3.4	0.454	0.459	0.735	0.976	0.783	0.799	0.808	0.863	0.915	0.994
3.5	0.446	0.459	0.446	0.957	0.783	0.800	0.809	0.865	0.916	0.995
3.6	0.435	0.481	0.688	0.979	0.805	0.811	0.814	0.868	0.916	0.996
3.7	0.461	0.492	0.751	0.774	0.858	0.828	0.825	0.877	0.926	1.004
3.8	0.445	0.486	0.732	0.990	0.861	0.831	0.826	0.879	0.926	1.005
3.9	0.433	0.482	0.642	0.989	0.856	0.830	0.827	0.880	0.927	1.005
4.0	0.423	0.761	0.475	0.969	0.851	0.827	0.827	0.879	0.927	1.006
4.1	0.451	0.508	0.746	0.965	0.931	0.865	0.847	0.894	0.934	1.008
4.2	0.467	0.579	0.782	0.933	0.944	0.870	0.854	0.900	0.940	1.019
4.3	0.454	0.587	0.760	0.947	0.947	0.871	0.855	0.900	0.940	1.020
4.4	0.431	0.597	0.754	0.982	0.950	0.872	0.857	0.901	0.940	1.021
4.5	0.418	0.606	0.995	0.999	0.951	0.875	0.858	0.902	0.941	1.021
4.6	0.474	0.601	0.700	1.095	1.001	0.896	0.877	0.915	0.951	1.031
4.7	0.465	0.605	0.980	1.139	1.009	0.899	0.879	0.915	0.951	1.031
4.8	0.452	0.610	1.007	1.145	1.015	0.903	0.880	0.916	0.952	1.032
4.9	0.431	0.617	1.037	1.155	1.018	0.903	0.882	0.917	0.952	1.032
5.0	0.411	0.620	1.060	1.172	1.023	0.904	0.883	0.917	0.952	1.033

VITA

Catherine Ann Hillsley Frazier received the B.S.E.E degree *summa cum laude* from the University of Maryland at College Park in 1994, where she held the Thomas J. Watson scholarship and a Maryland Distinguished Scholar Award. She entered the Graduate College at the University of Illinois at Urbana-Champaign in the Department of Electrical and Computer Engineering, and received the M.S. in 1996. She held a position as research assistant in the Bioacoustics Research Laboratory from August 1995 to May 2000. From August 1994 to July 1997, she held a National Science Foundation Fellowship. From August 1994 to July 1995, she also held the Koehler Fellowship. In April 1997, she was awarded the Robert T. Chien Memorial Award for outstanding research in electrical engineering. From January 1998 to December 1999, she was the student representative to the Administrative Committee of the IEEE Ultrasonics Ferroelectrics and Frequency Control Society. She has accepted a position on the technical staff at the Johns Hopkins University Applied Physics Laboratory in the Submarine Technology Group. Her current research interests are in acoustic image formation and array signal processing. She is a member of IEEE and the Acoustical Society of America as well as Eta Kappa Nu and Tau Beta Pi.